NATIONAL UNIVERSITY OF IRELAND GALWAY

Woofer-Tweeter Adaptive Optics for Astronomy

by

Thomas Farrell

Supervised by Professor Chris Dainty

A thesis submitted in partial fulfilment for the
degree of Doctor of Philosophy

in the
Applied Optics Group
School of Physics

March 2010

Contents

NATIONAL UNIVERSITY OF IRELAND GALWAY

Abstract

Applied Optics Group
School of Physics

Doctor of Philosophy

by Thomas Farrell
Supervised by Professor Chris Dainty

Adaptive optics has been used in telescopes to enable them achieve diffraction limited performance through atmospheric turbulence. As a technology, it is constantly improving to allow operation on larger telescopes with improved resolution and field of view. A dual mirror, single conjugate technique known as woofer-tweeter adaptive optics is one such technique which will be implemented on extremely large telescopes. Dual mirrors allow optimised correction of atmospheric aberrations with the woofer correcting for low spatial frequency aberrations and the tweeter correcting for high spatial frequency aberrations. The investigation of the methods and theory behind this technique through simulation and experiment form the basis of this thesis. A comparative analysis of eight commercially available deformable mirrors is shown with the two most appropriate mirrors (37 actuator Oko Technologies woofer and a 140 actuator Boston Micromachines tweeter) chosen for the woofer-tweeter laboratory demonstrator. Using such methods in a scaled 8 metre class telescope system, gains in Strehl ratio of approximately 30% are found over use of a single deformable mirror whilst the load on deformable mirrors is much reduced.

Acknowledgements

I wish to foremost acknowledge my supervisor Professor Chris Dainty for his guidance and understanding throughout my time as a student. I am also grateful to Sasha Goncharov, Nicholas Devaney, Ruth Mackey and Eugenie Dalimier for all their helpful advice and contributions.

This research was supported by the Irish Research Council for Science Engineering and technology under their postgraduate scholar scheme and through Science Foundation Ireland, grant SFI/01/PI.2/B039C.

Abbreviations

ADU	**A**nalogue to **D**igital **U**nit
AO	**A**daptive **O**ptics
DM	**D**eformable **M**irror
ExAO	**Ex**treme **A**daptive **O**ptics
ELT	**E**xtremely **L**arge **T**elescope
FoV	**F**ield **o**f **V**iew
GS	**G**uide **S**tar
LGS	**L**aser **G**uide **S**tar
MCAO	**M**ulti **C**onjugate **A**daptive **O**ptics
MEMS	**M**icro-**E**lectro-**M**echanical **S**ystem
PSF	**P**oint **S**pread **F**unction
RMS	**R**oot **M**ean **S**quare
SCIDAR	**SCI**intillation **D**etection **A**nd **R**anging
SR	**S**trehl **R**atio
SVD	**S**ingular **V**alue **D**ecomposition
TT	**T**ip **T**ilt
WFS	**W**ave**F**ront **S**ensor
WTAO	**W**oofer **T**weeter **A**daptive **O**ptics
VLT	**V**ery **L**arge **T**elescope

Chapter 1

Introduction

The Earth's atmosphere has long been identified as a limiting factor in astronomical observations. The 'tremors of the atmosphere' that Newton mentions have the effect of reducing imaging resolution in telescopes far short of diffraction limited performance. When imaging through strong turbulence the resolving power of a telescope is not proportional to its diameter but to the characteristic coherence length of turbulence called the Fried's parameter (Sec. 2.4). which may only be 5-15cm at visible wavelengths. This became a real problem in the 20th Century when telescopes continued to increase in size. Babcock[1] was the first to suggest a means to actively combat these atmospheric distortions by what became known as 'Adaptive Optics' (AO). The basic technology includes a wavefront sensing component, a wavefront shaping device and the hardware to compute all the control calculations at the required bandwidth. The implementation of AO on many telescopes around the world has been of great benefit to the astronomical community. Ground based telescopes can now match and improve on the performance and stability of the Hubble Space Telescope (figure 1.1).

As the technology has matured improvements have been sought; wider field correction, extreme high contrast correction and ultimately implementation on the next generation of telescopes. It is this latter challenge which will prove most difficult requiring massive investment in research to overcome the many technical challenges. Key to the success of these future giant telescopes will be some form of Woofer Tweeter Adaptive Optics (WTAO), a means by which to split AO correction over two spatial shaping

devices. The theory and experimental evaluation of this technology is the subject of this PhD thesis.

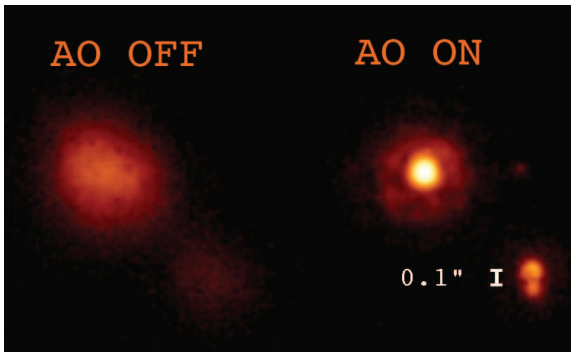

FIGURE 1.1: An image from the AO equipped MMT showing the benefits of AO correction on a small star cluster. The image on the left is without AO, with what seems to be a faint binary star. With correction it is possible to make out the bright guide star with a faint binary star in the bottom right. *CREDIT:Laird Close, CAAO, Steward Observatory*

In Chapter 2, I give a historical context to the rise of adaptive optics for astronomy, describing the statistical properties of atmospheric turbulence and its application to astronomical images. An overview is then given to the main features of AO systems with particular emphasis on wavefront sensors. The current trends in AO research are then explored including wider field AO, Laser Guide Star (LGS) and Extreme Adaptive Optics (ExAO).

Chapter 3 begins with a description of various deformable mirror types with a more detailed overview of the two chosen for the WTAO laboratory experiment, a low order piezoelectric DM and a high order MEMS device. An assessment of various available DMs is made through Monte Carlo simulations of atmospheric wavefront fitting. The results of these simulations have been presented at a number of conferences and are the subject of a peer-reviewed paper[2]. The atmospheric comparison of deformable mirrors is my contribution to this work with other researchers responsible for a comparison of mirrors in fitting ocular wavefronts.

The theoretical framework for WTAO spatial control is given in Chapter 4, which includes a number of different theories taken from literature. Simulations are used to test these various control methods for the experimentally measured interaction matrices of a woofer and tweeter DM.

Chapter 5 contains all the design background for the WTAO bench demonstrator. Each major part of the design such as turbulent phase screens and CCDs is discussed. The closed loop operation is described for static turbulence with the contrasting results of the different control schemes given. A short chapter then describes the main conclusions from this research work.

Work on this PhD study began in August 2004 with the Applied Optics group in N.U.I. Galway. For the first year I studied the background of AO and MCAO through simulations with Yorick AO, in particular simulations on multi mirror MCAO in ELTs. It was not until September 2005 that I decided to begin my work on WTAO, when at the time it was apparent that such methods were necessary for future large telescopes. At that time there had been no experimental verification of the technique and no published work dedicated to the subject. In the following years and months a number of studies were published which verified many of the concepts of WTAO. In this thesis I have referenced these works and included some of their theories in my experiment.

The experimental results achieved in this thesis show that woofer tweeter adaptive optics techniques are viable for use in large telescopes with performance gains realised and reduced mirror loading evident.

Chapter 2

Adaptive Optics and Astronomy

2.1 Historical background

The rise of astronomy from basic naked eye observations of star patterns has been immensely useful in helping earlier generations to navigate and in timekeeping. The advance of astronomy has been aided mostly by advances in the telescopes and the instrumentation associated with them. Telescopes have since evolved from simple, small refractors to giant refractors and then to the more common 8-10 metre class reflectors of today. At each point the distorting effects of the atmosphere were apparent to astronomers. The advent of photography made the situation worse with long exposures becoming blurred due to atmospheric effects.

It had long been recognised that avoiding the worst of the Earth's turbulent atmosphere was the best solution with telescopes located in high altitude mountain sites. Even so the aberrations of the atmosphere still dominate. The idea of phase manipulation to correct these aberrations only became apparent through the use of the Foucault knife edge test. This test was originally conceived to measure the aberrations of the primary mirror. This test was then adopted to measure atmospheric aberrations beyond the telescope and these early tests gave astronomers the scale of correction needed to obtain full resolution. Babcock's seminal 1953 paper[1] gave the first design of an AO system, although one that was technically unfeasible at the time.

As is usually the case, military requirement is the mother of all invention and AO became a reality for two American military programs during the Cold War. Adaptive

optics was used to pre-correct for horizontal path aberrations and allow high power laser beams to focus on a distant target. One of the first AO systems to be employed in this task used a segmented deformable mirror and multi-dither algorithms to achieve phase correction. A far more challenging application of AO was in correcting atmospheric distortions to allow the imaging of foreign orbiting satellites. Hardy's real time atmospheric compensator was the first 2D AO system and was soon succeeded by the larger Compensated Imaging System in 1982[3]. This 168 actuator system was hugely advanced for its time although largely unknown for most of its life due to its classified nature. The first dedicated astronomical AO system was developed in Europe by the European Southern Observatory (ESO) with a system known as 'COME-ON'[4].

The dearth of bright guide stars in the sky severely limits the amount of science targets to view through AO. This was recognised quite early in the development of AO systems with laser beacons being proposed as a solution. The use of Laser Guide Stars (LGS) as a means to open sky availability was suggested by Foy and Labeyrie[5] in open literature although the idea had been previously been the subject of classified military research. Telescopes which employ laser guide stars include the Hawaian Keck Observatory[6], the Californian Lick Observatory[7] and both the Gemini telescopes.

Adaptive Optics is a reasonably mature technology having been ported from military and astronomical applications into more beneficial areas such as ophthalmology, optical coherence tomography and free-space optical communication. Astronomy remains the main driver of the technology with large budget telescope projects providing the focus for the next generation of AO use.

2.2 Adaptive Optics

The aim of adaptive optics in astronomy is to minimise the wavefront disturbances at the telescope pupil through sensing and real time spatial light modulation. These disturbances are caused primarily through atmospheric turbulence and secondarily by internal aberrations within the telescope and instrumentation. Future large telescope mirrors will be segmented and employ active optics to ensure internal aberrations are kept to a minimum. Atmospheric aberrations have the effect of reducing resolution of

astronomical images to a characteristic 'seeing disc' many times larger than the diffraction limit of the telescope. Increases in the size of telescope aperture bring no increases in resolving power unless fitted with an AO instrument. The principal components of

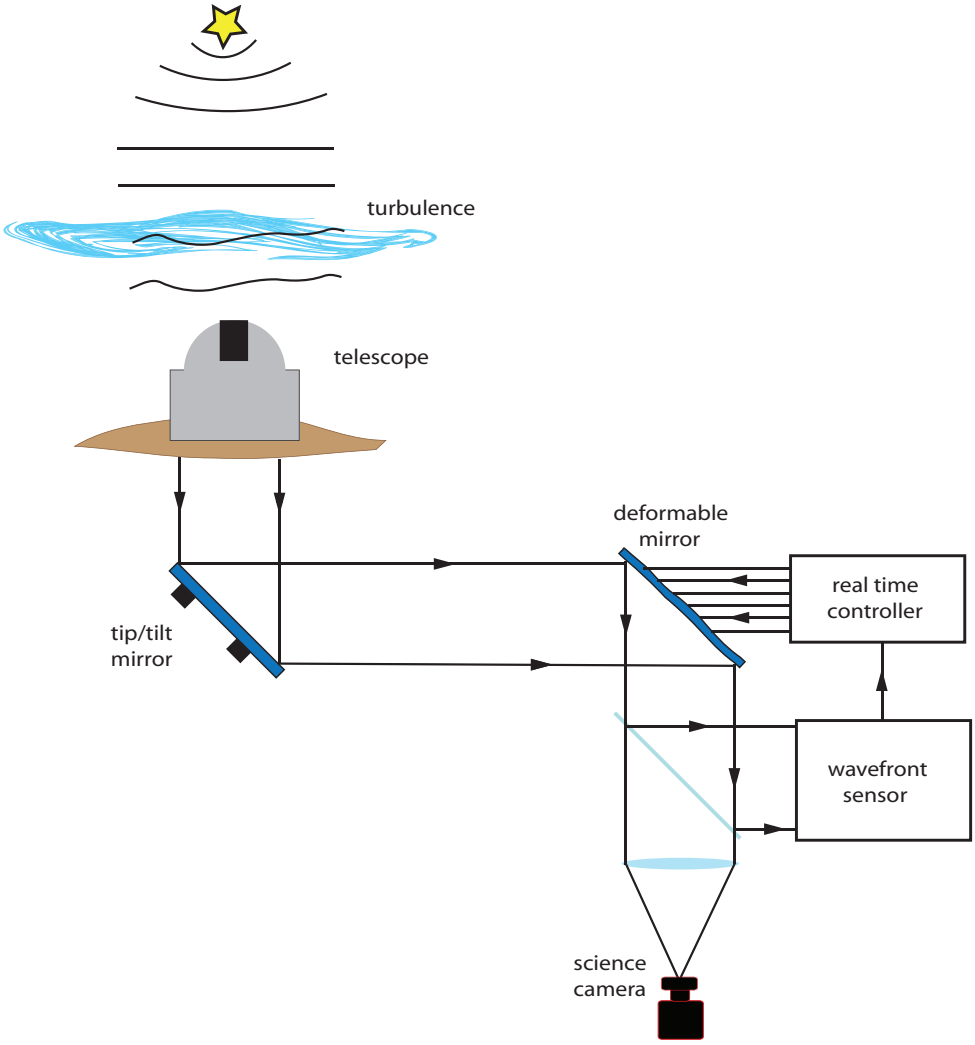

FIGURE 2.1: Schematic of a standard AO system with a single deformable mirror and tip/tilt mirror conjugated to the ground layer turbulence.

an adaptive optics system are

- **Reference beacon:** A sufficiently bright source of light located at infinity or at a large distance is needed to allow sensing of turbulence. This can be a Natural Guide Star (NGS) or a laser guide star. Using NGS limits sky availability as bright stars have to be located within the isoplanatic angle of the science target.

- **Wavefront sensor:** This is the device which computes the aberration at the pupil plane. There are numerous ways to achieve this with indirect aperture subdivision methods being most common.

- **Spatial correction device:** These devices control the shape of wavefront and are usually deformable mirrors used in reflection. Beam wander is controlled separately using a tip/tilt mirror.

- **Real time control computer:** Wavefront sensor measurements have to be converted into appropriate control signals for the correction device. A real time controller is needed to perform the matrix operations and temporal filters at sufficient bandwidth.

A schematic for a typical single star, ground conjugate AO system is shown in figure 2.1. The light from some NGS reaches the Earth's atmosphere as a planar wave before being corrupted by turbulence. A single tip/tilt mirror and a properly specified deformable mirror are situated before the WFS. Adaptive Optics is operated in closed loop with mirror corrections feeding into the WFS until correction reaches a stable point.

Supplementary to these major components are the other devices such as re-imaging optics, beam-splitters, filters, science camera, high voltage electronic drivers, atmospheric dispersion correctors etc. I will only detail these major components in this introduction with some detail of minor components being touched upon in the experimental chapter.

2.3 Wavefront Sensing

An optical wavefront is the surface of points that are within one wave of each other and have the same phase. Since it describes the phase relationship between points across some pupil, it also fully describes the associated aberrations. Accurate spatial sensing of these wavefronts at a sufficient bandwidth is essential to enable closed loop AO to function. A good WFS for astronomy will have the required spatial resolution to resolve high frequency phase details, be able to sense wavefronts from faint light sources and operate on incoherent white light and possibly extended sources. There are many different methods to perform wavefront sensing including:

- **Shack-Hartmann wavefront sensor[8]:** This senses local gradients through aperture sub-division with a lenslet array. This is the most common of wavefront sensor in astronomy and ophthalmology and is discussed in greater detail below.

- **Curvature sensor[9]:** This technique employs direct measurement of wavefront curvature as well as radial tilts to allow wavefront reconstruction by solving the Poisson equation. By locating two detectors at planes in front and behind the focus point of the wavefront and recording the irradiance patters, the difference between the signals can be shown to yield the wavefront curvature as well as radial tilts at the edge. Roddier[10] used a membrane mirror which has variable curvature to allow optical modulation of the focus point and imaging onto a single detector. This approach requires simpler optics, less calibration and can be tuned to varying strengths of turbulence. One very successful implementation of a curvature sensor was on the PUEO adaptive optics instrument where, paired with a low order bimorph mirror, it gave diffraction limited performance for median seeing[11].

- **Lateral shear interferometor[12]:** A shearing interferometer works on the basis of splitting a wavefront into two and recombining with one wavefront slightly displaced. The resulting interference patterns record the wavefront tilt and allow wavefront reconstruction from partially extended sources. To ensure achromatic operation a diffraction grating can be used to allow the variation of shear to be linear to wavelength. These WFSs are not commonly used in astronomical AO due to their complexity and difficulties in operation.

- **Pyramid wavefront sensor:[13][14]** A pyramid shaped prism is placed at the image plane of the light beam under inspection. Four separate pupils are then imaged in four quadrants with the resulting intensities indicating the direction of phase derivative. This is, in effect, a Foucault knife-edge test. Some modulation of the prism or focussed image is necessary to determine the amplitude of phase differences and to allow full wavefront reconstruction. This modulation can be achieved circularly or transversely with rotating beam steering mirrors or controllable prisms.

2.3.1 Shack-Hartmann wavefront sensor

The broadband, incoherent light associated with astronomy means direct interferometric measurements of atmospheric wavefronts are impossible. Incoherent shop testing methods also fail due to the high temporal frequency changes in atmospheric turbulence. The

gradients created by phase perturbations can be recorded in real time through irradiance measurements. By sub-division of the aperture it is possible to measure a grid of local gradients. The Shack-Hartmann wavefront sensor adopts this approach and is the product of two scientists, Johannes Hartmann and Roland Shack. Hartmann working at the turn of the 19th Century developed his Hartmann screen test to measure aberrations in telescope optics. His method required a mask with a grid of holes placed over the area under inspection and observation of an out-of-focus image near the image plane. Shack's contribution was eliminating the light losses caused by having a mask and using a lenslet array to capture all the light possible into a grid of focal spots. Figure 2.2 shows a schematic of a typical Shack-Hartmann WFS. Lenslet arrays can have circular or hexagonal geometries which should be matched to the deformable mirror geometry. A low noise photon sensor is required at the focal plane to allow AO to be implemented on low light level sources.

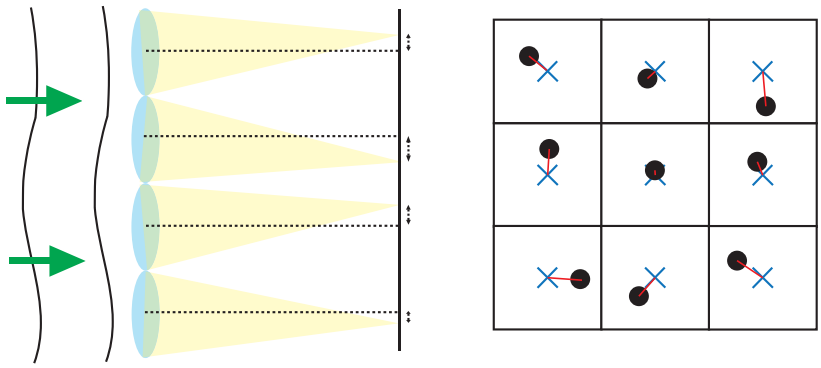

FIGURE 2.2: Subdividing an incoming wavefront with a lenslet array creates an irregular spot pattern. Imaging the resulting spot pattern and converting the pixel irradiance values into gradients allows full wavefront reconstruction to be computed.

When a flat wavefront is passed through the lenslet array, a spot pattern will be imaged onto camera, with spot positions matching the pitch and geometry of the lenslet array. If a turbulence distorted wavefront is measured these spots are displaced from there central positions. Each spot is sampled over a grid of pixels which can vary in size from 2^2 to n^2 pixels with the number of pixels n being limited by the pixel resolution of a detector. Increasing the number of pixels introduces more read noise per subaperture with minimal increases in sensitivity, hence quad cells are commonly used. Larger arrays of pixels give increased dynamic range and linearity across the aperture. In closed loop operation, small deviations around the null point are the norm for which quad cells

have acceptable accuracy. The offset positions of these gradients can be calculated in a number of ways.

Standard centroiding or center of gravity algorithms are commonly used to determine spot positions[15]. For an array of pixels with coordinates i, j the corresponding slopes s_x and s_y are

$$s_x = \frac{\sum_{i,j} x_{i,j} I_{i,j}}{\sum_{i,j} I_{i,j}} \text{ and } s_y = \frac{\sum_{i,j} y_{i,j} I_{i,j}}{\sum_{i,j} I_{i,j}} \tag{2.1}$$

with the recorded irradiance pattern $I_{i,j}$ for each pixel $x_{i,j}$ and $y_{i,j}$.

Another method of calculating these local wavefront gradients from a SH sensor is to use Maximum Likelihood estimation[16]. A wavefront sensor can be viewed as a linear system where an incoming wavefront, described in some parameter space by θ, is transformed into detector output signal g which is subject to some measurement noise n. The equation for this is

$$g = H\theta + n \tag{2.2}$$

with H being some operator that transforms wavefronts into raw detector signals. In the case of a SH wavefront sensor the raw detector signal g is provided and an estimate of θ is required. This estimate is found by maximising the likelihood of θ occurring for a given signal g. In equation terms,

$$\hat{\theta} = \text{argmax}(\text{pr}(g|\theta)) \tag{2.3}$$

A lookup table of probability density functions for parameter θ given signal g is required to allow the fast computation and estimation of wavefront data. This method of estimating wavefronts or derived wavefront terms such as centroids is the most efficient and allows low photon count wavefront sensing to be performed over the standard centre of gravity calculations due to the lower variance in slope estimates.

2.4 Atmospheric Turbulence

The limiting effects of the Earth's atmosphere on astronomical observations are caused by refractive index inhomogeneities in the air above the telescope. These minor variations in refractive index are due to the variations in air temperature, pressure and humidity. The strength and nature of this turbulence varies considerably at different

altitudes, different times and at specific locations. Typically the largest component of turbulence is concentrated at the lowest altitudes below a few hundred metres with nightfall bringing higher altitude layers caused by wind shear. The astronomical community has long since discovered the benefits of locating telescopes at higher altitudes to reduce the effects of ground layer turbulence.

2.4.1 Kolmogorov theory of atmospheric turbulence

In 1941 Komolgorov[17] proposed a theory for turbulent flow in a fluid medium which remains largely valid to this day. When energy is added (by the heating effects of the Sun) to a fluid medium such as air, there is a progression from large scale disturbances to smaller scale eddies. The initial large scale disturbance is known as the outer scale, L_0, and varies in size from 5-100m. Turbulent flow in the atmosphere occurs when the ratio of inertial forces to viscous forces exceeds a certain critical value. This ratio is known as Reynolds number and is given by,

$$Re = \frac{Lv}{k_v} \tag{2.4}$$

where L is the length scale, v is the characteristic velocity and k_v the kinematic velocity of the fluid. For the typical parameters; $L = 15\text{m}$, $v = 1\text{ms}^{-1}$ and $k_v = 1.5 \times 10^{-6}\text{m}^2 s^{-1}$ the dimensionless Reynolds number is 1×10^{-6}. As turbulence develops, energy is transferred from larger to smaller scale structures. The finest perturbation size is known as the inner scale, l_0. When Re falls below a critical value energy is dissipated by viscous friction. To reach stability the input rate of energy through heat must equal the rate of energy dissipation. In Kolmogorov's theory and within the inertial range $l_0 \leq L \leq L_0$, velocity fluctuations V are solely the product of scale size L and the rate of energy transfer ϵ. Given that the units of ϵ are m^2/s^3 then the only possible combination of the two variables is $V = (\epsilon L)^{1/3}$.

Kolmogorov used structure functions to describe the non-stationary random functions associated with turbulence and its related parameters of temperature, humidity and velocity. Typically a correlation function would be used to describe the statistics between distances in a material. However, for pure Kolmogorov turbulence with an infinite outer scale, the correlation function tends towards infinity as the separation between two points goes to zero. For this reason, structure functions are used. A structure function

for an observable $f(r)$ is defined as

$$D_f(r.r_1) = \langle [f(r) - f(r + r_1)]^2 \rangle \tag{2.5}$$

with $\langle\rangle$ denoting the ensemble average. Structure functions are necessary to describe the quasi-stationary and inhomogeneous variables of atmospheric turbulence in a locally stationary, homogenous and isotropic manner. These atmospheric variables incur changes in mean over time which makes it difficult to distinguish slow fluctuations. A temperature structure function is defined as

$$D_T(x.r) = \langle [T(x) - T(x + r)]^2 \rangle \tag{2.6}$$

with r the separation along a co-ordinate x. Temperature fluctuations in air affects imaging performance indirectly through refractive index changes. Refractive index n in air is directly related to air temperature and pressure. The refractivity of air is given as

$$N = 77.6P/T \tag{2.7}$$

with pressure P in millibars. Pressure fluctuations can be ignored as they are negligible compared to temperature fluctuations. Refractive index fluctuations for a vertical profile are then

$$\delta n = -77.6(P/T)\delta T \tag{2.8}$$

The associated structure function is then

$$D_N(r) = C_N^2 r^{2/3} \tag{2.9}$$

with C_N^2 being the refractive index structure constant which gives a measure of turbulence strength and has units of $m^{-2/3}$. The power spectrum of refractive index variations in atmospheric turbulence is useful to obtain a measure of frequency content for turbulence over the range between the inner and outer scale. As the kinetic energy within turbulence is proportional to V^2 and the spatial wavenumber is defined as $\kappa = 2\pi/l$, the one dimensional power spectrum is

$$\Phi_T(\kappa) \propto \kappa^{-2/3}, \tag{2.10}$$

whilst in the three dimensional case,

$$\Phi_T(\kappa) \propto \kappa^{-11/3} \tag{2.11}$$

Tatarski[18] has derived the three dimensional power spectrum for atmospheric temperature as

$$\Phi_T(\kappa) = \frac{\Gamma(8/3)\sin(\pi/3)}{4\pi^3} C_T^2 \kappa^{11/3} = 0.033 C_T^2 \kappa^{11/3} \tag{2.12}$$

As the refractive index structure constant is related to the temperature structure constant by

$$C_N = \frac{\delta N}{\delta T} C_T \tag{2.13}$$

the refractive index power spectrum (units=$m^{-5/3}$). is similarly found to be

$$\Phi_N(\kappa) = 0.033 C_N^2 \kappa^{-11/3} \tag{2.14}$$

This power spectrum is only valid within the inertial range between the inner and outer scale as it tends to infinity at larger spatial separations. Von Karman gave a modified version of (2.14) to allow the spectrum to converge to a constant at small spatial frequencies of $\kappa_0 \leq 2\pi/L_0$;

$$\Phi_N(\kappa) = 0.033 C_N^2 (\kappa^2 + \kappa_0^2)^{11/6} \tag{2.15}$$

The outer scale is an important parameter in turbulence statistics and its range of values are much debated in astronomical circles. The standard spectrum of Kolmogorov turbulence is usually written with infinite outer scale and the effect of finite outer scales is to reduce the lower spatial frequency contributions[19]. This effect is more pronounced as the telescope diameter exceeds the size of the outer scale. Given that the outer scale is usually measured as some length between $100m$ and even $10m$[20], many of the future extremely large telescopes will have larger diameters than the outer scale. The stroke and tip/tilt requirements for these telescopes will be greatly reduced[21] and it is important to have a measure of outer scale to properly specify and AO system for a telescope. For the rest of this thesis I will assume in all calculations and simulations an infinite outer scale as this will serve as an upper limit on what is expected for real turbulence.

The strength of these refractive index fluctuations which govern turbulence power are

directly proportional to C_N^2. The profile of C_N^2 changes relative to atmospheric height from ground. Knowledge of this profile is very important in designing an adaptive optics system for each new observation site and is usually the subject of much measurement and modeling. There are three distinct aberrating layers of the Earth's atmosphere[3];

- **Surface layer:** This extends from just above the telescope enclosure to a kilometre in the sky and contains the strongest component of turbulence. Turbulent flow is created by convection currents from diurnal cycles of warming and cooling ground and can be largely alleviated by siting a telescope high in the mountains at a specific location.
- **Planetary boundary layer:** This layer extends 10km and consists of a small amount of background seeing with a few thin layers (100-200m) of stronger turbulence.
- **Tropopause:** At some point above 10km there tends to be an area of strong wind shear.

The height dependant C_N^2 profiles can be measured in a few different ways.

- **Meteorological balloons:**[22] By ascending balloons fitted with temperature sensors the C_T^2 profile which can be converted to C_N^2 with great accuracy. This method is only useful for average site characterisation and lacks any instantaneous information due to the slowly ascending balloons. This can be overcome with large numbers of balloons launched at fixed time intervals.
- **SCintillation Detection And Ranging (SCIDAR)[23]:** This real time technique uses the scintillation patterns of binary stars to profile the turbulence strength and wind shear at some site. A recent study within our group showed the possibility of using SCIDAR techniques on a single star[24], The resolution is less than that achievable with meteorological balloons being limited to a few hundred metres.
- **SLOpe Detection And Ranging (SLODAR:)**[25] This is another instantaneous technique used for site profiling and real time optimisation or tuning of adaptive optics. An atmospheric profile is calculated through cross correlation of

SH slope data for binary stars. The benefits of SLODAR is the relative low cost and greater sky availability in comparison to SCIDAR with good lower altitude sampling. Overall turbulence profile resolution is good ($> 100m$) depending on the WFS resolution.

Turbulence models of C_N^2 profiles are useful for overall site characterisation and imaging calculations. The most successful numerical model has been the Hufnagel Valley method originally conceived for early AO in the defence community. Valley modified Hufnagel's earlier model to produce

$$\begin{aligned} C_N^2(h) = \quad & A \quad [2.2\text{x}10^{-53} h^{10} \left(\frac{w}{27}\right)^2 \exp\left(-\frac{h}{1000}\right) \\ & + \quad 1\text{x}10^{-16} \exp\left(-\frac{h}{1000}\right)] \\ & + \quad B \exp\left(-\frac{h}{100}\right) \end{aligned}$$

with the coefficient A representing an average fine structure constant, w is the high altitude factor and B is Valley's ground level factor. This equation can be extended to a more general form to account for more turbulent layers.

$$\begin{aligned} C_N^2(h) = \quad & A \quad \exp -\frac{h}{h_a} + B \exp\left(-\frac{h}{h_b}\right) \\ & + \quad 1\text{x}10^{-16} \exp\left(-\frac{h}{1000}\right)] \\ & + \quad B \exp\left(-\frac{h}{100}\right) \end{aligned}$$

In figure 2.3 I have plotted the C_N^2 profile for Hufnagel's model (solid) which describes a typical site which has dominant lower altitude turbulence and includes a band of turbulence around 10Km.

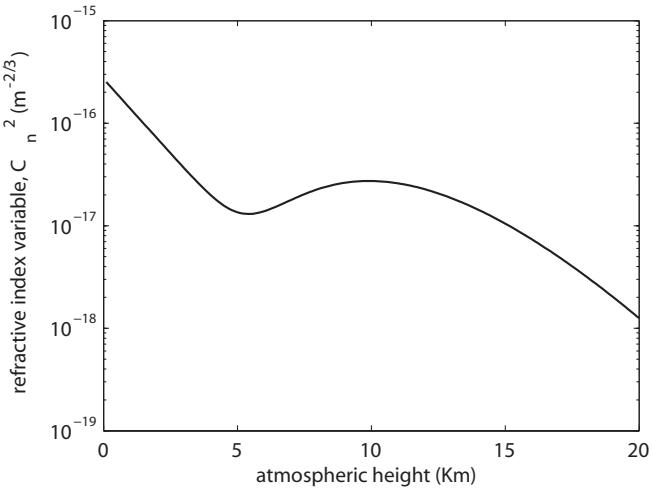

FIGURE 2.3: C_N^2 numerical profile using an adjusted Hufnagel-Valley model. Actual turbulence profiles would vary considerably from this model.

2.4.2 Imaging through turbulence

The phase distortions that arrive at the telescope entrance are the cumulative effect of refractive index variations through a vertical path in the atmosphere. For a continuous distribution of turbulence Roddier[26] gives the coherence function at the telescope aperture as

$$B_0(r) = \exp -1/2 \left[2.914k^2 \sec(\xi^{5/3}) \int dh C_N^2(h) \right] \tag{2.16}$$

with ξ being the observation zenith angle. Fried [27][28] defined the atmospheric transfer function $B(f)$and the phase structure function $D(r)$ as

$$B(f) = \exp -3.44(r/r_0)^{5/3} \tag{2.17}$$

$$D(r) = 6.88(r/r_0)^{5/3} \tag{2.18}$$

The r_0 parameter was defined by Fried as being the diameter of a diffraction limited telescope that matched the resolving power of the atmospheric transfer function. This 'Fried's parameter' as it is now known can be thought of as a coherence length of atmospheric turbulence; corresponding to the diameter of turbulence that has a phase variance of 1 rad^2. This equates to a Strehl ratio of 0.37 and not the 0.3 of Fried's original paper. The angular resolution of any telescope is therefore limited to the angular

resolution λ/r_0, a serious limitation for astronomers. Combining (2.16) and (2.17), the parameter r_0 can be expressed in terms of the integrated C_N^2 profile as

$$r_0 = \left[0.423k^2 \sec(\xi) \int dh C_N^2(h)\right] \tag{2.19}$$

The turbulence strength at a site can then be defined by one single parameter which is proportional to $\lambda^{6/5}$. Imaging with longer wavelengths increases the Fried's parameter and increases the resolving power of a telescope up to the diffraction limit.

The image measured from a telescope system is just the point spread function of the combined atmosphere and telescope pupil. Fraunhofer diffraction dictates that the PSF for a short exposure is

$$PSF \propto \|FT\{\Psi(r)P(r)\}\|^2 \tag{2.20}$$

with $\Psi(r)$the complex field at the telescope pupil and $P(r)$ is the telescope pupil function. The long exposure image is just the ensemble average of the short exposure for a given length of time.

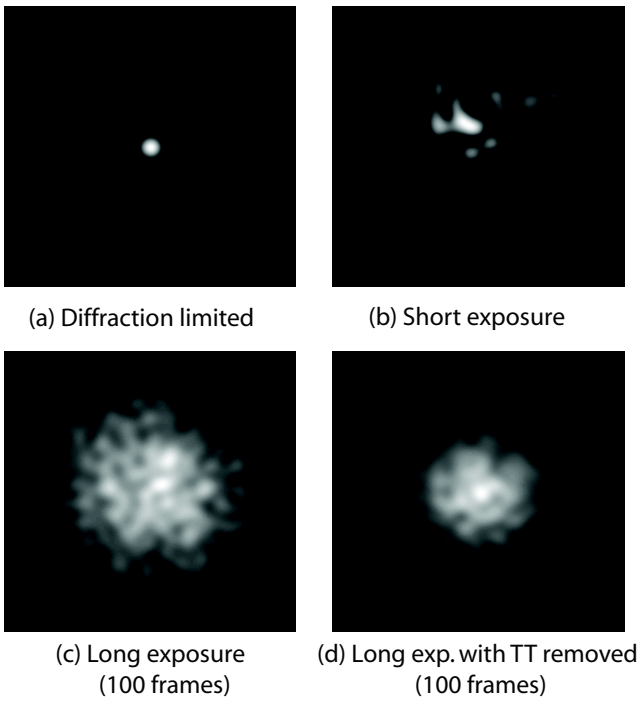

FIGURE 2.4: Results of simulated PSFs for an average of 100 turbulence samples showing the distorting effects of turbulence on image formation. The strength of turbulence used is $D/r_0 = 10$ with an infinite outer scale.

The effects of Kolmogorov turbulence on short and long exposure images is computed

and shown in figure 2.4. For a circular aperture with no central obstruction the PSF results in an Airy disc. By minimising the contribution of the atmosphere AO attempts to retrieve this image. These images are for an r_0 of $0.8m$ at $\lambda = 2.2\mu m$ on an $8m$ telescope giving a $D/r_0 = 10$. The long exposure images are just the sum of 100 frames so some residual fluctuations are present in figures 2.4(c) and (d).

2.5 Scientific Case for Astronomical Adaptive Optics

The driving force behind new telescope designs are the requirements of astronomers and cosmologists. Larger telescopes give these scientists more light and resolution to allow them observe fainter objects in greater detail. It is not the case of filling a technological vacuum for the sake of it; increasing a telescopes aperture from ten to thirty metres really does open up whole new areas of possible research. The ELTs of the next decade will be vital instruments to help with the following areas of research[29]:

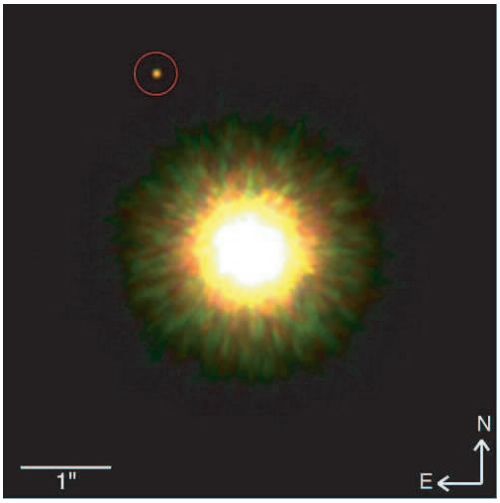

FIGURE 2.5: First image of an exo-planet around a Sun like star. Such planets will be the subject of much research thanks to the high resolution, light gathering properties of ELTs [30]

- **Extra-solar planet detection: (figure 2.5)** This is one of the most exciting areas of astronomy with ELTS equipped with advanced AO systems being able to directly image large planets from reflected light. Detection of smaller, Earth sized planets should also be possible using the radial velocity technique. Measurements on early planet formation will give greater insight into how our own planet evolved.

Completely mapping the planetary content of an extra-solar system will allow us to gauge our uniqueness in the universe.

- **Cosmology:** The proliferation of dark energy and dark matter in our Universe is one of the great mysteries in cosmology. ELTs will allow mapping of the gravitational effects of dark matter through observation of galaxy growth and evolution. By detecting the red shifts of distant galaxies and understanding the evolutionary dynamics, astronomers should have an insight into the nature of dark energy

- **The unknown future:** With the large period between defining science requirements and first light, there may be a lot of newer areas of astronomical research that could benefit from an ELT. History has shown us that the act of building a better telescope can lead to completely new and unforeseen phenomena.

2.6 Extremely Large Telescopes

Much like Moore's law, telescopes have followed their own law of growth since their inception many centuries ago. Typically over the last few centuries telescopes have doubled in size every 35-50 years (figure 2.6). Increasing the diameter of a telescope generally increases its resolving power and SNR, allowing imaging of fainter and smaller objects. Ignoring atmospheric distortions the angular resolution is proportional to λ/D, for a given wavelength λ and diameter D. The amount of light received is proportional to the square of diameter. The current generation of Very Large Telescopes (VLTs) have been operational for the last decade and have also followed this growth law. However the next generation of ELTs will have broken it considerably with apertures increasing 3-4 times what is currently available in a 20 year interval. This technological leap is laden with challenges, both in terms of technology and cost feasibility. The following are the main ELTs currently in planning to take astronomy through the 21st century.

- **Thirty Meter Telescope (TMT):** This is currently the most advanced of the ELT projects involving a number of partners from North America. The design is a 30m Ritchey-Chretien segmented telescope with a 3m secondary. No site has yet been decided and first light is planned for 2017.

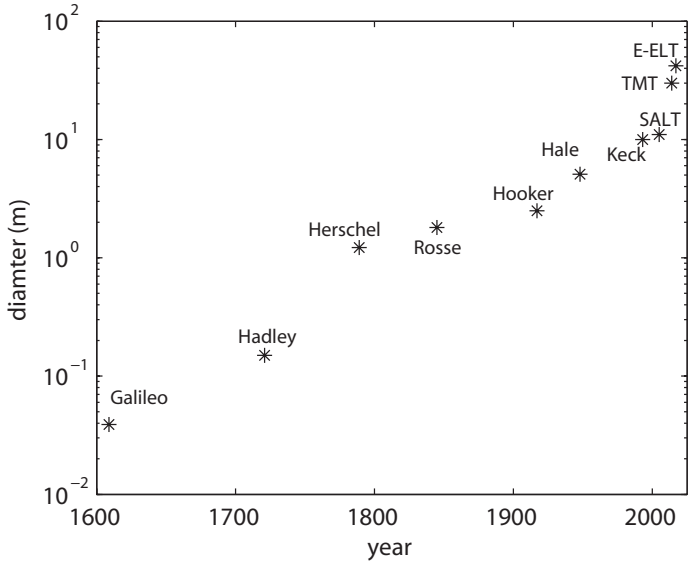

FIGURE 2.6: Some specific telescopes and their diameters throughout the years. The trend of the previous centuries will be broken by the next generation of ELTs

- **European-ELT (E-ELT):** This ESO project is the result of the shelved 100m OWL telescope and to a lesser extent the EURO50 telescope. The 42m segmented primary reflects onto a 6m secondary, itself a VLT class surface. Adaptive optics is implemented into the telescope design with a 2.7m woofer and 2.5m tweeter. First light is scheduled for 2016 but a lot of design briefs remain incomplete and behind the TMT.

- **Giant Magellan Telescope (GMT):**This 24m telescope is being developed by a consortium of mostly North American university groups. Its unusual design is based around 7 large 8.4m segments arranged radially around a central surface. Scheduled for completion in 2017.

- **Japan ELT (JELT):** This proposed Japanese project is a 30m design and is still in its early stages of development.

2.7 Wide Field Adaptive Optics

The standard single mirror, single conjugate AO has proved useful for astronomers in imaging solar planets and stars with greater detail. These observations are limited by the brightness and availability of NGSs close to the science target and their angular distance apart. To overcome these limitations artificial light beacons known as laser guide stars

are used in AO systems with multiple mirrors to give wider, more uniform correction across the sky. This section details the theory behind these angular limitations and their solutions.

2.7.1 Anisoplanatism

As the angle between some guide star and the science target increases, so too does the volume of turbulence relevant to the science target which is unsampled. At large separations θ, the higher altitude contribution to turbulence becomes completely unsampled leading to inferior AO correction (figure 2.7). This effect is known as anisoplanatism[31]. The effects of anisoplanatism for single conjugate adaptive optics from the PUEO AO system are seen in 2.8. The two images are part of a larger image and are separated by 30", with the outer image showing much poorer resolution. The non-uniformity of resolution is a serious hindrance to any photometry or astronomical calculations.

Tyson[32] gives the isoplanatic angle, that is the angle at which the mean square wavefront error between GS and object is 1 rad^2, as

$$\theta_0 = \left(2.91(2\pi/\lambda)^2 \int C_n^2(h) h^{5/3} dh\right)^{-3/5} \tag{2.21}$$

This can be simplified as $\theta_0 = r_0/\bar{h}$ with $\bar{h}$ being an average turbulence height given by

$$\bar{h} = \left(\frac{\int C_n^2(h) h^{5/3} dh}{\int C_n^2(h) dh}\right)^{3/5} \tag{2.22}$$

This mean turbulence altitude can also be defined by some dominant layer to allow a simpler calculation. If at some site the dominant layer is at 8km, with an average r_0 value of 12cm then the anisoplanatic angle is 0.81 arcseconds.

2.7.2 Sky coverage

Adaptive Optics requires a sufficiently bright guide star within the isoplanatic patch to successfully perform wavefront sensing. Stars which are too faint give too low a signal to noise ratio for wavefront sensing to operate. Only stars brighter than a certain limiting magnitude can be used. This limiting magnitude depends on the telescope, optical throughput and the efficiency of the detector. The availability of stars above this

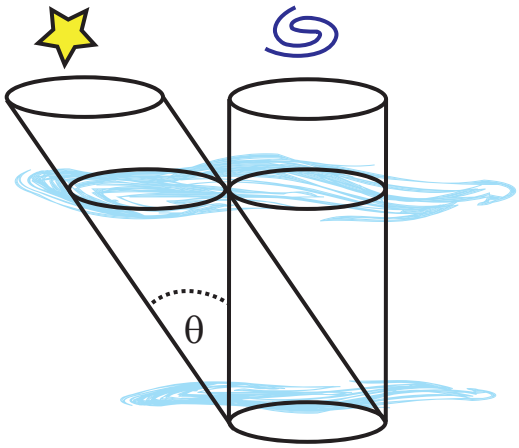

FIGURE 2.7: Schematic of anisoplanatic effects in the upper atmosphere, with beam profiles becoming separated at large angles of θ. This separation angle is purely a geometric parameter and not the isoplanatic angle θ_0.

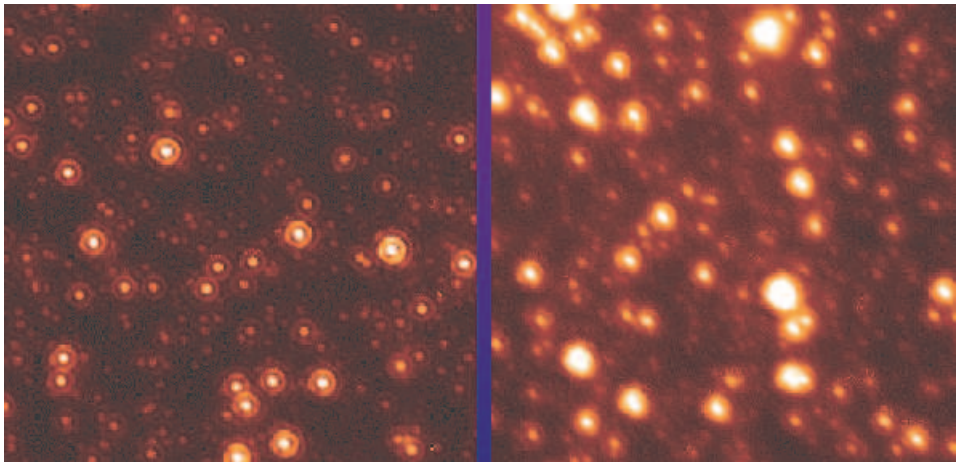

FIGURE 2.8: K band image from the AO system, PUEO at the Canada, France and Hawaii telescope. The images are separated in space by 30" demonstrating the detrimental effects of anisoplanatism.

limiting magnitude across the sky is known as sky coverage[33]. Flicker[34] describes sky coverage as,

$$\text{sky coverage} = \pi\theta_m \text{ x star density} \tag{2.23}$$

with θ_m being the instrument specific isoplanatic patch with star density only considering those of sufficiently bright magnitude. Simulations of sky coverage for the Gemini Observatory[35] indicate that coverage is generally below a few percent depending on observation conditions and target performance.

2.7.3 Laser Guide Stars

One obvious method to increase sky coverage is to create artificial light beacons located approximately at infinity in the sky. Foy and Labeyrie[5] suggested targeting lasers at the sky to create beacons of Rayleigh backscattered light at altitudes around 15km. Rayleigh backscattering becomes less prevalent at altitudes above 20Km which can be problematic when there are layers of turbulence above the beacons. Another method to create an LGS is to exploit the atomic resonance fluorescence of the sodium layer at altitudes of 80-100Km [36]. Either of these methods allows astronomers a degree of control in the location and brightness of guide stars, even combining the information from multiple beacons to allow tomographic reconstruction of the atmospheric volume.

There are some large drawbacks to LGS use which are still in active research. Focal anisoplanatism occurs due to the finite altitude at which the beacons occur and the resulting cone shape of the beam which leaves high altitude layers unsampled. This is particularly acute for Rayleigh backscattered LGS which are at a lower altitude. Sodium LGS suffer from a different problem, namely elongated beacons which create problems when wavefront sensing. This is due to the extended volume of the Sodium layer. Another problem is the issue of tilt indetermination which occurs due to the round trip the laser light takes from ground to upper atmosphere leaving the tilt modes undetermined. The simplest solution is to use a NGS for tilt calculation, which although not as stringent in star requirements still causes sky availability to drop. Getting an operational laser with the required power and tuning is also very difficult and has slowed their implementation on more telescopes.

2.7.4 Multi conjugate adaptive optics (MCAO)

Extending adaptive optics correction to wider fields requires atmospheric turbulence to be treated as a 3D volume. Single star wavefront sensing results in vertical path integrated wavefront from which altitude contributions are undetermined. By sampling the atmosphere with multiple stars and correcting with multiple mirrors it becomes a three dimensional technology. Beckers [37] provided groundwork for MCAO and atmospheric tomography in 1988 realising as well the necessary use of multiple LGS to combat the near zero sky coverage that a multiple star system would require. In truth MCAO does

not aim to treat the atmosphere as a true 3D volume but more as a combination of discrete 2D layers at specific volumes where turbulence is strongest. Indeed diffraction limited correction can be achieved over a wide field by conjugating only 2-3 deformable mirrors at specific altitudes[38].

It is possible to operate MCAO in two configurations, layer orientated and star orientated.

- **Star orientated MCAO:**[39][40] Each guide star senses its own patch of turbulence for a particular direction and is coupled to its own camera (figure 2.9). This is much like the case for single conjugate adaptive optics but the multiple stars allow tomography to be performed for a particular altitude layer. Each DM is then conjugated to an appropriate aliunde with the higher altitude corrections contributing to a wider corrected field of view.
- **Layer orientated MCAO:**[41] This approach contains a similar configuration of stars sampling the various sections of sky but each wavefront sensor now is conjugated to a particular altitude. Deformable mirrors are then paired to these conjugate altitude to allow separate control for each layer.

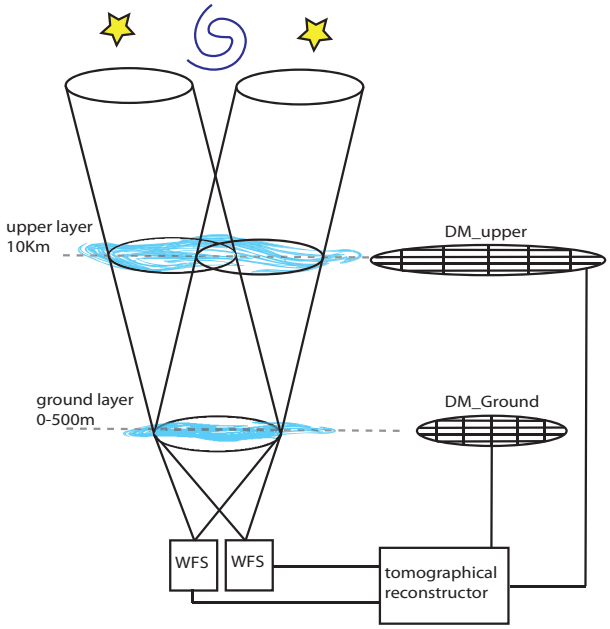

FIGURE 2.9: Schematic of star-oriented MCAO with a wavefront sensor for each guide star direction. Various geometries of guide star patterns allow for stitching of large areas of turbulence for wider correction.

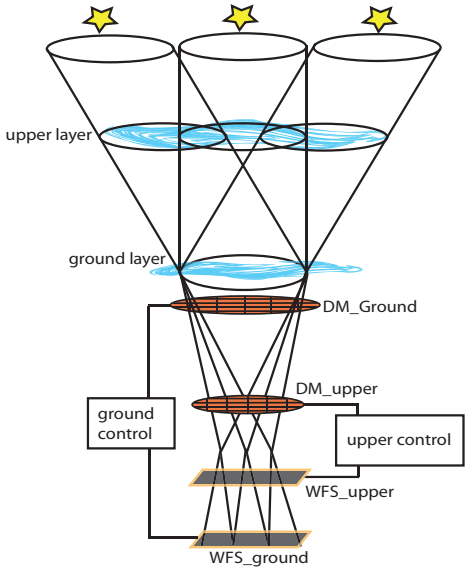

FIGURE 2.10: Schematic of layer-oriented MCAO where each wavefront sensor and deformable mirror are conjugated to a particular altitude. This approach usually requires a pyramid WFS for each conjugate altitude.

Another offshoot from MCAO is ground layer adaptive optics (GLAO)[42] which is a single conjugate, multi-star method. Atmospheric profiling has shown that the ground layer of the atmosphere is the dominant source of aberrations. The aim of ground layer adaptive optics is to really widen correction beyond MCAO but at much lower Strehl ratio. A typical GLAO system has a single deformable mirror conjugated to the ground layer with multiple guide stars illuminating from a wide field of view. The large separations in guide star pattern allows an averaging of high altitude turbulence and provides a uniform correction across the field [43] which amounts to a near doubling of encircled energy in the point spread function. Its intended effect is to provide good quality uniform seeing over the widest field possible, effectively halving the wavefront error[44]. The wide field gains in imaging performance of MCAO and GLAO are shown in figure 2.11.

2.8 High contrast extreme adaptive optics

Direct imaging of extra-solar planets has long been a holy grail of astronomy[45] that has since been achieved with the Keck and Gemini North telescopes (figure 2.5)[30]. The processing and techniques used to image this planet are quite complicated. Future detection of these planets require a device capable of high contrast, high Strehl

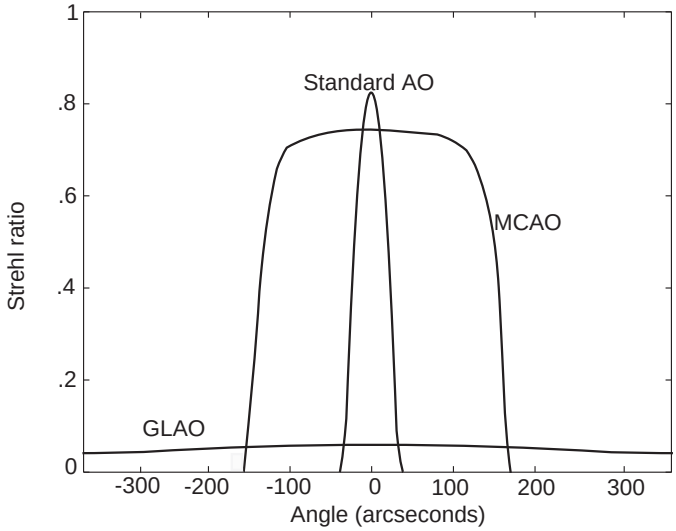

FIGURE 2.11: Strehl ratio as a function of off axis angles for standard AO, wider field MCAO and seeing improving GLAO.

ratio (Appendix 2) imaging. EXtreme Adaptive Optics (ExAO) is a technique to help astronomers image far more fainter and smaller extra solar planets with greater ease.

The basis of an ExAo system are a coronagraph to block as much light from the parent star as possible and a high resolution, low wavefront error adaptive optics system to get the high (>90%) Strehl ratio required. This extremely low wavefront error requires MEMS deformable mirrors with very flat surfaces. High spatial resolution correction is also a must and these systems will require dual mirrors to overcome the stroke limitations inherent with a high order MEMS mirror.

Chapter 3

Deformable Mirrors

3.1 Introduction

When Babcock[1] proposed his seeing compensation system, a crucial part of his design was the Eidophor mirror, an oil based phase forming device. The realisation of atmospheric phase correction only became possible with the introduction of mechanical Deformable Mirrors (DMs). It had been possible to shape static optical wavefronts through the use of lenses but for rapidly evolving atmospheric turbulence a dynamic correcting device is needed. The dynamic and spatial requirements for an atmospheric phase correcting device were beyond the technological capabilities for twenty years after Babcock's initial paper. The first Adaptive Optics (AO) systems were used to shape high power lasers propagated through atmosphere and the first two dimensional wavefront correction was achieved for satellite imaging[3]. The Real Time Atmospheric Compensator as it was known used continuous monolithic piezoelectric mirrors to perform wavefront correction[46].

As adaptive optics has matured, the range of wavefront shaping devices has increased. These include refractive devices and inertial devices. This study will only concentrate on the inertial types which include DMs. Whilst there are many types of mirror technology a lot of these have yet to be used operationally in telescopes but have found use in other AO applications. The main types of DM are:

- **Continuous facesheet[47]:** A continuous reflective facesheet is deformed by piezoelectric or electrorestrictive actuators. Large numbers of actuators are possible with stroke over $10\mu m$. They are relatively high in cost and some hysteresis is associated with this technology.

- **Segmented[48]:** Individual reflective segments are controlled my various actuator types. Total degrees of freedom depends on whether individual segments have piston only or piston with tilt control. Segmented mirrors with piston only control have a larger fitting error per number of actuators than continuous facesheet mirrors. The cost is relatively high and discontinuities in mirror surface lead to diffraction effects in image.

- **Bimorph[49]:**Sheets of bonded piezoelectric material with electrodes inserted control local curvature. These DMs have limited numbers of actuators but have excellent low order modal fitting. Large amounts of stroke may allow bimorph DMs to perform tip/tilt correction for atmospheric turbulence below a certain power which reduces system complexity although a tip/tilt mirror would be commonly used.

- **Membrane[50]:** A fixed reflective membrane is controlled by electrostatic actuators. These mirrors have limited stroke with number of actuators inversely proportional to peak deformation.

- **Microelectromechanical (MEMS)[51]:**These mirrors employ micro-lithography manufacturing processes to create integrated deformable mirror chips. Massive amounts ($100,000$) of actuators are possible with stroke values small but increasing all the time. This makes MEMS mirrors very low cost per actuator. The small mirror size make them inappropriate for certain applications where large angular magnifications would be required.

An ideal deformable mirror should have a low fitting error to dynamic turbulence. This is achieved through the following properties:

- have sufficient degrees of freedom
- operate at a sufficient temporal frequency
- have sufficient dynamic range (stroke) to compensate for the intended aberration

- have mirror modes which match those of the aberration
- be mechanically stable and robust
- have minimum residual wavefront error or flatness
- match the pupil diameter as close as possible
- cost as little as possible

In the following sections I will describe in more detail two of DMs used in the woofer-tweeter experiment and the technology behind their operation. A comparative study of for atmospheric wavefront fitting is then shown for eight commercially available DMs.

3.2 Continuous faceplate deformable mirrors with piezoelectric actuation

Mirrors which employ ferroelectric actuators bonded to a reflective faceplates are amongst the most common and cost effective DMs used in adaptive optics. These can include actuators based on the pizeoelectric[52] effect or on electrorestrictive[53] forces. Monolithic Piezoelectric Mirrors (MPM) which have one layer of ceramic material with inserted electrodes were amongst the first DMs used in adaptive optics. A more common approach now is to have discrete ceramic actuators bonded to a reflective facesheet (figure 3.1). One particular example of this type of DM is the 37 actuator mirror developed by OKO technologies (OKO37_PZT) and is the subject of this study (figure 3.2). The ceramic material used to create the piezoelectric forces required is a compound of lead, zirconate and titanate, Pb(Zr,Ti)O3, commonly known as PZT. The OKO mirror is a low cost example based on the transverse piezoelectric effect as opposed to the more common axial PZT type which use stacked ceramic elements. In the transverse case the deformation of a ceramic actuator with length l is given by [52]

$$\Delta l = V d_{31} l/h - \frac{\sigma l}{Y} \tag{3.1}$$

where V is the voltage applied, h is the thickness, σ is the stress applied and Y is Young's modulus. The variable d_{31} is the transverse piezoelectric coefficient and is typically around $0.3\mu m/kV$. The benefits of using transverse PZT actuators over stacked

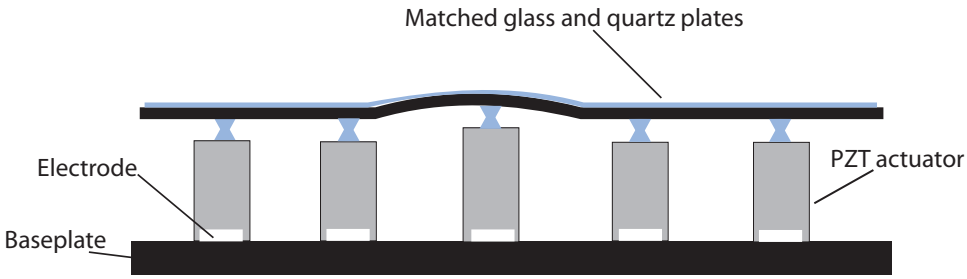

FIGURE 3.1: Schematic of the OKO37PZT.

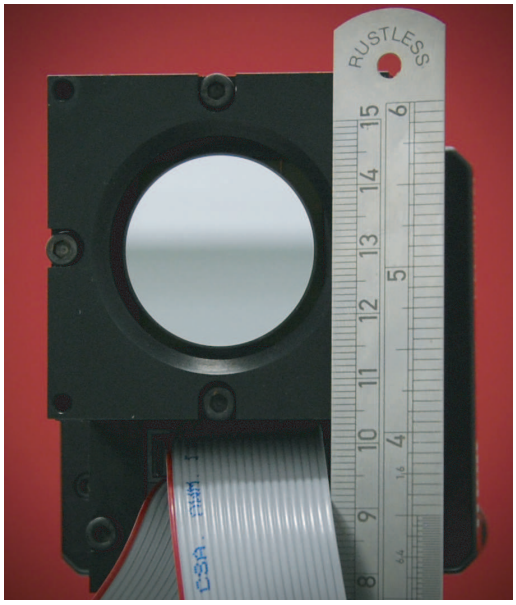

FIGURE 3.2: OKO37PZT with attached housing

ceramic actuators include

- Between 10-20 times lower power dissipation
- Much lower cost due to availability of low cost ceramic actuators
- Lower complexity in driver electronics which benefits costs and operating frequency

The main properties of the OKO37_PZT (figure3.1)are;

- Each actuator is manufactured onto an hexagonal grid with 4.3mm pitch (figure 3.3).
- The reflective faceplate consists of matched glass and quartz plates ($Al + MgF_2$)
- 30mm reflective aperture with free edge

- Initial RMS wavefront aberration of $.52\mu m$ in our particular mirror
- Highly linear operation
- $8\mu m$ maximum stroke
- 2KHz maximum operating frequency

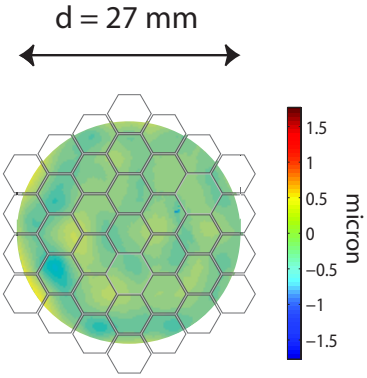

FIGURE 3.3: OKO37PZT actuator geometry and useable aperture with initial aberration overlayed.

The spatial fitting of any DM can be measured by recording its influence functions. A mirror's influence function is its phase response to individual actuator deformations or 'pokes'. The full range influence function of the OKO37PZT was recorded using a Twyman-Green Interferometer (Fisba Optik μPhase) with the resulting phase maps binned onto a 128×128 pixel grid (figure 3.4). Each actuator response map is the difference between positive and negative pokes about a bias position. Full positive and negative deformation is achieved at 210V and 0V with the bias position being the midpoint of 105V. The inner rings of actuators achieve individual, maximum deformations of approximately 4.5μm while the unfixed outer ring has a maximum deflection of 7μm.

Piezoelectric actuation is a linear effect as is evident with the OKO37PZT over its full range from 0-400 Volts (figure 3.5). Ramping voltage from its maximum to minimum ranges in a full loop will result in hysteresis effects. This was measured for the 19 actuator OKO as 14% of its full range[54]

To characterise wavefront fitting performance for a DM, an overview of the control theory is needed. The interaction matrix $\mathbf{D}$, relates the DM actuator commands c to measure phase ϕ.

$$\phi = Dc \tag{3.2}$$

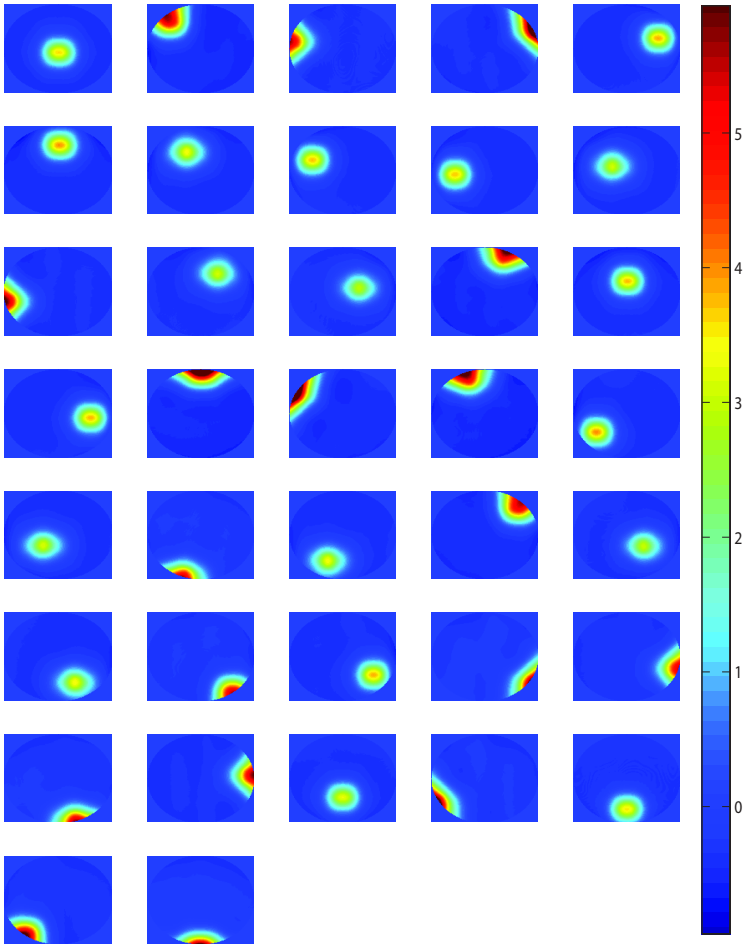

FIGURE 3.4: Influence function for OKO37PZT scaled in microns as recorded using an interferometer.

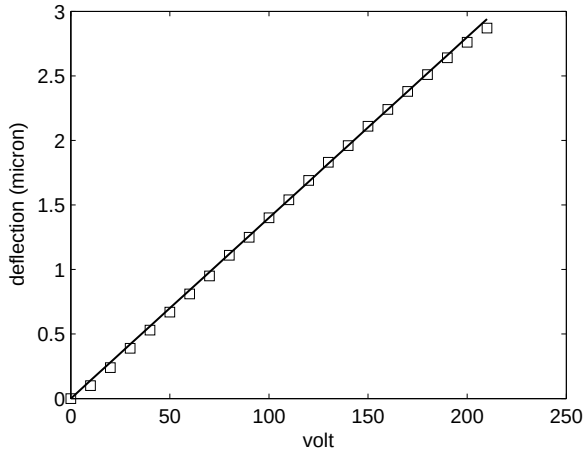

FIGURE 3.5: Phase response to control voltage for single OKO37PZT actuator.

The matrix $\mathbf{D}$, has a size of $n_{act} \times n_{pix}^2$ where n_{act} is the number of actuators and n_{pix} is the number of pixels used to record the phase maps. If a Shack-Hartmann lenslet array is used to record the wavefronts there would be $2n_{spot}$ number of spot measurements with each gradient measured in the x and y directions.

To find the control vector that gives a certain phase ϕ_m the inverse of D is required known as the control matrix M

$$c = M\phi_m \tag{3.3}$$

By using the least square approach (Appendix C) the control vector that minimises a wavefront ϕ_m is given by

$$c = (D^T D)^{-1} D^T \phi_m \tag{3.4}$$

The matrix $(D^T D)^{-1}$ is generally non-invertible due to $n_{pix} \gg n_{act}$. Singular Value Decomposition (SVD)[55] is used to find the generalised inverse of D and to obtain a set of orthogonal mirror modes.

$$D = UWV^T \tag{3.5}$$

- U contains the phase maps of the orthogonal mirror modes (figure 3.6) with each phase map stored as a vector. For a 37 actuator mirror (37 modes) with phase maps stored in $128^2 \times 1$ vectors, U has size 37×16384.
- W is a diagonal matrix containing the singular values. Small singular values lead to large mirror mode gains when inverted and this creates noise amplification. The singular values for the OKO37_PZT are plotted in figure 3.7.
- V contains the appropriate actuator command signals to recreate a particular orthogonal mirror mode.

The actuator commands are then obtained

$$c = VW^{\dagger}U^T\phi_m \tag{3.6}$$

The pseudo-inverse $W^{\dagger}$ is calculated by inverting every non-zero diagonal element λ_i in W.

One of the consequences of the OKO_PZT's design is its large degree of initial aberration. This is caused by lack of stiffness in the thin reflective plates as well stress in

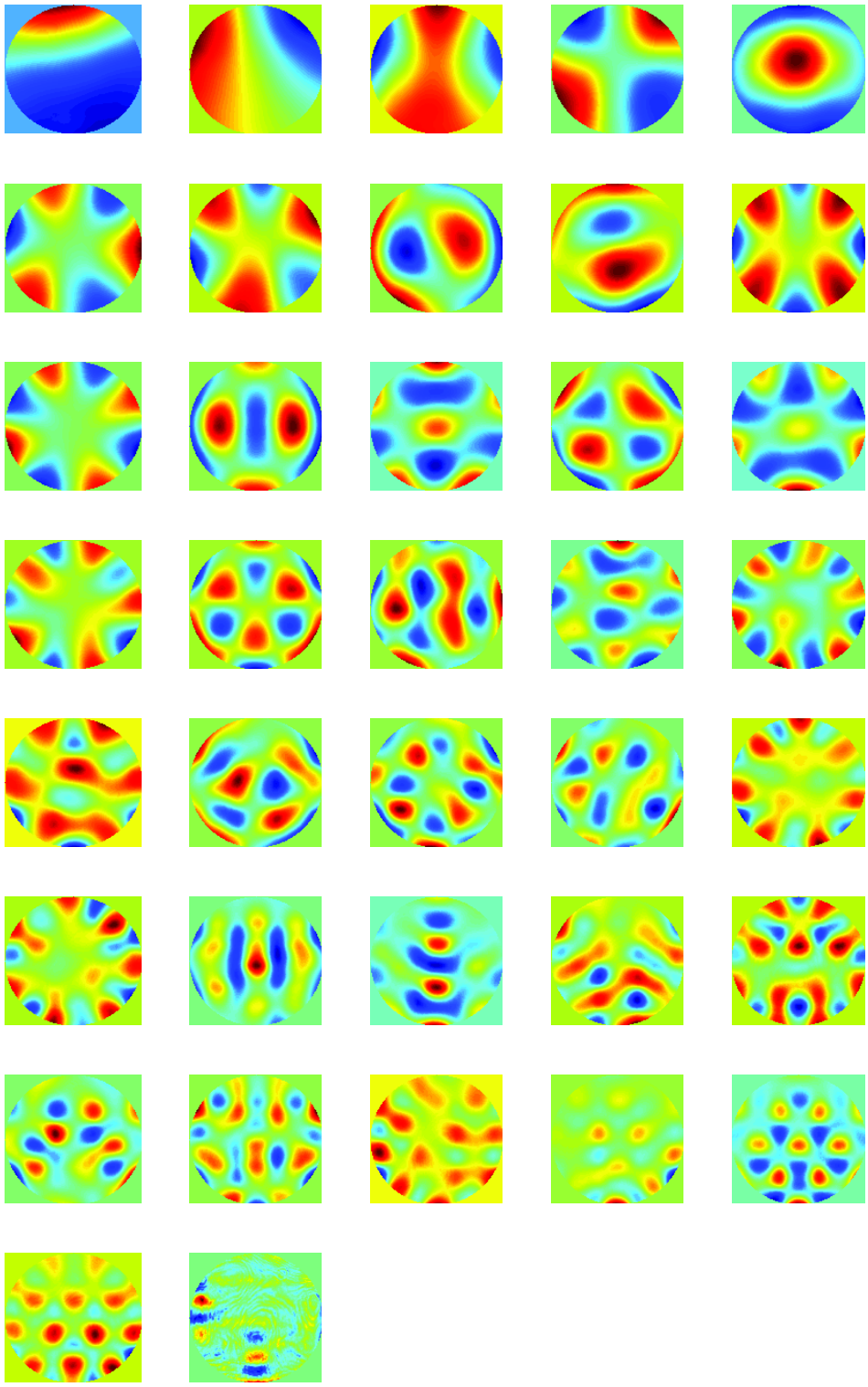

FIGURE 3.6: Orthogonal mirror modes obtained by SVD for OKO37PZT

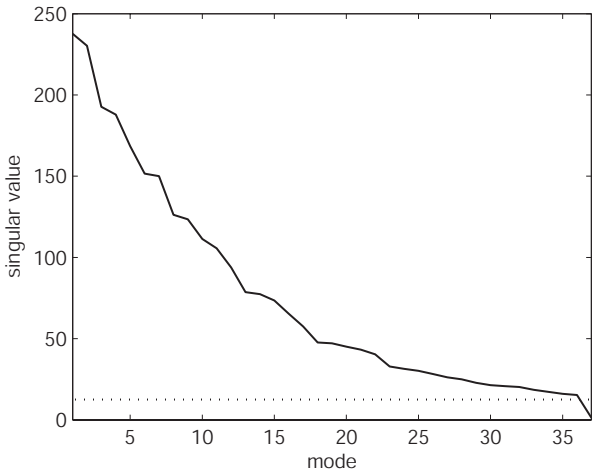

FIGURE 3.7: Singular values W for the OKO37PZT

the optical coating. The manufacturer lists this as less than $1.3\mu m$ RMS error from a reference sphere. At its bias position I measured $0.52\mu m$ RMS aberration. The command voltages to flatten the mirror were calculated from equation 3.6. A comparison between the simulated flattening and the measured result can be seen in figure 3.8. This open loop correction assumes full linearity between actuators and no hysteresis, which accounts for the larger wavefront error. Running through a full interaction matrix sequence with all 37 actuators pushed and pulled to their maximum deformation leaves a residual shape on the mirror different to that before the sequence started. In closed loop operation these hysteresis effects are nullified although they do have the effect of reducing correction bandwidth. The effects of having to flatten a deformable mirror for an AO system are reduced dynamic range of correcting devices and additional wavefront aberration assuming non-perfect correction.

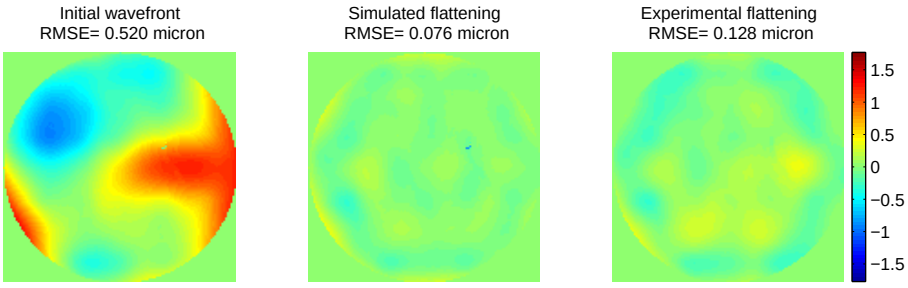

FIGURE 3.8: Initial aberration from bias, with simulated and experimental flattening results for OKO37PZT. The larger values of experimental flattening can be attributed to the open loop nature of the correction with control signals calculated from interferometer measurements.

For every wavefront to be corrected by a deformable mirror there is an optimum number of mirror modes and pupil diameter which depend on the spatial profile of the wavefront, the spatial response of the mirror and wavefront sensor noise. Optimal wavefront correction is usually achieved by limiting the spatial resolution of a DM through truncation of W. Small singular values in W lead to large gains in the control matrix which results in actuator saturation and reduced performance. Likewise reducing the DM aperture can benefit performance with outside actuators showing improved fitting. Whilst reducing mirror modes and aperture diameter limits the spatial resolution of a correcting device it does increase fitting performance to lower order aberrations. Using a sample of 100 wavefronts of atmospheric turbulence the fitting performance was calculated as a function of aperture ratio and truncated mirror modes. These optimum values are calculated for a mean turbulence strength of $D/r_0 = 9$. From sample to sample the optimum value of both parameters would vary. It may be possible to improve performance in real adaptive optics system by dynamically monitoring the strength of aberration and adjusting aperture and modes as appropriate. The optimum aperture for the OKO37PZT was found to be 0.92 of its full reflective aperture. Using a condition factor of 1/20 the first singular value, V is truncated so that only the first 36 modes are used (figure 3.7). The noisy 37th mirror mode can be viewed in figure 3.6. This matches the optimum number of mirror modes found through simulation (figure 3.9).

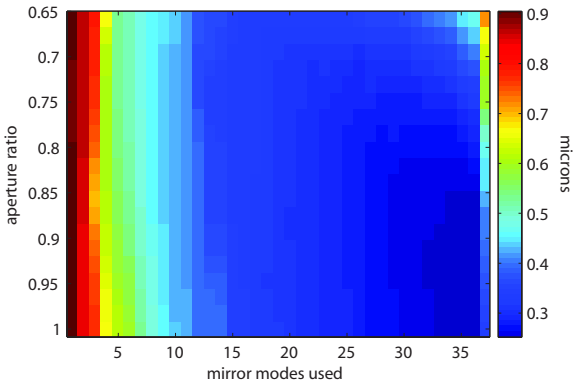

FIGURE 3.9: Average RMS wavefront aberration as a function of mirror modes and aperture after simulated fitting of OKO37PZT to generated atmospheric wavefronts. Increasing the number of mirror modes used in fitting improves correction performance up to the 36th mode. Reducing the amount of mirror aperture used also improves performance up to a point before the outer ring of actuators become redundant and correction decreases.

3.3 Continuous membrane microelectromechanical deformable mirrors

Deformable membrane mirror technology[56] dates back to the 1970's[50] and has found limited use in adaptive optics systems. Poor dynamic range and sensitivity to vibration have limited their usage in astronomical AO. As a counter to this, membrane DMs have no hysteresis or inertial effects. By using micro-electromechanical design methods membrane technology is becoming increasingly useful with small DMs with large numbers of actuators now being manufactured.

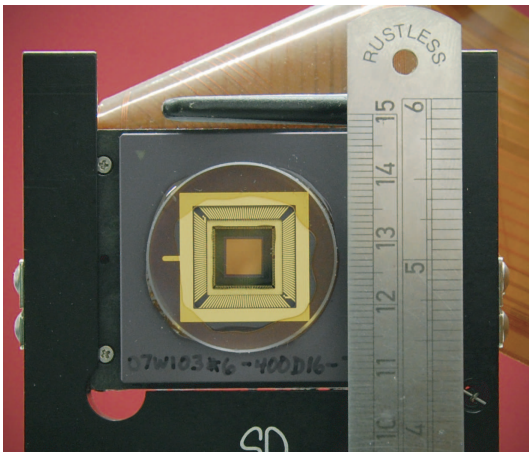

FIGURE 3.10: BMC140 with attached housing and control wiring.

The mirror under consideration here is the 140 actuator Micro-ElectroMechanical System (MEMS) mirror developed by Boston Micromachines Corporation (BMC)[57][58]. A mounted version of this mirror can be seen in figure 3.10. This mirror uses a surface micromachined silicon membrane which is deformed electrostatically by a 12×12 array of electrodes (figure 3.11). A poly-crystalline silicon electrode forms a parallel plate capacitor with the grounded actuator membrane. By applying a voltage to the underlying electrode the membrane is deflected downward. A mirror membrane is coupled to the actuators through small mechanical posts. This parallel plate capacitor produces a pressure equal to

$$P = \frac{\epsilon_0 V^2}{d^2} \tag{3.7}$$

where ϵ is the permittivity of free space V is the voltage applied and d is the separation

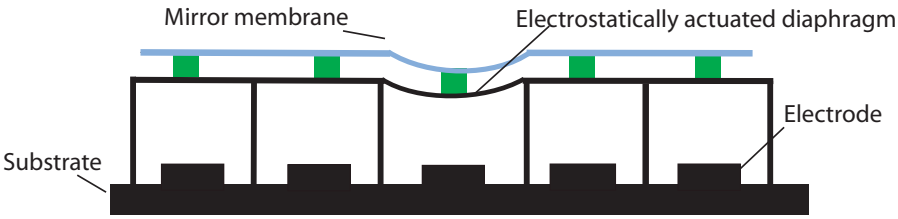

FIGURE 3.11: Schematic of the BMC140.

between electrodes. The steady state defection for this arrangement is

$$\nabla^2 z = \frac{-P}{T} \tag{3.8}$$

with T being the membrane tension.

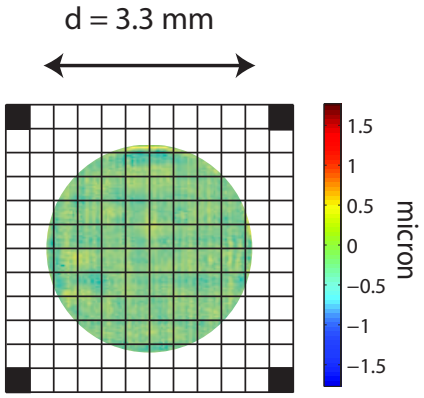

FIGURE 3.12: Actuator geometry, pupil diameter and initial aberration of the BMC140.

- The mirror (Boston Micromachines Multi-DM) has 140 actuators arranged on a square grid with the corner actuators missing (figure 3.12)
- Each actuator has $400\mu m$ pitch and influence functions with full-width half maximum of $550\mu m$ corresponding to 26% coupling between actuators
- The total available stroke is listed by the manufacturer as $3.5\mu m$
- $4.4mm$ reflective aperture fixed at the edges
- Initial RMS wavefront aberration of $96nm$
- 500Hz maximum operating frequency

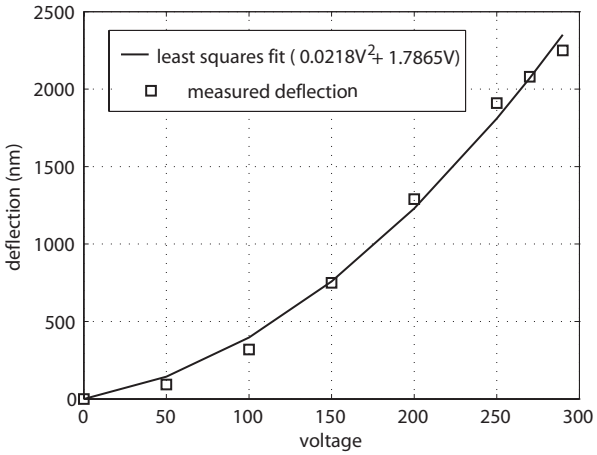

FIGURE 3.13: Phase response to actuator voltage with least squares fitting for BMC140.

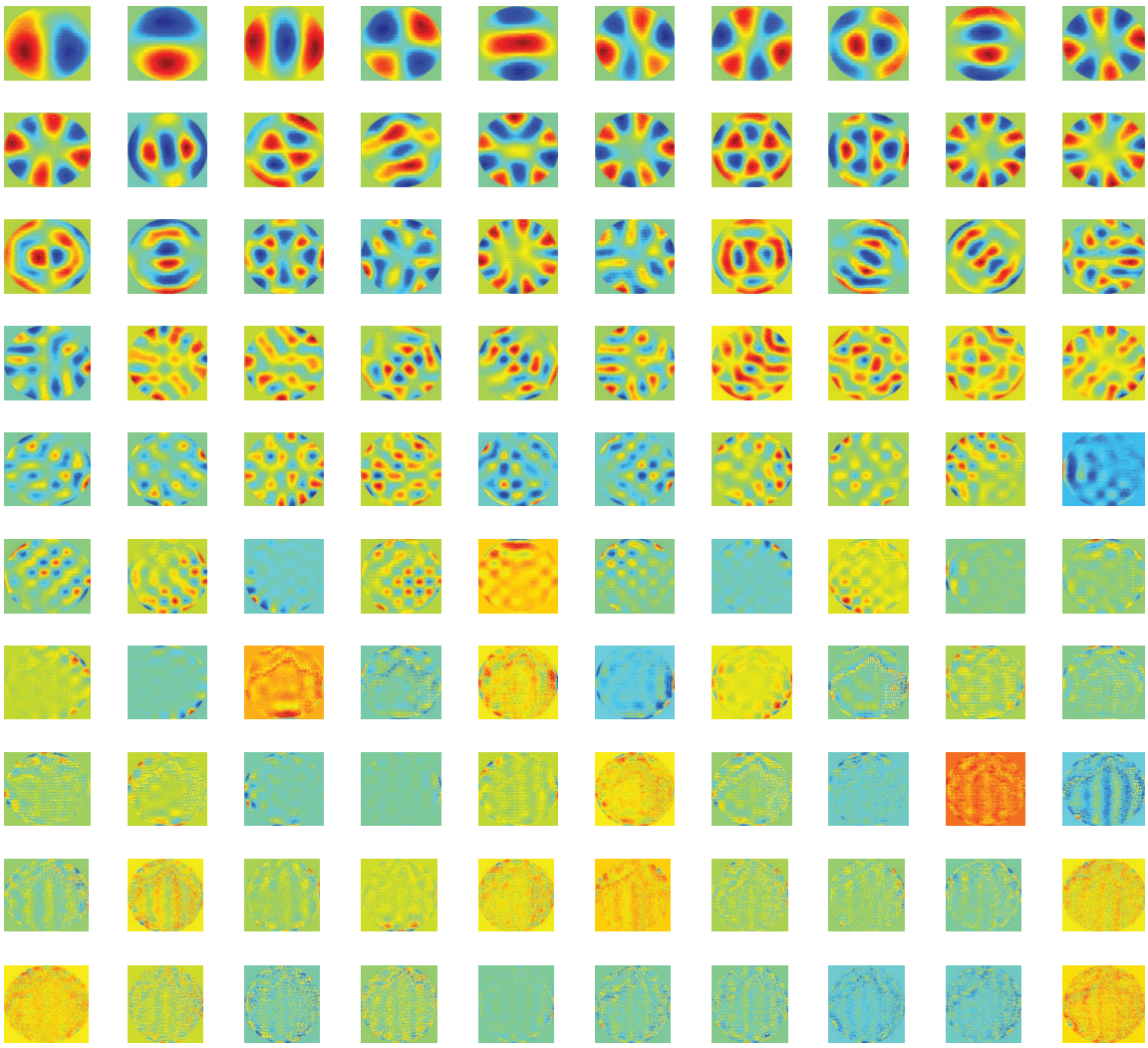

FIGURE 3.14: First 100 orthogonal mirror modes for BMC140 obtained by SVD

Mechanical displacement using electrostatic actuators is a non linear effect usually proportional to the square of the input voltage. Over the range $0 - 290V$ a single actuator displays this non-linear behavior (figure 3.13). By grouping actuators together a more linear deformation is observed becoming completely linear at 3×3 actuator pokes. As actuation only occurs uni-directionally it is necessary to bias the actuators to some default position to allow positive and negative corrections. The phase response to voltage needs to be fully understood to allow for maximum range of stroke and to reduce closed loop corrections errors.

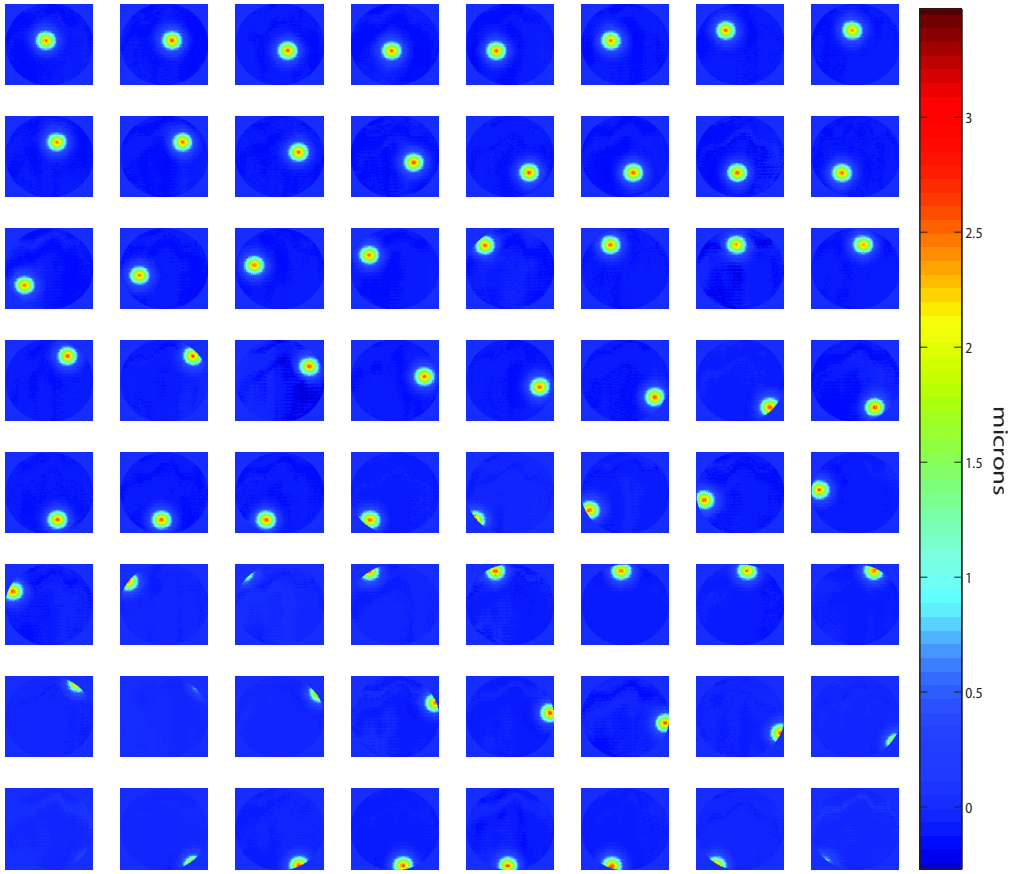

FIGURE 3.15: First 64 influence functions for BMC140 increasing radially outwards

By constraining the optical pupil of the BC140 to $3.3mm$ the influence of outside actuators is reduced to near zero effectively making it a 100 actuator DM. The fixed boundary edge does not allow for free movement of these actuators and their inclusion would lead to sub-optimal performance. The influence functions for the first 64 actuators are shown in figure 3.15 beginning with the innermost actuators. Using singular value decomposition an orthogonal set of mirror modes is obtained for this mirror, the first 100 modes of which are shown in figure 3.14. The corresponding singular values can be

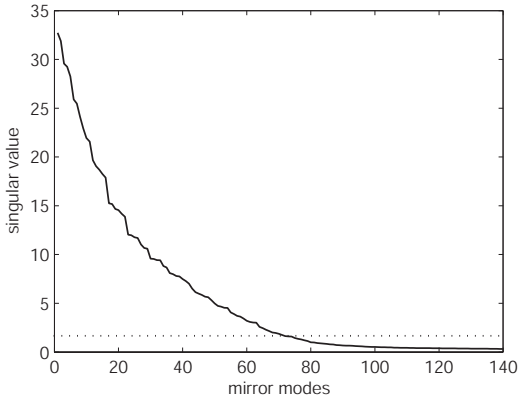

FIGURE 3.16: Singular values W for the BMC140

seen in figure 3.16. Using a condition factor of 1/20 the first singular value the cutoff point would be reached at the 72^{nd} mirror mode.

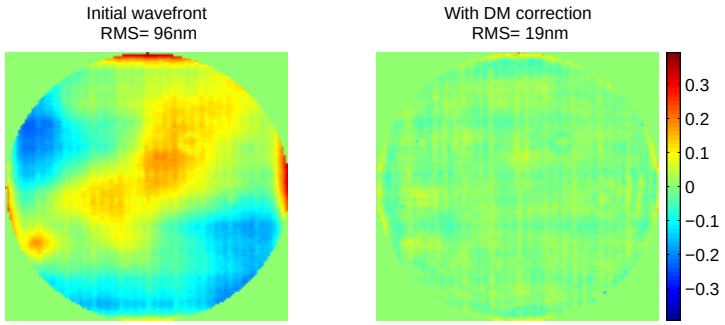

FIGURE 3.17: Initial aberration from bias, with simulated flattening results for BMC140

The BMC140 exhibits $\lambda/8$ flatness when used with $632nm$ light and at its bias position. This can be reduced to 19nm RMS residual wavefront error by self correction (figure 3.17). Closed loop AO correction should yield a similar level of flatness. Sub-nm flattening has been demonstrated on a 1024 actuator MEMS mirror developed by Boston Micromachines[59] which makes these DMs ideal for extreme adaptive optics correction[60] and as tweeter mirrors in a woofer-tweeter configuration[61].

The optimum number of modes and aperture diameter has been estimated for the BMC140 (figure 3.18). Again this is calculated for atmospheric turbulence with strength of $D/r_0 = 9$. The value of D is 3.3mm here and not the full $4.4mm$ reflective surface of the mirror. The optimum number of mirror modes was found to be approximately 100 although average correction does not vary much whether 80-140 modes are used. The optimum aperture diameter is reached at $3.3mm$.

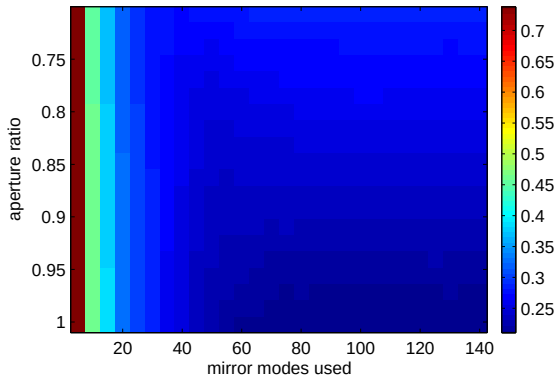

FIGURE 3.18: Average RMS wavefront aberration as a function of mirror modes and aperture after simulated fitting of BMC140 to generated atmospheric wavefronts. Unlike the OKO37PZT in 3.9, the BMC140 does not improve correction performance as the aperture is constricted.

3.4 Atmospheric compensation

In this section the atmospheric fitting performance of a number of DMs is simulated. The spatial characteristics of each mirror as defined by their experimentally obtained actuator influence functions are used to calculate the expected wavefront compensation. Atmospheric wavefronts used are simulated according to Komologorov turbulence statistics.

When light is imaged through the Earth's atmosphere a degrading effect is observed on the image formed. This is true for astronomical observations, satellite imaging and horizontal path laser propagation. The nature of this aberration is well understood by the statistical approach of Kolmogorov and Tatarski. Roddier[26] gives a concise overview of this theory which I have also described in section 2.4. In summary the structure function of atmospheric phase at a point which is a distance r from an initial point x is

$$D_\phi(r) = \langle | \phi(x) - \phi(x+r) | \rangle^2 \tag{3.9}$$

This structure function is defined by Fried[28] as

$$D_\phi(r) = 6.88 \left(\frac{r}{r_0} \right)^{5/3} \tag{3.10}$$

The Fried parameter, r_0, is a measure of turbulence coherence length or atmospheric seeing and usually ranges from $5 - 20cm$ at visible wavelengths. A circular area of

turbulent phase with diameter r_0 has approximately 1 radian RMS phase error. The variable r_0 is characterised by

$$r_0 = [0.423\frac{2\pi}{\lambda}(cos(z))^{-1}\int C_N^2(h)dh]^{-3/5} \tag{3.11}$$

with C_N^2 being the refractive index structure constant, h the height of turbulence layer and z is the zenith angle. From 3.11 it is evident that $r_0 \propto \lambda^{6/5}$. Therefore the scale of aberration to be corrected by an AO system decreases with wavelength.

Noll[62] describes the statistics of atmospheric turbulence in terms of a Zernike basis. A wavefront can be decomposed onto this basis as

$$\phi(x) = \sum_{i=1}^{\infty} = a_i Z_i(x) \tag{3.12}$$

where Z_i are the Zernike modes and a_i are the corresponding coefficients. The residual phase variance when n modes are corrected from a wavefront are given as

$${\sigma_{fit}}^2 = a_N \left(\frac{D}{r_0}\right)^{5/3} \tag{3.13}$$

The value for a_N when tip/tilt is removed is 0.134. The number of actuators required for correction is proportional to $(D/r_0)^2$. Using a zonal approach for a deformable mirror with actuator pitch d, the wavefront fitting error is given by

$${\sigma_{fit}}^2 = \alpha \left(\frac{d}{r_0}\right)^{5/3} \tag{3.14}$$

where α is an actuator influence function coefficient

The number of actuators N in a given pupil diameter D is $N = (D/d)^2$. The fitting error can then be expressed as

$${\sigma_{fit}}^2 = \alpha \left(\frac{D}{r_0}\right)^{5/3} N^{(5/6)} \tag{3.15}$$

Greenwood[63] gives coefficient α as 0.274 whilst Tyson[64] indicates a more conservative value of 0.5 which takes account of the reduced wavefront fitting at the edges of constrained DMs. This fitting coefficient varies between $0.14 - 1.3$ for different actuator types. Using equation 3.15 with $\alpha = 0.274$, diffraction limited performance (Strehl ratio

> 0.8 or fitting error less than 0.223rad^2) for an 8 metre telescope with $r_0^k = 0.8m$ would require 128 actuators.

The stroke of a DM is the peak to valley optical deformation. The RMS wavefront error for turbulent wavefronts (with infinite outer scale) with piston and tip/tilt modes removed is shown in figure 3.19 . To correct for $\pm 3\sigma$, capturing 97% of wavefront deviations[65], a mirror will need to have stroke S equal to

$$S = 2\frac{\lambda}{2\pi}\frac{3}{2}\sigma_{fit} \tag{3.16}$$

A plot of this function for r_0 in the K band is shown in figure 3.19. Mirrors which do not

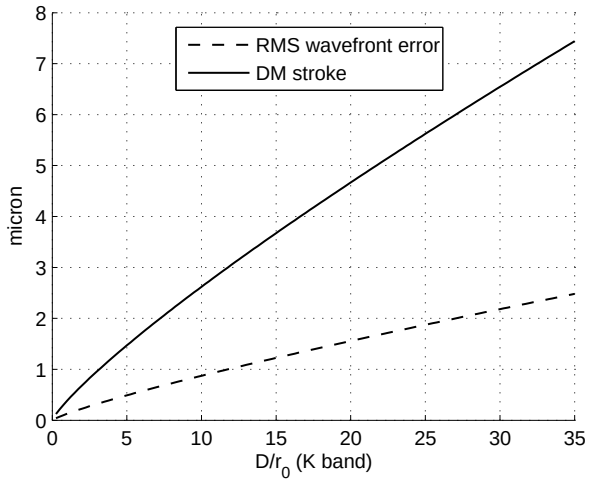

FIGURE 3.19: Wavefront phase variance as a function of turbulence strength (tip/tilt removed and with infinite outer scale) including stroke requirement

have enough range for a particular wavefront will give partial correction. Saturation and control clipping can also occur with high gain mirror modes when actuator commands given by equation 3.6 are clipped to a specified range to avoid detrimental high voltage loads or for the purposes of simulation, unrealistic performance. The residual wavefront is given by

$$\phi_{residual} = \phi_{initial} - Mf(c) \tag{3.17}$$

with clipping function $f(c)$ limited by maximum voltage $\pm c_{lim}$ given as

$$f(c_i) = \begin{cases} c & if -c_{clim} \leq c_i \leq c_{lim} \\ \frac{c_{lim} c_i}{abs(c_i)} & if c_i < -c_{lim} or c_i > c_{lim} \end{cases} \tag{3.18}$$

The stroke requirements are non uniform over DM aperture due to the non-stationary nature of wavefronts which have Zernike modes removed. Conan[66] has shown that when tip/tilt and piston is fully removed from Kolmogorov wavefronts the RMS residual at the edge of the pupil is 35% more than that in the centre. This effect is dependant on the size of the outer scale, L_o and on the number of modes corrected. If we consider the situation where the piston or tilt component of some atmospheric aberration extends beyond the telescope aperture and is zero at the centre of the aperture. Moving away from the centre of the aperture the wavefront will deviate from this zero point. Removing this component will ensure that the middle area of the aperture will have less wavefront variance than at the edges due to the spatial statistics of Kolmogorov turbulence. Figure 3.20 gives an illustration of this effect for 1000 Kolmogorov wavefronts with strength $d/r_0 = 9$ and with infinite outer scale. Further to this Vdovin[67] outlines the optimum requirement for outer edge actuators when correcting for lower order aberrations.

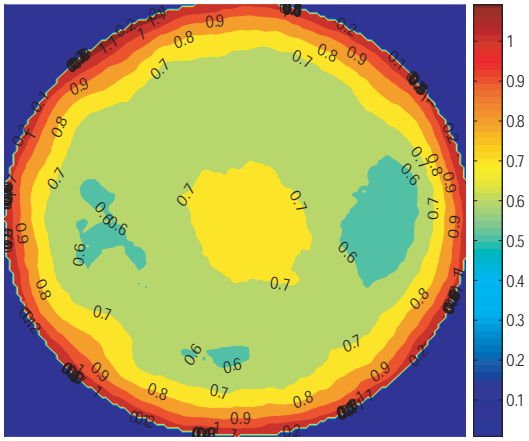

FIGURE 3.20: Phase variance over telescope aperture for 1000 atmospheric wavefronts with piston and tip/tilt removed and infinite outer scale.

It is possible to simulate Kolmogorov turbulence using the Fourier transform of the power spectrum of phase structure functions. Such an approach results in poor low frequency reproduction of Kolmogorov turbulence. A more accurate approach developed by Harding *et al* [68] is to generate a low resolution phase screen from the phase covariance matrix. Higher resolution screens are then interpolated from this initial 'seed'. This resulting screens are a very near match of the ideal structure functions. All turbulence

used in these simulations is generated from this method and from code provided by the authors.

Calculating an average value for $\phi_{residual}$ for each mirror allows judgement to be made on a particular DMs spatial correction performance. This calculation was performed 100 times for each DM with Kolmogorov turbulence simulated at a strength of $D/r_0 = 9$ and with infinite outer scale. For each grid of generated turbulence wavefronts, the mirror commands to minimise and flatten these wavefronts is calcuated through singular value decomposition. Using control signal clipping to replicate actuator saturation the resulting wavefront obtained by a DM is calculated. Subtracting this wavefront from the generated turbulence allows residual wavefront errors to be calculated.

The previous calculations suggest a DM with 130 actuators (square array; ≈ 100 for a circular or hexagonal array) and at least $2.5\mu m$ of stroke is needed to achieve diffraction limited performance. The fitting performance for the OKO37 PZT and the BMC140 as a function of turbulence strength is given in figure 3.21.

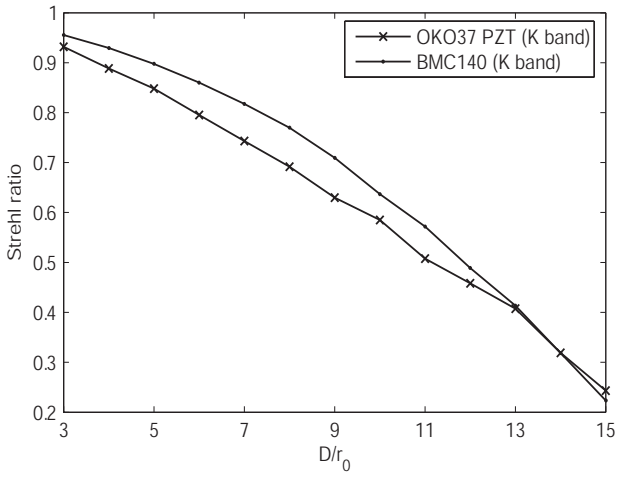

FIGURE 3.21: wavefront phase variance as a function of turbulence strength (tip/tilt removed) including stroke requirement

The main parameters that influence spatial wavefront fitting are

- Actuator density (or d/r_0)
- Individual actuator stroke and total DM stroke
- Geometrical arrangement of actuators

- Influence function shape and cross talk
- linearity of superimposed influence functions
- Flatness of mirror surface which serves as the upper limit of achievable correction

The importance of actuator stroke in an operational adaptive optics system for a telescope extends beyond slightly reduced performances as the mirror falls short of the wavefront shape required. When used in closed loop any shortfall in mirror shape by actuator clipping can be quickly exacerbated through loop instabilities. Control loop gains are carefully calculated to avoid oscillations and are based on the assumption that the mirror surface will closely approximate the required shape. Actuator clipping will result in successively severe oscillations if this is not the case. There are other issues which can effect the dynamics of closed loop wavefront fitting such as hysteresis and actuator response linearity but these can be accounted for by careful dynamic consideration based on the temporal filter used.

A wide variety of mirrors were used for this comparison including (figure 3.22)

- OKO19PZT : 19 actuator version of OKO37PZT with $3-8\mu m$ of stroke for different rings of actuators
- AOptix35 : This 35 actuator bimorph mirror is developed by AOptix technologies and uses two layers of lead magnesium niobate (MPN) which is bonded to electrodes. The inner ring of electrodes is capable of producing curvature deformations whilst the outer ring produces linear slope. The total stroke available to the mirror is $16\mu m$ with individual actuator stroke varying from $3\mu m$ at inner actuators to $7\mu m$ for the outer ring.
- OKO37MMDM : This micro-machined membrane mirror has a 15mm diameter with actuators arranged on an hexagonal array.
- AgilOptics37 Developed by Agil Optics this is another MMDM with similar properties to the OKO37PZT. Individual actuator stroke varies from $0.2-0.6\mu m$ with total stroke of $4.5\mu m$. As is the case with fixed edge membranes optimal pupil is about 2/3 of mirror diameter.

- MIRAO52 : Developed by Imagine Eyes this DM uses magnetic actuation to with a maximum stroke of $50\mu m$ possible although this is limited to $25\mu m$ in practice on the advice of the manufacturer.

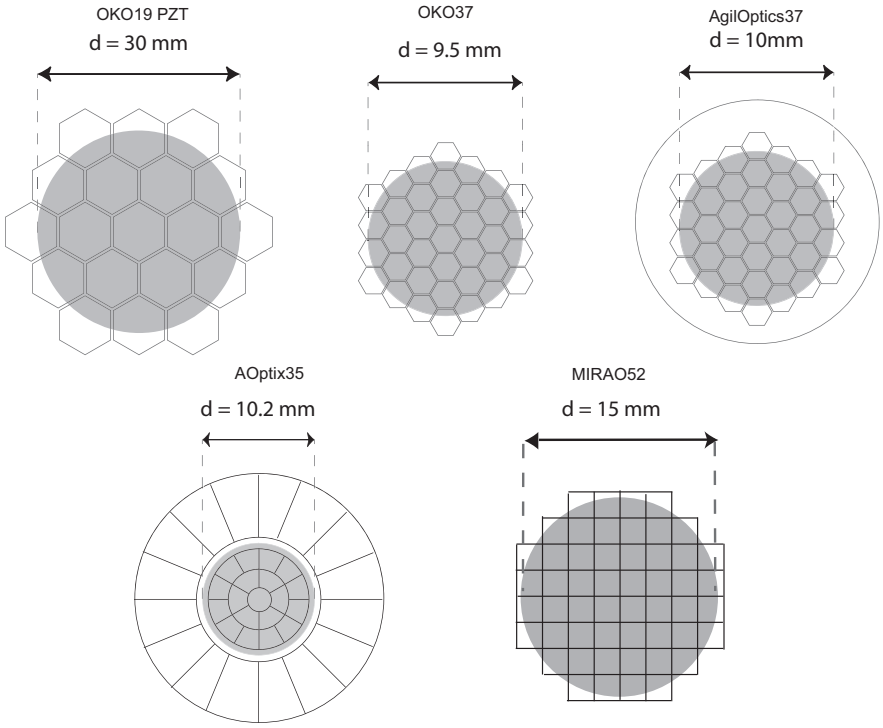

FIGURE 3.22: Actuator geometry and pupil diameter for all mirrors

The mean Strehl ratio calculated at $2.2\mu m$ for each mirror is shown in figure 3.23 with standard deviation error bars for the 100 samples included. The residual wavefronts for a single sample of turbulence is shown in figure 3.24. Figure 3.25 gives an insight into the spatial frequency content for each mirrors residual. The main results and conclusions from this study are,

- The AgilOptics37 and OKO37 are of the same specification and technology type with both performing poorly. Actuator number and geometry cannot makeup for the low amount of individual actuator stroke that micro-machined membrane mirrors produce. Overall stroke for these mirrors may be over $3\mu m$ but this might only be for very low order defocus or coma aberrations. To maximise performance the number of mirror modes is attenuated to 11 for the OKO37 and only 7 for the AgilOptics37. These mirrors are in effect correcting for the very lowest Zernike radial orders (2nd-3rd). These mirrors would only be suitable for very small telescopes where D/r_0 would be below $4-5$.

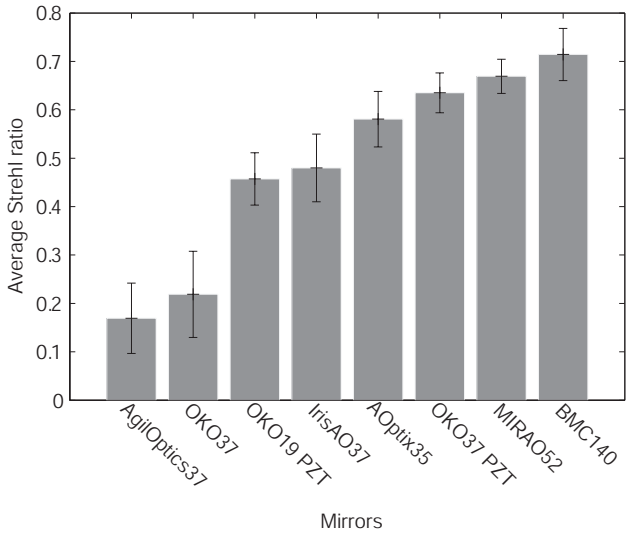

FIGURE 3.23: Mean Strehl ratio after fitting to turbulent wavefronts

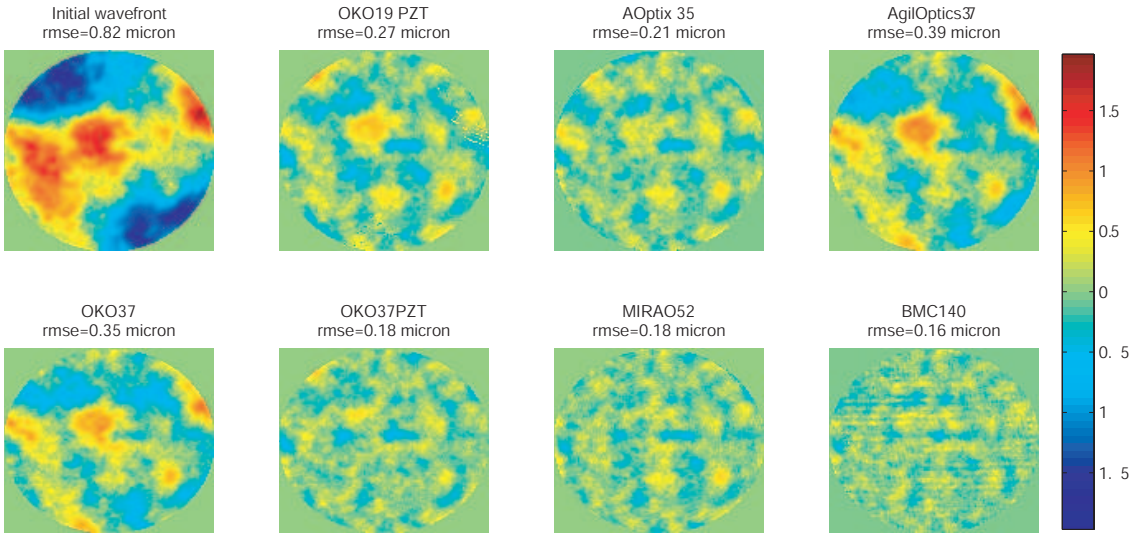

FIGURE 3.24: Residual wavefronts for each mirror after correction for one sample of simulated turbulence

- The OKO37PZT has a similar specification to the OKO19PZT which has one less ring of actuators. This is reflected in its increased spatial fitting error with a Strehl ratio of 0.64 compared to 0.46. Both mirrors show good low order correction with the OKO37PZT having lower RMS residual error for all Zernike radial orders. With the relatively large $30mm$ aperture both these mirrors would be suitable for atmospheric correction in a small telescope system.

- The only bimorph mirror in this study, the AOptix35 performs well with an average Strehl ratio of 0.58 . Despite its large amount of available stroke mirror modes

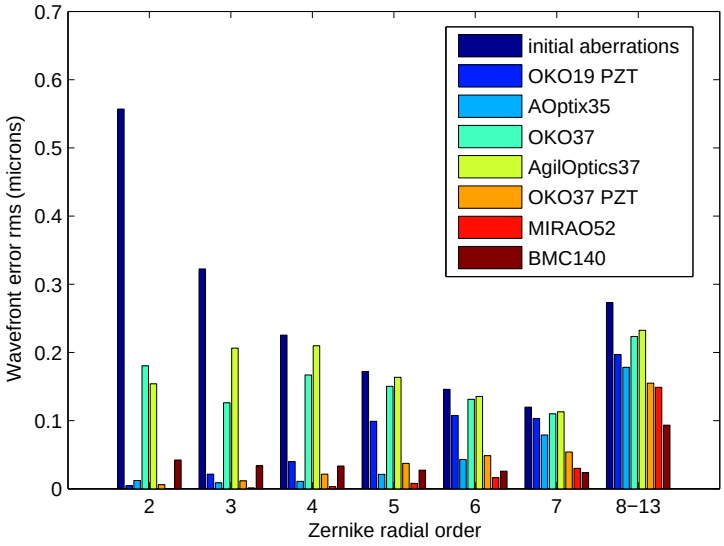

FIGURE 3.25: Mean norm of the turbulent wavefront residuals for each Zernike radial order

were clipped to 32 of 35 available to negate the effect of the noisier modes. The mirror exhibits good initial low order correction up to the 6th Zernike radial order but is limited by its 35 actuators.

- MIRAO52 : This mirror has the second best fitting to atmospheric wavefronts of the deformable mirrors in this study. It also had the most stable correction performance which can be attributed to its large amount of available stroke. In practice, this mirror would struggle due to its slow dynamic speed of operation.

- Boston Micromachines produce the best overall performing mirror at this strength of turbulence. This is due to its large number of actuators (100 only used) and reasonable $1.5\mu m$ individual actuator stroke. The influence functions of all 140 actuators were recorded but only 100 mirror modes are used in calculations. Spatial correction at the lower modes isn't as good as other mirrors due in part to its square geometry. Overall correction throughout the spectral range is very good.

3.5 Conclusion

In this chapter an overview of deformable mirrors for adaptive optics was shown with the wavefront fitting performance of 8 commercially available mirrors calculated. When

tasked with minimising atmospheric wavefronts the best performing mirrors had sharp well defined influence functions, adequate stroke and actuator numbers. Dynamic effects and other practical issues are ignored in this spatial fitting comparison. In choosing a DM for practical usage its important to ensure that it is well matched to whatever particular aberration is expected, robust enough for the environment and costs no more than is necessary.

Some of the results from this chapter have been presented at conferences and have been published[69][70][2] as part of wider studies into the fitting of deformable mirrors for both astronomical and ophthalmological use.

Chapter 4

Woofer Tweeter Adaptive optics

4.1 Introduction

The use of dual deformable mirrors is not a new concept in adaptive optics. Dual deformable mirrors are being used in AO systems to extend the field of view[40] and to correct for amplitude variations in lasers[71]. Extending AO systems beyond a conventional single deformable mirror allows wider field corrections such as multi-conjugate AO[72] and ground layer AO[42] to be performed. By treating the atmosphere as a volume of turbulence, each mirror (possibly more than two) corrects for a particular altitude conjugation. There has also been a considerable amount of research in correcting phase and scintillation errors in high power laser systems[73]. The earliest use of dual deformable mirrors arose when Tip/Tilt (TT) mirrors where paired with higher order mirrors. The use of Woofer Tweeter Adaptive Optics (WTAO) can be considered an extension of these dual mirror systems. Tip/tilt mirrors are necessary to correct for the large amplitude X and Y jitter caused by atmospheric turbulence and wind shake. Whilst a normal deformable mirror may have sufficient dynamic range to correct for these motions, it is limiting both to the overall performance and cost of a system. The use of a lone tip/tilt steering mirror can have a significant effect on long exposure image quality in astronomy. The maximum amount of tip/tilt as derived from Tyson[32] is

$$\alpha_{tip} = 1.075 \left(\frac{D}{r_0}\right)^{5/6} \frac{\lambda}{D} \tag{4.1}$$

Total angular stroke for a tip/tilt mirror will be 2.5 times the standard deviation which captures 99.5% of wavefront excursions. A demagnification effect occurs due to the limited diameter of tilt mirror and the angular motion is multiplied by a factor of D/D_{TT} where D_{TT} is the diameter of the tip/tilt mirror. Combining these, the total angular stroke requirement is

$$\alpha_{tip} = \pm 1.1 \left(\frac{D}{r_0}\right)^{5/6} \frac{\lambda}{D_{TT}} \tag{4.2}$$

For an 8m telescope with $r_0 = 0.8$m in the K band and a 20cm tip/tilt mirror the angular stroke requirement is 17 arcseconds or 16μm. Whilst there are deformable mirrors that can satisfy this requirement many would not be suitable for astronomical and historically such mirrors have not been available. In practical execution the effects of wind buffeting on the telescope will dictate that much larger tip/tilt angles be corrected although this is not a technical challenge for a dedicated tip/tilt mirror. It does make it entirely unfeasible to use a higher order DM to correct for these large angular deviations. These calculations assume an infinite outer scale and a smaller outer scale would reduce this figure. In any case a tip/tilt mirror would still be used so there is no net gain in imaging from a smaller outer scale.

4.2 Deformable mirror requirements for astronomy

In section 3.4 I gave an account of the main requirements for deformable mirrors for astronomy. The two main parameters that effect AO performance are degrees of freedom and stroke. As telescope apertures get larger so to does the volume of turbulence to be corrected resulting in higher spatial frequencies and larger PV wavefront excursions. Greenwood[63] has shown how the fitting error is effected by actuator spacing d as

$$\sigma^2_{fit} \approx \alpha \left(\frac{d}{r_0}\right)^{5/3} \tag{4.3}$$

The coefficient , α, depends on the type of actuator used with a value of 0.5 being an average value and was used previously in chapter 2. For segmented mirrors with piston only actuation ($\alpha \approx .134$), piston and tip/tilt actuation ($\alpha \approx 1.03$), diffraction limited performance($SR = 0.8$ or $\sigma^2 \leq 0.22 rad^2$) is achieved when $d/r_0 \leq 0.4$ and $d/r_0 \leq 1.36$

respectively. As telescopes increase in size the actuator density requirement increases to the 5/3 power. Figure 4.1 illustrates this effect for apertures of $4 - 42m$ size, with the $42m$, European Extremely Large Telescope[74] currently being the largest telescope in planning. Requirements become prohibitively severe as the observation wavelength decreases from the K band.

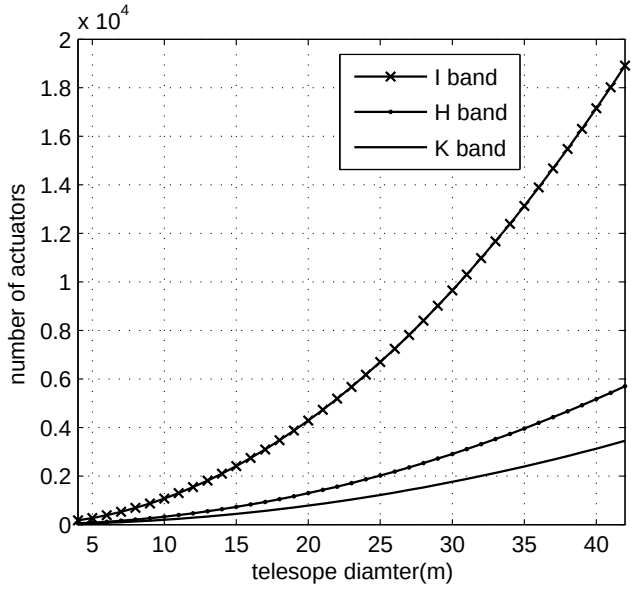

FIGURE 4.1: Number of actuators required to achieve diffraction limited performance on AO equipped telescopes. This assumes an infinite outer scale and a continuous facesheet deformable mirror.

Stroke requirements are generally not as severe for larger telescopes and are independent of wavelength. With tip/tilt removed Noll[62] gives the remaining wavefront variance due to atmospheric turbulence as

$$\sigma_{fit}^2 = 0.134 \left(\frac{D}{r_0}\right)^{5/3} \tag{4.4}$$

The stroke required is then 3 times the root mean square wavefront error[65]

$$S_{req} = \frac{3\lambda}{2\pi} 0.366 (D/r_0)^{5/6} \tag{4.5}$$

with a less severe 5/6 power dependency on aperture diameter. In figure 4.2, the impact of varying seeing conditions on stroke requirements is evident. For the ELTs, mirrors will need to be capable of at least 10μm to avoid being limited by poorer than average seeing conditions. To fulfil its science requirement the TMT project have specified a need for a deformable mirror with $10,000$ actuators and 11μm of stroke[75].

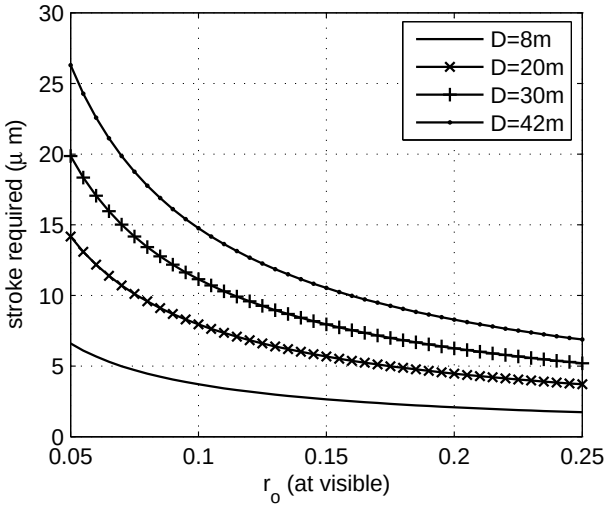

FIGURE 4.2: Deformable mirror stroke requirements for varying seeing conditions and different telescope sizes assuming an infinite outer scale

If adaptive optics is to be implemented for wavelengths approaching the visible on telescopes of $30m$ or more diameter, a very high spatial frequency deformable mirror is required and one which is capable of a relatively large amount of stroke. This is the engineering problem that faces the astronomy community and one that has been recognised by Ellerbroek since 2001[76].

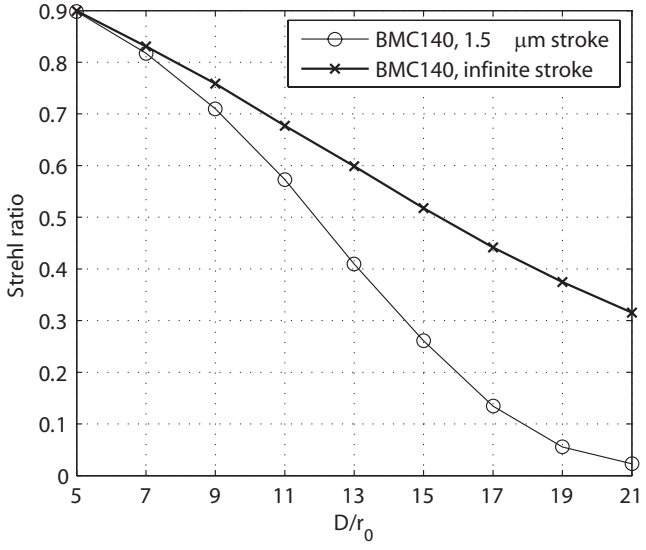

FIGURE 4.3: Strehl ratio after fitting 100 Kolmogorov wavefronts with infinite outer scale. The stroke limited ($1.5\mu m$)tweeter in this instance has the spatial characteristics of the BMC140 mirror but with clipped actuator range. This hypothetical mirror has increasingly poor correction as turbulence strength is increased whilst a mirror with infinite stroke shows better correction. The gap between the two show the potential gains of using WTAO by not being limited by mirror stroke.

The aim of using dual mirrors is to remove the large amplitude low order aberrations so that the tweeter can then achieve high order correction without being limited by stroke. In figure 4.3 the performance of a BMC140 with $1.5\mu m$ stroke in fitting atmospheric wavefronts is plotted as a function of turbulence strength. By setting the actuator clipping to an approximately infinite number the effects of having no actuator clipping for this mirror are seen. Immediately there is better correction at stronger amounts of turbulence with any performance decreases due to the increasing higher spatial frequencies. This idealised deformable mirror serves as an upper limit to AO correction for that mirror when used with a woofer. The spatial control schemes used to achieve WTAO correction and their simulated performance is the subject of the following sections.

4.3 Woofer-tweeter control methods

The spatial control of dual deformable mirrors at a single conjugate is understandably more complex than for the usual TT/DM combination. The optimum method for WTAO is the one which produces the highest Strehl ratio and minimises the stroke requirements for both woofer and tweeter. These two conflicting requirements are constrained by imaging demands and/or available technology. Controlling two mirrors simultaneously creates issues around loop stability especially when one mirror counters the phase of the other. There are a number of control methods already mentioned in literature to achieve WTAO correction. These are;

- Zonal WTAO (Dual deformable mirror) : Control signals are obtained from inversion of a concatenated interaction matrix for both woofer and tweeter[61]
- Modal de-project: A derivative of [61]. Woofer modes are de-projected from tweeter and control signals are computed separately for both woofer and tweeter
- Split Zernike: Aberration is decomposed into Zernike terms and each mirror corrects for a spatially filtered wavefront[77]
- Dual step: This approach was used for ocular adaptive optics[78][79] with success but will be difficult to implement for dynamic turbulence. It is of interest as a possible indicator of maximum performance for dual deformable mirror adaptive

optics. The group responsible are the only persons using WTAO for ophthalmological applications. They have recently suggest a modified version of the zonal WTAO[80] method which could be useful for for turbulence oriented WTAO.

By investigating a number of the above methods through simulation and experiment and optimal solution to the problem is found.

4.3.1 Dual step

This is the simplest of control methods resembling two separate standard AO loops with duplex operation. Its success in ocular AO can be attributed to the relatively stationary low order aberrations which the woofer corrects, leaving the tweeter with high spatial frequency and high temporal frequency aberrations. In the event of dynamic low order aberrations, the system would not be able to account for these changes. The temporal coherence of atmospheric turbulence is such that any fixed low order correction will be entirely uncorrelated within a fraction of a second. If correction was multiplexed at a high enough frequency then this system might be possible in astronomy but closed loop stability could be very difficult to achieve. It may however be the most efficient way to spatially fit a wavefront using two DMs.

4.3.2 Zonal WTAO

This is the simplest useable method for WTAO where both mirrors interaction matrices are combined to create a virtual master mirror. Three zonal interaction matrices are measured either in phase space or subaperture gradients; tip/tilt D_{TT}, woofer D_W, tweeter D_T. The final interaction matrix to be inverted is just a concatenation of all three.

$$D_z = [D_{TT} D_W D_T] \tag{4.6}$$

Control signals for each mirror are then calculated by inverting D_z using SVD. The mirror modes are now combinations of both woofer and tweeter with the former comprising most of the lower order modes. The singular values for these modes should be clipped at an appropriate point to ensure stability and optimum correction.

4.3.3 Modal de-project

In the zonal WTAO approach, the combinations of woofer and tweeter used in each mode might not be the most efficient use of dynamic range for each mirror. In the modal de-project method, the lower order woofer modes are de-projected from the tweeter influence functions. Again the woofer interaction matrix is W and the tweeter's is T. Projecting the woofer interaction matrix onto the tweeter,

$$P_{TW} = (W)^{-1} T_{tt} \tag{4.7}$$

Here T_{tt} is the tweeter interaction matrix with TT and piston modes de-projected. For all simulations and experiment in this thesis, TT is removed before correction and any residual TT is corrected by the woofer which can easily accommodate small amounts.

$$\begin{aligned} T_{tt} &= T B_t \\ B_t &= I - P_T^{-1} P_T \\ P_T &= PTT^{-1}T \end{aligned}$$

This modal basis B_T contains the actuator commands that remove a particular mode from T. In this case PTT is the WFS or phase space representation of piston and TT stored in column vectors and projected onto the T. With P_T calculated the woofer free tweeter basis

$$B_{TW} = I - P_{TW}^{-1} P_{TW} \tag{4.8}$$

and the final woofer free tweeter interaction matrix is

$$T_W = T B_{TW} \tag{4.9}$$

Correction for both woofer and tweeter can proceed separately with each mirror aiming to minimise the same input phase. The de-projection will ensure that both mirrors correct in an orthogonal manner.

4.3.4 Split Zernike

By decomposing a wavefront ϕ onto an orthogonal Zernike basis Z, a measure of spatial control is achievable.

$$\phi = \sum_{n=1}^{x} a_n Z_n \tag{4.10}$$

This can be separated into a low and high order component from a cutoff mode k.

$$\phi_{woofer} = \sum_{n=1}^{k} a_n Z_n \tag{4.11}$$

$$\phi_{tweeter} = \sum_{n=k+1}^{x} a_n Z_n \tag{4.12}$$

Each deformable mirror is tasked to correct for the appropriate high or low order wavefronts ensuring a degree of separation between mirrors.

4.4 Woofer Tweeter simulations

Performance estimates for each WTAO control scheme are obtained through Monte-Carlo simulation of wavefront fitting. As in the previous chapter, simulated Kolmogorov turbulent wavefronts are fitted to the measured deformable mirror influence functions and residual wavefronts are used to calculate correction performance. Each deformable mirror has its interaction matrix measured experimentally using an interferometer. The singular values obtained through singular value decomposition are shown in figure 4.4 for the zonal WTAO and the modal de-projected tweeter. These singular values describe the sensitivity of a mirror to particular modes with highly sensitive modes causing instabilities when operated in closed loop. For wavefront fitting the de-projected tweeter has its singular values attenuated to the 40^{th} mode to ensure maximum stability of correction for D/r_0 ratios above $10 - 12$. The zonal WTAO control scheme operates best with 80 mirror modes in use for the same strength of turbulence. Using equation 4.9, all woofer modes are removed from tweeter influence functions including tip/tilt modes. Performing a SVD on the measured tweeter influence functions allows us access to the orthogonal mirror modes. In figure 4.5 the effect of de-projecting woofer modes is evident. By de-projecting the woofer modes, the BMC140 is left with modes that are of a much higher spatial frequency. These new tweeter modes are fully orthogonal to

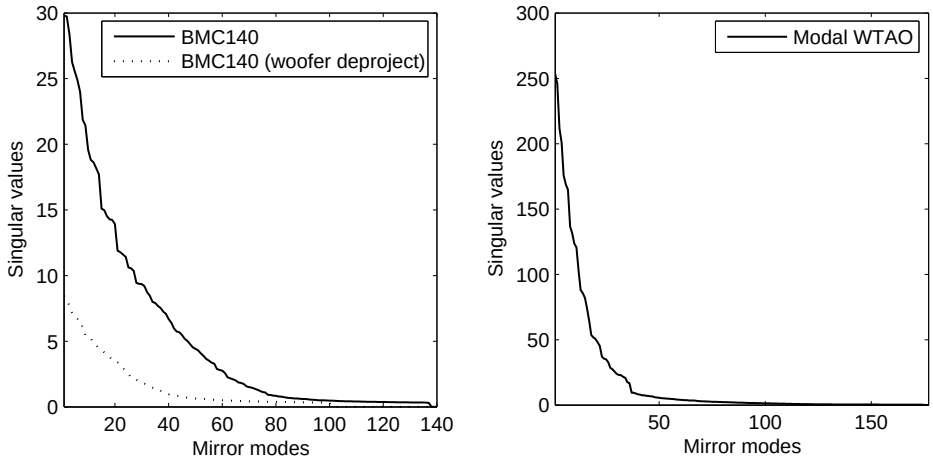

FIGURE 4.4: Singular values for standard tweeter, de-projected tweeter and zonal WTAO control schemes. The cutoff point for these modes is usually set by a condition factor of $S_1/20$ with s_1 being the largest singular value. Depending on the strength of turbulence and loop stability a higher or lower cutoff point can improve performance.

the woofer modes and vice versa. Likewise when the woofer performs a correction, the

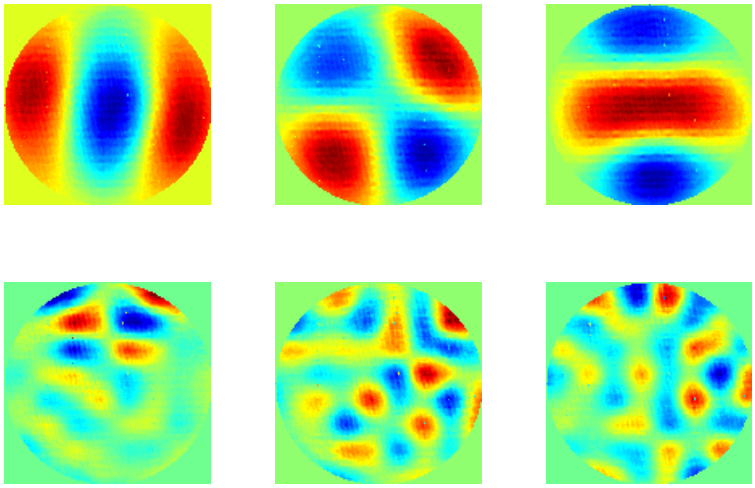

FIGURE 4.5: (top) first three mirror modes for the BMC140 (bottom) first three mirror modes for the BMC140 with OKO37PZT modes de-projected. These latter modes have much more higher spatial frequency content indicating that this mirror will now operate more as a tweeter.

shape it adopts will be beyond the fitting of the modified tweeter influence functions. A visual representation of this is shown in figure 4.6. When the unmodified tweeter is tasked with fitting the woofer shape on the left it does so quite successfully leaving a small residual error. When the de-projected tweeter performs the same task it is blind to this woofer shape.

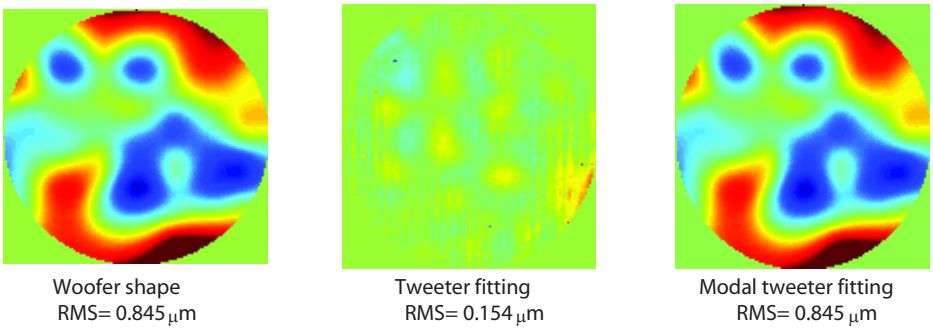

FIGURE 4.6: The phase map on the left shows a typical woofer shape when correcting for turbulence with strength $D/r_0 = 12$. Using the unmodified BMC140 to fit this shape results in flattened surface showing that the tweeter is fully sensitive to woofer modes. When the de-projected tweeter is given the same task it provides zero correction showing itself to be entirely blind to woofer modes.

Using simulations, a measure of performance for the two control schemes is calculated as a function of turbulence strength. The improvement in performance over using a single tweeter mirror is shown in figure 4.7. As the turbulence strength increases past $D/r_0 = 13$ the modal de-project control scheme performs best. The question must be asked, why is this scheme performing better? Is it the most optimum way to use two mirrors?

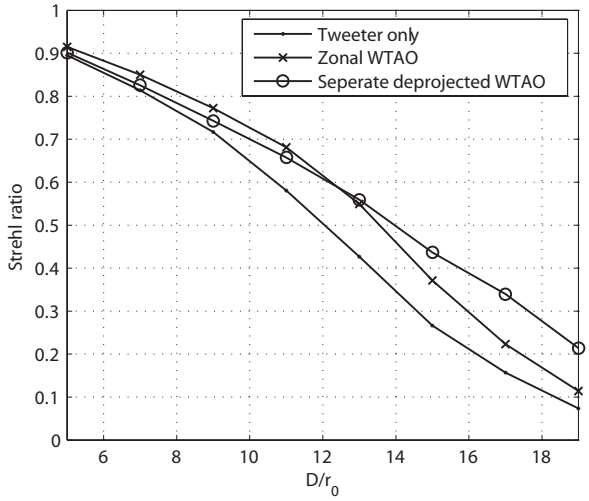

FIGURE 4.7: Average Strehl ratio (100 samples) after wavefront fitting versus turbulence strength for the BMC140, zonal WTAO and modal de-project WTAO. For both WTAO methods dual mirror fitting of the woofer and tweeter is performed with optimal mirror apertures and singular value modes.

It is interesting to view the actual deformations the tweeter makes for each control scheme. In figure 4.8 the resulting shapes are shown for a correction of a single piece of turbulence with strength $D/r_0 = 12$, with the modal de-project method being the most economical with stroke whilst still maintaining similar performance to the zonal WTAO

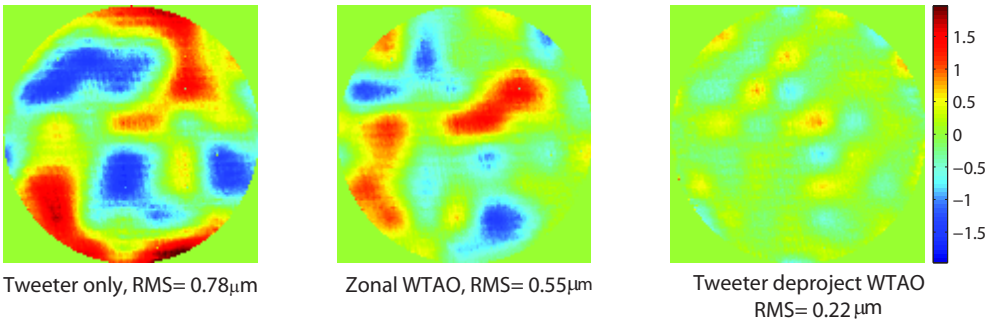

FIGURE 4.8: Tweeter shapes for a single fitting of D/r_0 turbulence. With the tweeter working on its own it has the highest PV deformation whilst still not giving as good overall correction as the dual mirror schemes. The de-projected tweeter shows the least amount of mirror deformation whilst showing it to be the most efficient method.

method. For a hundred samples of D/r_0 turbulence the average PV mirror deformation

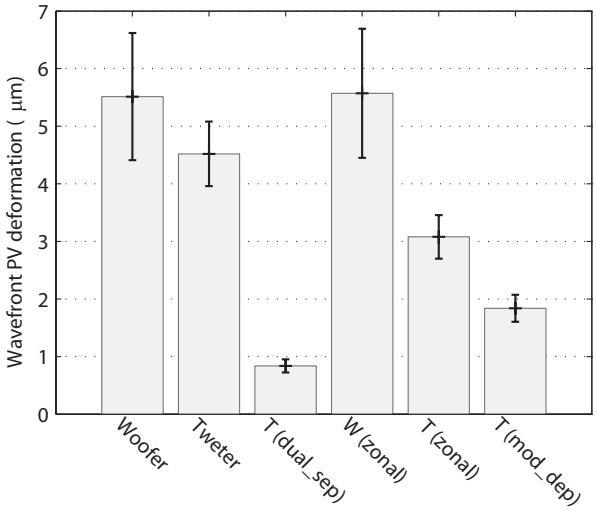

FIGURE 4.9: Average PV mirror deformation for various control schemes when fitted with turbulence of strength $D/r_0 = 12$. The dual step tweeter operates with the woofer. The zonal tweeter operates with the zonal woofer. The modal de-project tweeter operates with the woofer.

was plotted for each mirror and shown in figure 4.9. This shows the different demands placed on the tweeter for the zonal WTAO and de-projected WTAO methods with the zonal method required approximately 50% more stroke. The demands on woofer dynamic range were largely the same. From this we can conclude that both methods place reduced loads on the tweeter with the zonal method requiring the least amount of stroke with no loss in performance.

Another important metric is the number of actuators that are clipped when fitting. A clipped actuator is one that is at its maximum range, occurring when a wavefront is too large in amplitude. It also occurs when higher frequency wavefronts cause saturation of

the smaller mirror modes. This is usually avoided by attenuating these modes through SVD. The average clipping performance for each mirror is shown in 4.10. Despite having

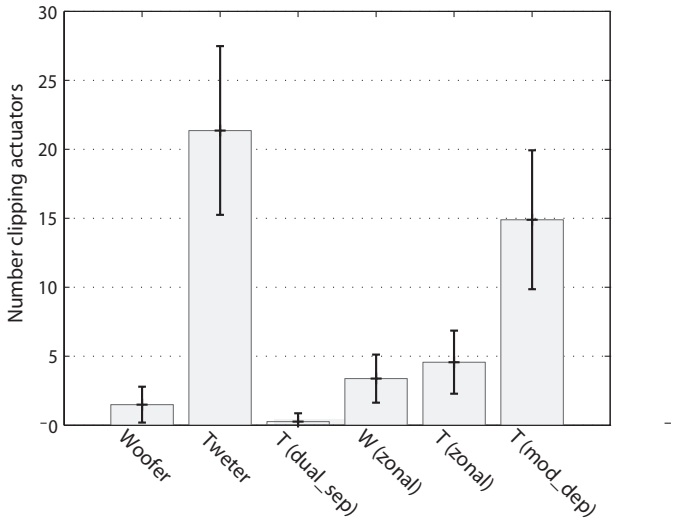

FIGURE 4.10: Average number of clipping actuators for various control schemes when fitted with turbulence of strength $d/r_0 = 12$. Actuator clipping is usually detrimental to wavefront fitting performance. The modal de-project tweeter has the most actuator clipping due to its highly sensitive high spatial frequency mirror modes.

a lower average PV shape the modal de-projected tweeter suffered from actuator clipping to a larger extent than the zonal tweeter which would lead to detrimental performance in a closed loop system. The higher frequency mirror modes for the tweeter in this control scheme tend to have the highest wavefront variances at the edge of the aperture and these highly sensitive mirror modes can easily cause to neighboring actuators to push and pull at full range in order to make some high frequency shape. This doesn't usually manifest itself in wavefront shape as the actuator cross-talk can lead to a cancelling effect. This undesirable operation can be negated by attenuating the modal gains for higher frequency modes but will reduced the spatial fitting properties of the mirrors. This issue needs to be addressed, possibly by reducing the higher frequency woofer modes and allowing the tweeter correct these and finding a more efficient solution that does not lead to tweeter actuator saturation but preserves the high frequency wavefront fitting abilities of the tweeter.

4.5 Conclusions

In this chapter I have described the background to WTAO and the various spatial control schemes associated with this approach. Monte Carlo simulations have provided an insight into expected performance for each control scheme. The modal de-project method shows the most promise with woofer modes being fully de-projected from the tweeter interaction matrices. Having fully independent and orthogonal woofer and tweeter modes leads to better correction performance and should lead to more stable closed loop operation. The PV deformations are also lower with this method despite having more actuators clipping. These simulations are relevant to the experiment which follows, both being based on the same woofer and tweeter. For the purpose of ELTs it maybe more appropriate to simulate for larger apertures and larger deformable mirrors to get a more definitive answer on which spatial fitting scheme is the most appropriate.

Chapter 5

Woofer Tweeter Laboratory Demonstrator

5.1 Introduction

The preceding theory and simulation work has shown woofer-tweeter adaptive optics to be a necessary and viable application of AO technology. Before implementing such systems on ELTs, some intermediary experimental evaluation is needed to fine tune and support the concepts. In this regard I designed a WTAO laboratory demonstrator using two deformable mirrors and an etched phase screen. The aim of this experiment is to verify the WTAO spatial control schemes of chapter 4. By finding the best performing control scheme and understanding the factors behind their performance I hope to make a valuable contribution to AO design for ELTs. The following sections describe the various components of the experiment including overall optical design. Important aspects such as temporal control and internal aberration are also discussed. Finally the experimental results for each control scheme are given along with a discussion on the performance of each.

5.2 Optical Design

The first job in designing and building the WTAO demonstrator is in defining the core components of the system. These include the light source, phase screen, wavefront sensor

and two DMs. All optical design is then based on the properties of these choices.

A He-Ne laser light source is used instead of a white light source for a number of reasons. Although a white light source is a better approximation of broadband starlight it has a number of disadvantages. In the virtual WFS experiment[81] in our laboratory, a halogen light source suffered from low luminance and odd shaped point sources. By using a laser such problems are avoided. As the wavefront sensing and phase correction is largely achromatic the use of a a He-Ne laser source does not effect the validity of this experiment. Interference from the multiple reflecting surfaces did not manifest itself in the course of this experiment.

The choice of woofer and tweeter DMs is largely based on availability within the group. Before arriving at the final design, a system had been created to employ a membrane mirror, the OKO 37 micromachined deformable mirror (OKO37MMDM) as a woofer with a 48000 actuator MEMS mirror developed by the Fraunhofer Insitut[82] as the tweeter. The low stroke and poor wavefront fitting performance (chapter 3) of OKO37MMDM and unstable operation of the Fraunhofer tweeter made these two unsuitable for use in the WTAO demonstrator. A more suitable combination is found with the OKO37PZT and BMC140 DMs which had the necessary high/low stroke differences. The combination of OKO37PZT and BMC140 was mechanically awkward in that they required a 9x factor demagnification from the 27mm OKO37PZT to the 3mm BMC140 mirror surface. All optical design was based around imaging a 11mm beam from the phase screens onto both DMs with appropriate demagnification. A not-to-scale schematic of this design in shown in figure 5.1.

A helium-neon laser with fibre optic coupling provides a single point source acting as both guide star and science target. This is collimated onto an etched Kolmogorov phase screen located at the entrance pupil. The woofer is then located at the first conjugate point where a beamsplitter reflects light back at 90^0 to the tweeter. Another beampslitter splits light into the WFS and imaging camera. The system also has a non permanent fixture to allow WFS calibration. The WFS calibration arm is shown in figure 5.2 along with the main properties of each optical element.

The initial aperture chosen impacts on the number and influence of DM actuators for both woofer and tweeter. It also effects the strength of turbulence and the sampling

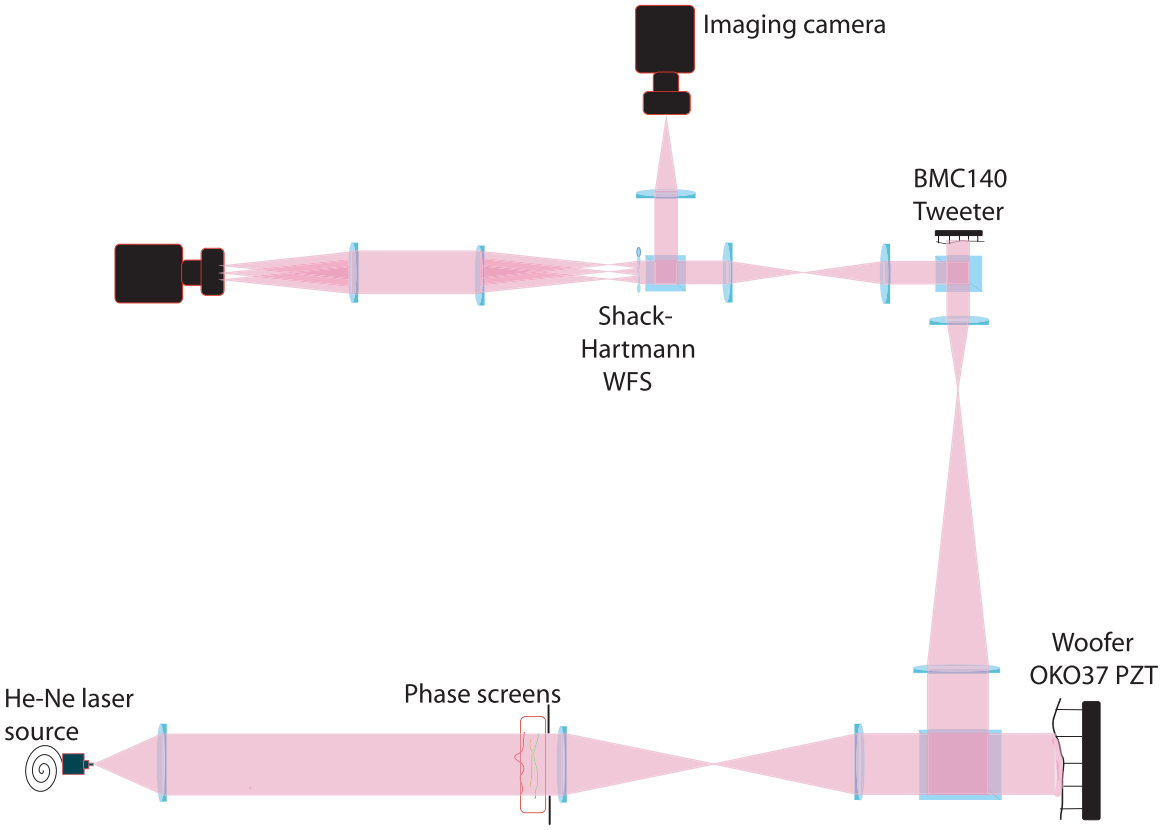

FIGURE 5.1: Schematic of the optical bench for the WTAO experiment with exaggerated scale. The pupil conjugates are located at the phase screen, woofer, tweeter and just behind the lenslet array.

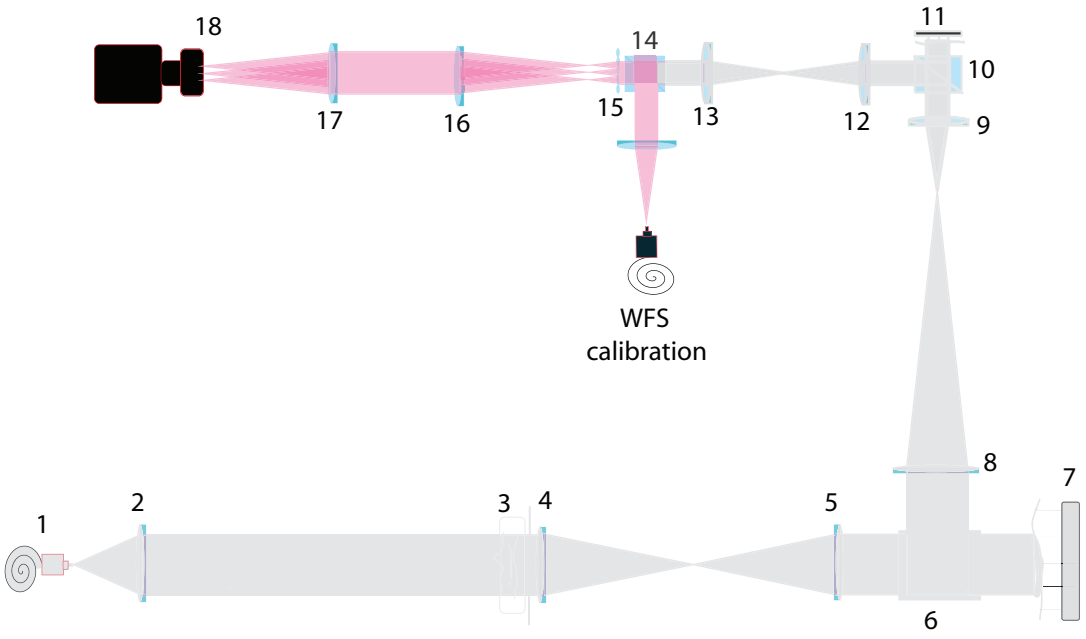

FIGURE 5.2: Optical path for WFS calibration

object	distance (mm)	diameter (mm)
1. HeNe laser fibre	40	0.01
2. Collimating lens, f=300	300	60
3.Stop and phase screen, $r_0 = 1mm$	140	12
4.f=140mm	440	11
5.f=300mm	100	26.4
6.30mm Beamsplitter	170	23.6
7.OKO37PZT Woofer	400	23.6
8. f=400mm	445	23.6
9. f=45mm	25	2.66
10. 20mm Beamsplitter	20	2.66
11. BMC140 Tweeter	60	2.66
12. f=60mm	120	2.66
13. f=60mm	40	2.66
14.20mm Beamsplitter	20	2.66
15. 12x12 square lenslet array	67	2.66
16. f=60mm	120	-
17. f=60mm	67	-
18. Retiga 2000R CCD	-	-

TABLE 5.1: Properties of main optical elements

of phase in the WFS. Using an 11mm diameter beam at the phase screen the geometric representation of actuator positions and SH subapertures is shown in figure 5.3.

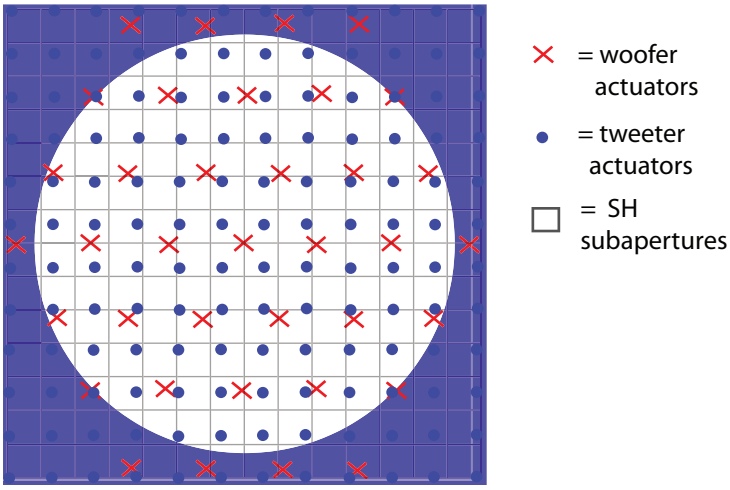

FIGURE 5.3: Actuator and subaperture geometry for the WTAO demonstrator. There is no major matching of components with the overlapping geometries dictated by the intrinsic properties of each mirror and lenslet array. Consideration is given to ensure optical beams are centred as much as possible on each component.

5.3 Wavefront Sensing

Wavefront sensing in this experiment is performed using a common Shack-Hartman WFS with a lenslet array at the pupil conjugate imaged onto a low noise CCD. The characterisation of this CCD and WFS operation is described in this section.

CCD Characterisation

A Charge Coupled Device (CCD) camera is used to image the spot positions for the SH WFS. In this experiment a Retiga 2000R manufactured by QImaging is used. The main properties of this CCD are

- Monochrome non-cooled
- 12 bit, 4096 gray levels
- 1.92 Megapixels, 1600x1200
- $7.5\mu m$ pixel size
- 40,000e- full well depth

The camera was experimentally characterised to measure its gain, readout noise, dark current and linearity. Such variables are usually included with the manufacturers literature but these are obtained through different tests and for different cameras. A measure of these properties is necessary to account for errors in wavefront sensing.

The gain of a CCD camera is the ratio of photon/electrons for unit output of Analog to Digital Units(ADU)[83]. As such it is the only measure of real light intensity when comparing ADU outputs between cameras. Knowledge of gain also allows other variables such as read noise and full well depth to be calculated. The gain for the Retiga 2000r was measured by calculating the variance of mean signal level[84]. Uniform illumination is an important feature of these experiments and a Bentham Instruments Integrating Sphere fulfilled this role. This light source has three levels of power and a variable aperture with the maximum of each being used here to minimise dark noise effects. The gain of a CCD is related to its shot noise (N_s) and mean signal level($\overline{S}$) as

$$G = \frac{\overline{S}}{N_s^2} \tag{5.1}$$

Readout speed	10MHz	20MHz
Read noise (e-)	15.03 ± 0.02	14.07 ± 0.30
Manufacturer's value (e-)	-	16

TABLE 5.2: Read noise for the Retiga 2000R. There is surprisingly less noise at 20Mhz operation possibly due to manufacturer opimisation.

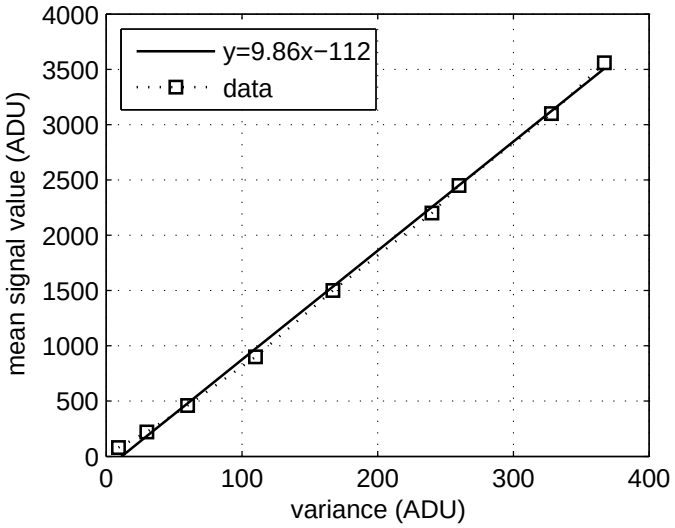

FIGURE 5.4: Plot of mean signal level versus signal variance with polynomial fit

Mean signal level was increased by varying exposure times. After flat field effects had been removed from the images the variance N_s^2 was calculated. By plotting signal against variance (figure 5.4) a least square fit was performed on the data. This yielded a gain value of $9.86 \pm 0.05 e/ADU$ which is valid for the linear region of the camera. Manufacturer's value was not given but full well depth was quoted as 40,000 electrons. Therefore for a 12bit camera with 4096 gray levels, the gain would be $9.77 e/ADU$.

Read noise is associated with measuring a time integrated signal from a pixel and it is usually the dominant noise source associated with CCDs. To measure read noise a number of bias and dark frames are recorded. These are images recorded with no light input and the lowest exposure time, $10\mu s$ for this model. Flat field effects are removed from each image and then all frames are averaged. The standard deviation of these images is then the read noise recorded in digital counts. Converting into electrons using the previous gain figure the following results were obtained.

Dark current in a CCD occurs when thermal electrons are released during exposure which add to those released through photon interaction. The effect is heat based and can be reduced through additional chip cooling. The dark current was measured

experimentally for the Retiga 2000r by making a series of long exposures of 60 seconds under zero illumination. A bias frame was subtracted from each of these 'dark' frames and the mean signal difference between dark and bias frames is calculated. This figure is then divided by sixty seconds and converted from ADU to $e-$ using the previous gain figure. The dark current on camera startup in a colder morning laboratory was found to be $0.278 \pm 0.033e- /pixels/s$ whilst in warmer conditions this rose to $0.524 \pm 0.108e- /pixel/s$. The manufacturer, Q-Imaging, declared the dark current to be $0.5e- /pixel/s$ with no temperature specified.

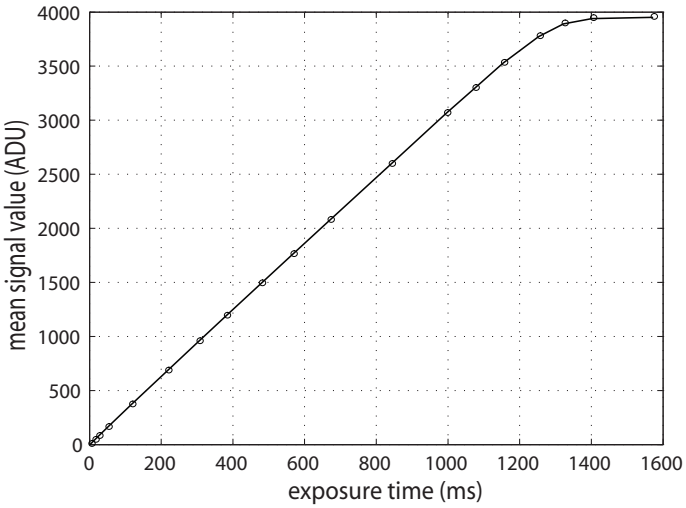

FIGURE 5.5: Plot of mean signal level versus exposure time for the Retiga 2000R. This CCD responds linearly to light intensity up to below about 90% saturation.

The linearity of a CCD is a measure of its electronic response to light intensity. The easiest way to measure this was to keep the camera at constant illumination, vary the exposure times and record the mean signal level. The Retiga 2000r had its exposure varied from $10ms$ to$1600ms$ where pixels are beginning to saturate. A plot of ADU output (figure 5.5) shows the camera to be largely linear up to about 3500 counts.

The dynamic range of a camera is the amount of discernible light levels it can record. In terms of decibel the dynamic range is (full well depth / read noise). From the 2000r's data sheet this is $68db$. Using the measured values the dynamic range is $69db$.

5.3.1 Shack-Hartmann Wavefront Sensor

An essential part of the AO system is the wavefront sensor and for this experiment a SH -WFS was thought to be the most appropriate choice. In section 2.4 I describe the theory behind this WFS. A lenslet array from Adaptive Optics Associates inc. is used in this experiment. This square lenslet array has a focal length for each lenslet of 6.7mm and a lenslet pitch of 0.2mm. For square apertures, spot width is $d_{spot} = 2\lambda f/d$. This corresponds to a spot width of 42.4μm or 3.3 pixels on the camera when used in the 2x2 binned mode.

It is important that the dynamic range of the WFS is matched to the incoming aberrations. Before AO convergence the SH spots will be at their peak angular excursions. If there is not enough dynamic range, spots might locate in neighbouring subapertures and AO correction convergence may not occur. Goncharov *et al*[85] gives the standard deviation of tilt angle for a beam propagated through atmospheric turbulence as

$$\sigma_\alpha = 0.427\frac{\lambda/d}{d/r_0^{5/6}} \tag{5.2}$$

The maximum tilt deviation is then $2.5\sigma_\alpha$ which is true 99.7% of the time. For this experiment $r_0 = 0.18$mm at the lenslet array. This corresponds to a 3.67x10^{-3}radian angular deviation. The minimum number of pixels required for a subaperture is

$$m = n(1 + 5\sigma_\alpha d/\lambda) \tag{5.3}$$

where n is the number of pixels sampling the spot and d is subaperture size. For the parameters of this experiment 10.91 or 11 pixels are required for each subaperture. As the focal plane of the lenslet array is too short to image directly onto the CCD an optical relay is needed. A straight 4f optical relay is used which has resulted in pixel quantisation of each focal spot. Each subaperture is sampled by 15.5 pixels which is above the required 11 pixels. Figure 5.6 shows one such spot with no aberration and with phase screen aberration. The spot loses its square aperture diffraction pattern which indicates a small amount of higher order aberration other than tilt present. This is due to the slight undersampling of the wavefront. The D/r_0 ratio requires 15 subapertures to be sampled but only 13-14 subapertures are used in the experiment. In practice AO performance was not effected and this may be due to a slight overstating of phase screen

strengths. Figure 5.7 shows the SH spot positions and geometry for both clean and aberrated wavefronts.

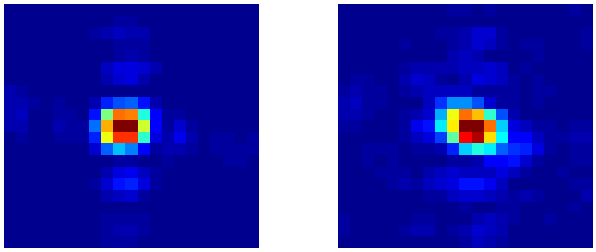

FIGURE 5.6: Typical Shack-Hartmann spot imaged with full CCD resolution and not in the binned mode used in experiments. The image on the right has been aberrated by a turbulent phase screen.

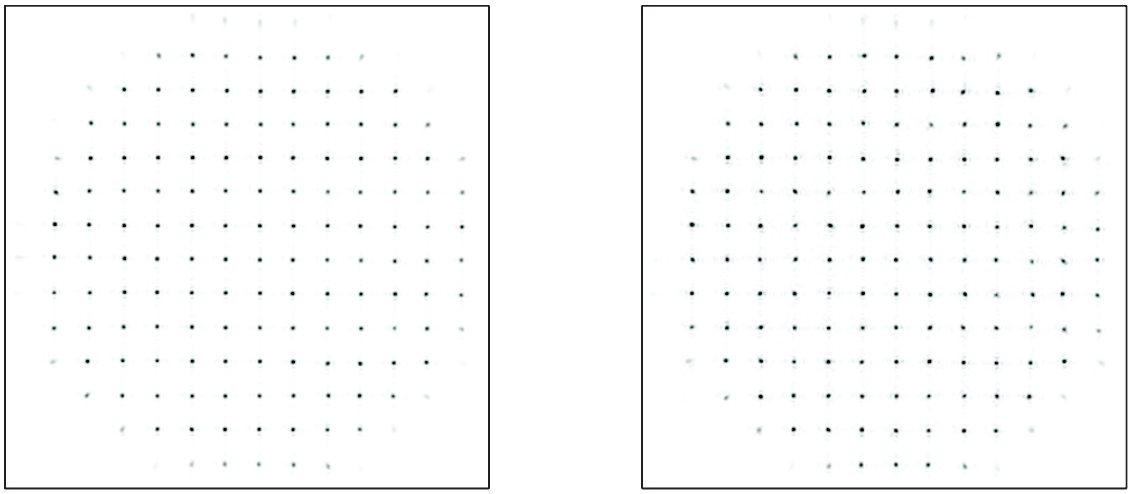

FIGURE 5.7: Recorded SH spots for WTAO experiment with and without turbulent phase screens where subtle spot deviations of between 1-4 pixels occur.

The wavefront is calculated continuously for each iteration of the AO loop. Figure 5.8 shows the procedure for wavefront sensing.

1. **Define grid centre:** User manually selects the centre pixel from a live image. A grid 15x15 subaperatures is then defined around this central point with each subaperture being 15 pixels wide. Across the full aperture individual spots are not centred within their boxes.

2. **Perform grid thresholding:** The square grid contains boxes which have no spots or outlying spots with low intensity and irregular shape. By integrating the

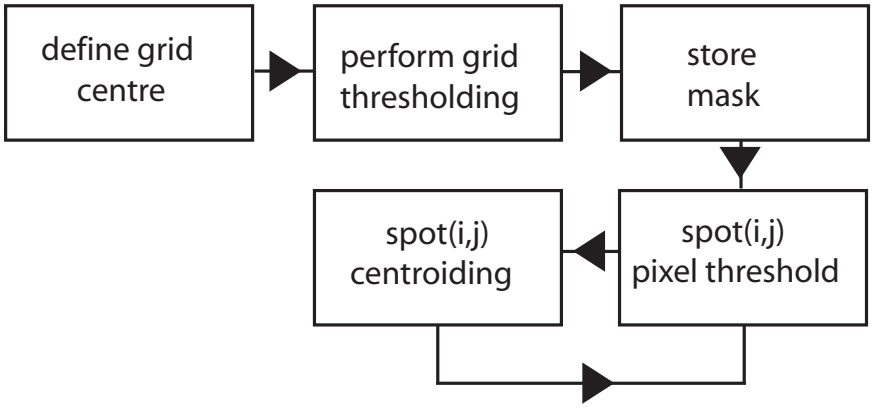

FIGURE 5.8: Wavefront sensing workflow with each routine performed by computer calculation.

light in each box a measure of an acceptable spot can be obtained. A threshold is then set to flag these redundant subapertures.

3. **Store mask:** A mask is made up from the positions of null subapertures (figure 5.9).This mask is applied to all WFSing operations from performing interaction matrix calculations and closed loop AO. This ensures wavefront uniformity between operations.

4. **Pixel thresholding:** For each spot position a threshold value is set on pixel intensity. Pixels which fall below this value are zeroed. This ensures any non-uniform illumination across the aperture is not included in centroiding results and also mitigates some effects of the effects of CCD noise.

5. **Centroiding :** For each subaperture the local wavefront gradients can be calculated by a number of methods. The simplest method is to perform and centre of mass calculation. For either x or y slopes the gradient value, S_x or S_y, in pixels for any subaperture is

$$S_x = \frac{\sum_{x=1}^{N}\sum_{y=1}^{N} I_{x,y}x}{\sum_{x=1}^{N}\sum_{y=1}^{N} I_{x,y}} \tag{5.4}$$

Here x and y are the pixel locations and I is the intensity measured in ADUs.

Full wavefront reconstruction is an unnecessary intermediary step in the AO loop with X and Y gradients being sufficient measures of phase. Wavefront reconstruction

calculates the phase relationship between subapertures and is useful for visual representations of wavefronts. The recursive techniques of Hudgin[86] are used to calculate wavefronts from slope information. The sensor in this case outputs estimates of wavefront slope or phase differences on a square array. The points of phase difference S are defined by the phase ϕ at subaperture points as

$$S^1_{j,k} = \phi_{j,k} - \phi_{j+1,k}, \tag{5.5}$$

$$S^2_{j,k} = \phi_{j,k} - \phi_{j,k+1} \tag{5.6}$$

where $j, k = 1, ..., N$. Hudgin states the recursive form of this wavefront reconstructor as

$$\phi_{j,k} = \frac{1}{4}(\phi_{j,k} - \phi_{j,k+1} + \phi_{j,k} - \phi_{j,k+1}) + \frac{1}{4}(S^1_{j,k} - S^1_{j-1,k} + S^2_{j,k} - S^2_{j,k-1}). \tag{5.7}$$

By setting the boundary nodes of phase as zero a full phase map can be recursively reconstructed from gradient measurements. An example of one such reconstruction is shown in figure 5.10

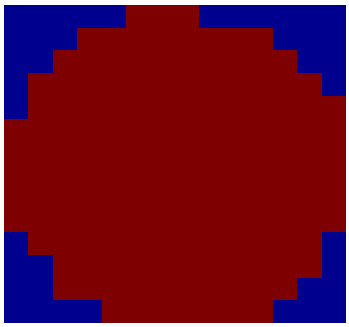

FIGURE 5.9: Wavefront sensing mask to exclude redundant subapertures

5.3.2 Turbulence

Atmospheric turbulence as experienced in astronomical observations needs to be simulated effectively in any scaled laboratory experiment. Any aberrations caused by air flow in the laboratory will be negligible. A substitute is required that matches the Kolmogorov power spectrum and which can be made with varying intensities. A hot air turbulence generator has been demonstrated for use in a WTAO experiment[87]

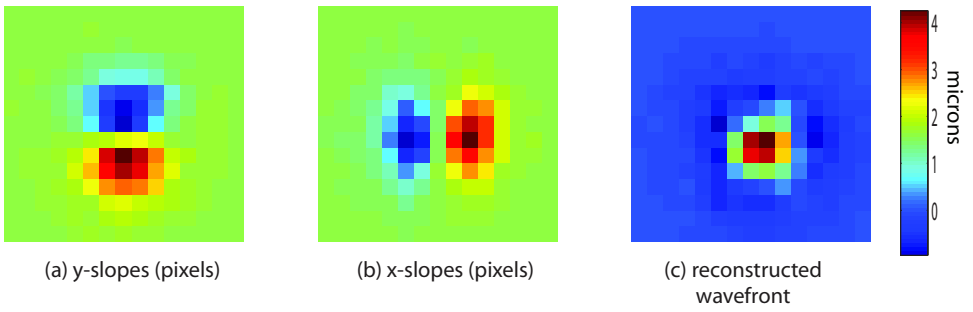

FIGURE 5.10: The first to images are of X and Y slopes recorded in colour-scale with units of pixel length for a single actuator poke of the OKO37PZT. Using Hudgin's recursive reconstructor the image on the right is of the reconstructed wavefront with scale in microns.

which satisfies both these requirements. It is however fully dynamic, non-repeatable and overly complex for the purposes of this experiment. A simpler approach is to manufacture phase screens with the appropriate statistical aberration either through ion exchange[88] or etching[89]. In this experiment etched phase screens are used.

The surface etched phase screens used here are produced by Silios Technologies and feature on the European Southern Observatory's (ESO) Multi-conjugate Adaptive Optics System[90]. An atmospheric phase pattern is etched onto a silicon and glass substrate with a 1.5mm thickness. The benefits of using etching methods are a high transmission ($> 90\%$) and higher spatial resolution with pixels being 0.1mm in size. A single plate placed at the optical pupil is used to provide aberrations for the WTAO. This plate (PS2) has been characterised by a previous group[65]. The template phase map is shown in figure 5.11 overlayed with the pupil. Although the physical plates are different the template phase screen used to print the plates are the same. The intended strength of this screen is $r_0 = 0.81 \pm 0.03$mm at 632.8nm. Using a method of point spread function inspection to characterise the r_0 value of the screen an experimental value of 0.73 ± 0.06mm was found. A masters student within the Applied Optics group, Richard Legg, attempted to validate this figure by way of interferometric analysis but the screens proved too strong to yield meaningful results. His results for two weaker screens showed the quoted r_0 values to be a close match to the intended values.

The final strength of turbulence is then defined by the aperture diameter through PS2. An 11mm aperture will provide strong turbulence between $D/r_0 = 13 - 15$ given the disparity in r_0. This might not be an appropriate strength to overload the tweeter,

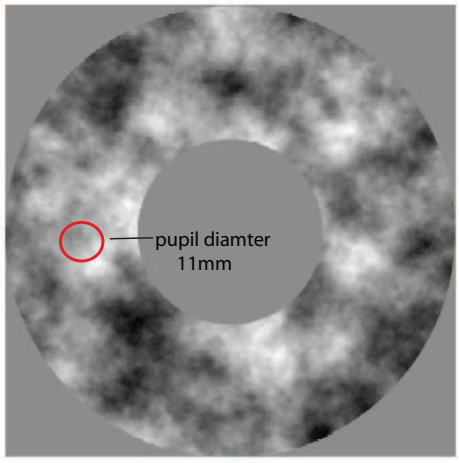

FIGURE 5.11: Phase screen PS2 with scaled pupil. This phase map is the simulated template used to produce the screen.

but will cause it to clip when combined with the internal aberration. The benefits of WTAO operation should then be apparent.

5.4 Adaptive Optics Correction

Closed loop AO requires a well aligned and calibrated WFS to be successful. Measuring an accurate interaction matrix for both mirrors is an essential part of this. The WFS response to each actuator poke is given in figure 5.12. Each horizontal column expresses the pixel shift in x(column 1-225) and y(column 226-450) directions. The woofer actuator pokes show influence over a far wider area than the correpsonding tweeter pokes which only cause deformations around a few neighbouring SH supapertures. Examining the

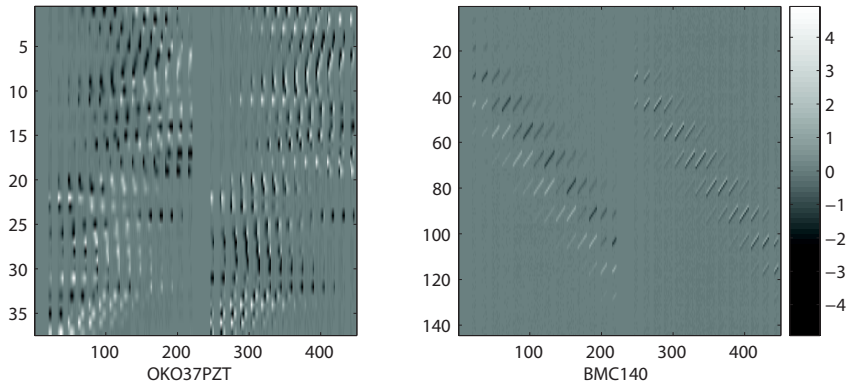

FIGURE 5.12: Interaction matrices for the woofer and tweeter DMs. Each column relates the WFS response to unitary actuator pokes as recorded in pixels.

wavefront maps for four of these influence functions for each mirror (figures 5.13, 5.14) shows the WFS and DMs to be performing as expected.

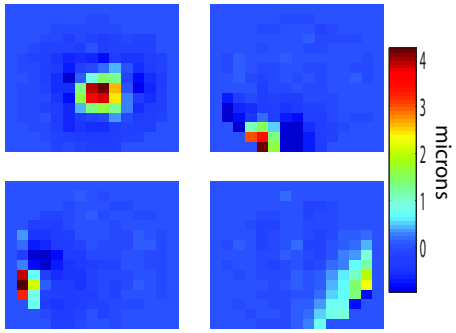

FIGURE 5.13: Reconstructed phase maps for the first four woofer influence functions scaled with scaling in microns. These are the result of positive and negative actuator pokes and the 4 actuators chosen are located at different locations in the aperture with the fourth actuator located outside the aperture resulting in a relatively poor influence function.

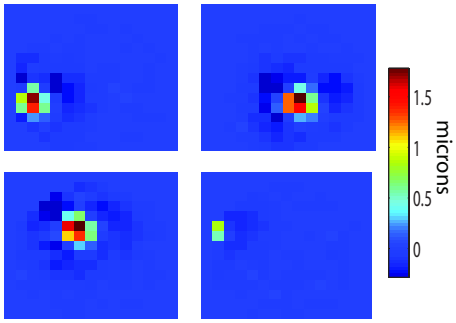

FIGURE 5.14: Four randomly chosen influence functions for the tweeter DM with scaling in microns. Note the smaller PV range of deformation and narrower profile in comparison to the woofer pokes.

As before in simulations, SVD is used to aid inversion and modal filtering for these interaction matrices. The experimental singular values for both woofer and tweeter are shown in figure 5.15.

Figure 5.16 shows the singular values for the large zonal interaction matrix and the deprojected tweeter interaction matrix.

5.4.1 Temporal Control

The temporal control of actuator commands is calculated separately to spatial control . The WTAO demonstrator operates with static Kolmogorov phase screens as the focus of this thesis is on spatial control. Hampton *et al.*[91] have given an overview of the temporal aspects of WTAO. Temporal control filtering is unnecessary if the system is

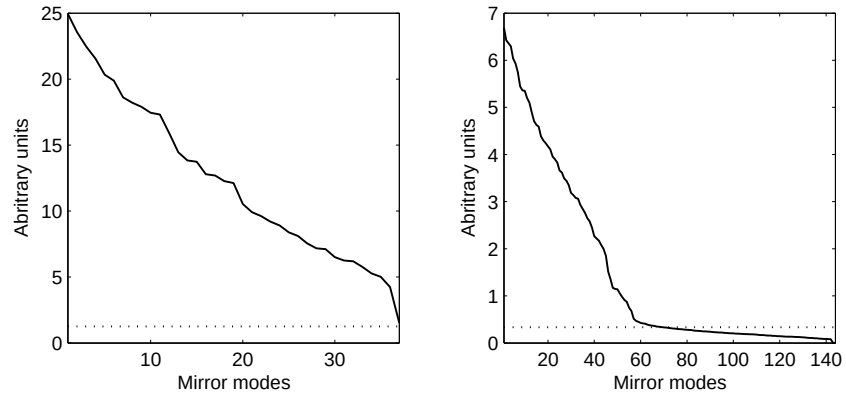

FIGURE 5.15: Singular values for separate woofer (left) and tweeter (right). With a condition factor of 1/20th the first singular value this results in 36 modes for the woofer and 60 for the tweeter.

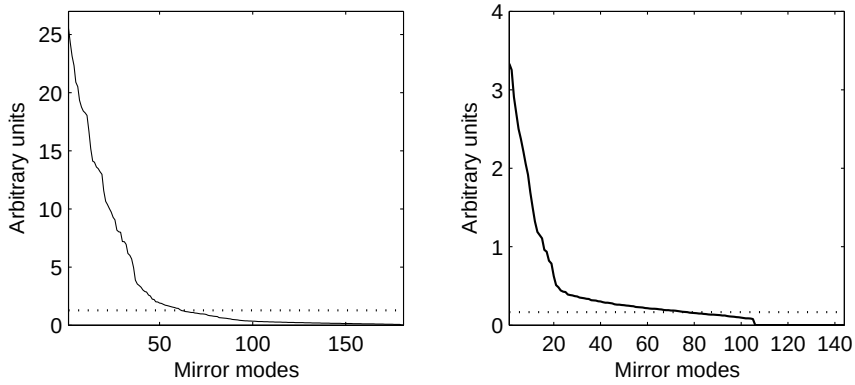

FIGURE 5.16: (left)singular values for dual zonal WTAO (right)singular values for tweeter with deprojected woofer modes.

to operate in open loop. However, due to DM hysteresis, non-linearity and other small effects closed loop AO allows the system to converge to a better solution than open loop correction. For that reason a static system still requires temporal filtering of closed loop control signals.

After calculation of command signals through spatial fitting it is necessary for these signals to be filtered to avoid oscillations or non-optimum correction. A simple integrator[92] is used in this regard with command signals at time n given as

$$x_n = (1 - \beta)x_{n-1} + gMs_n \tag{5.8}$$

with both $\beta, g \ll 1$. The bleed parameter β is used to negate the effect of invisible modes. System gain, g defines the speed of convergence and stability of the loop. Both these parameters are optimised for each spatial control regime through trial and error.

The control matrix M and slope estimates s_m being used to calculate the initial control signals before filtering. A summary of the optimal experimental values is shown below.

	Gain, g	Bleed, β
Dual separate, woofer	0.6	0
Dual separate, tweeter	0.25	0.25
Zonal WTAO, woofer	0.6	0.05
Zonal WTAO, tweeter	0.3	0
Modal deproject, woofer	0.6	0
Modal deproject, tweeter	0.1	0.15

TABLE 5.3: Gain and bleed parameters used for each control scheme. These parameters were found through experimentation.

The AO loop runs at a speed of approximately 5Hz, far below the requirements for realistic dynamic turbulence.

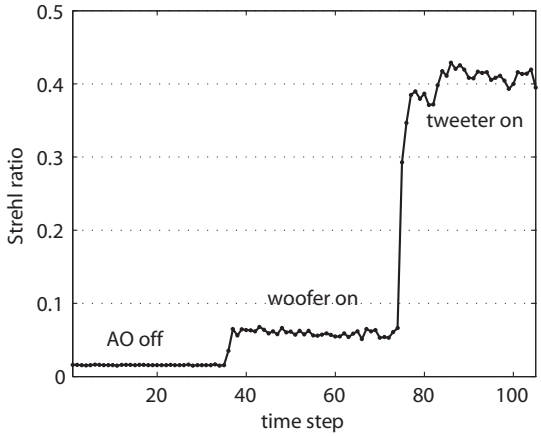

FIGURE 5.17: Strehl ratio versus time when using AO off, woofer switched on and then tweeter. The zonal method here means the woofer corrects very poorly on its own as the control modes are a combination of woofer and tweeter actuators.

5.4.2 Internal aberration correction

The light that passes through the WTAO system does not arrive at the WFS as a perfect plane wave. Each optical element it passes through or reflects off adds its own aberration from slight misalignments of the beam and manufacturing tolerances. The two DMs also have their own bias position aberration which is quite severe in the case of the OKO37PZT. To minimise these aberrations it is necessary for the WFS to be calibrated by a separate plane wave source. The null positions as measured by the WFS

from this light source will act as a reference; closing the AO loop successfully will result in wavefronts returning to plane wave form.

A collimated laser beam is positioned to enter the third beamsplitter to illuminate the WFS (figure 5.2). Care is taken to ensure that this beam passes through the same path as that of the guide star. Any additional aberration from the final four optical elements will not be included in this reference. These non-common path aberrations can also be corrected by using phase diversity techniques in which some image has a known aberration applied to it and phase retrieval is achieved by measuring the known aberrated PSF and the original aberrated PSF [93].

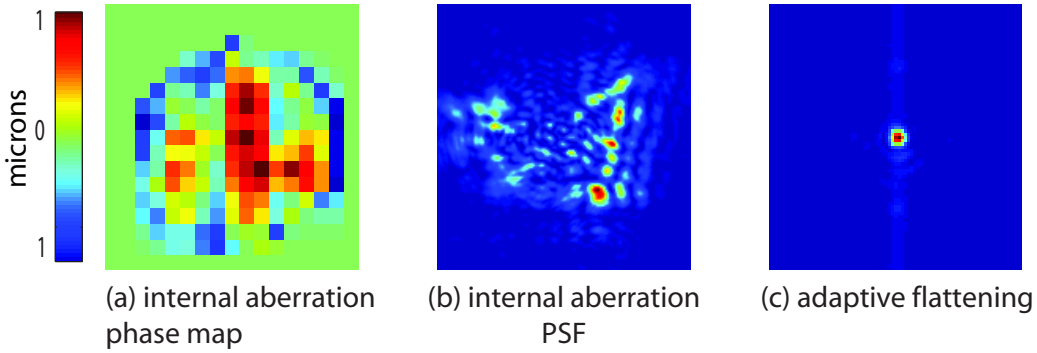

FIGURE 5.18: Phase map and PSF for the initial internal aberration. The woofer uses quite a bit of its dynamic range to correct for this aberration.

5.4.3 Closed loop WTAO

The three control schemes mentioned in section 4.3 are experimentally evaluated to confirm the simulation results. The performance parameters of interest are final image Strehl ratio and PV mirror shapes. Appendix 2 describes the software and hardware environment used to control each piece of hardware and perform calculations.

The method of de-projecting the woofer modes from the tweeter influence functions was the most successful when simulated in section 4.4. Results from the University of Victoria[61] indicate that a similar method would require 9 times less stroke than a zonal method. Using the matrix operations of section 4.33 the woofer modes are removed from the tweeter influence functions. Figure 5.19 shows woofer influence functions projected onto tweeter influence functions ($P_{TW} = W^{-1}T$). Each column represents the woofer commands to fit a tweeter influence function. A projection of woofer IFs onto tweeter IFs with woofer modes removed is shown on the right. The near zero scaling shows these

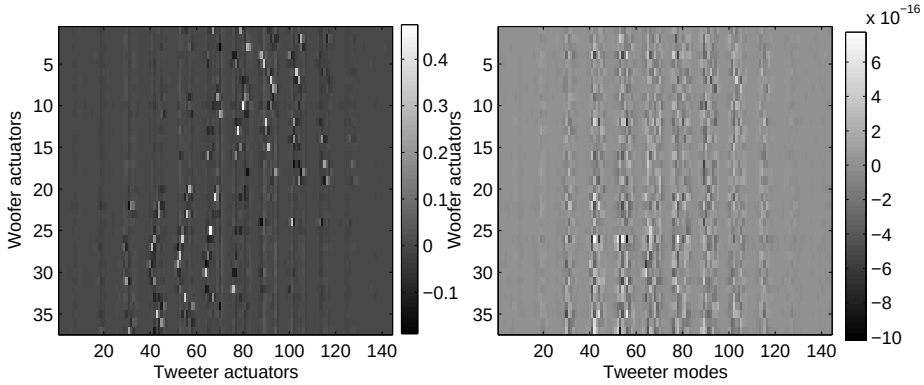

FIGURE 5.19: (left)Woofer influence functions projected onto tweeter influence functions. (right) woofer influence functions projected onto tweeter modes with de-projected woofer influence functions. The near zero values show the woofer modes to be fully removed from tweeter.

modes to be effectively removed, with no combination of woofer shape able to recreate a tweeter mirror mode. These tweeter modes are now fully orthogonal to woofer shapes when used in the WTAO experiment.

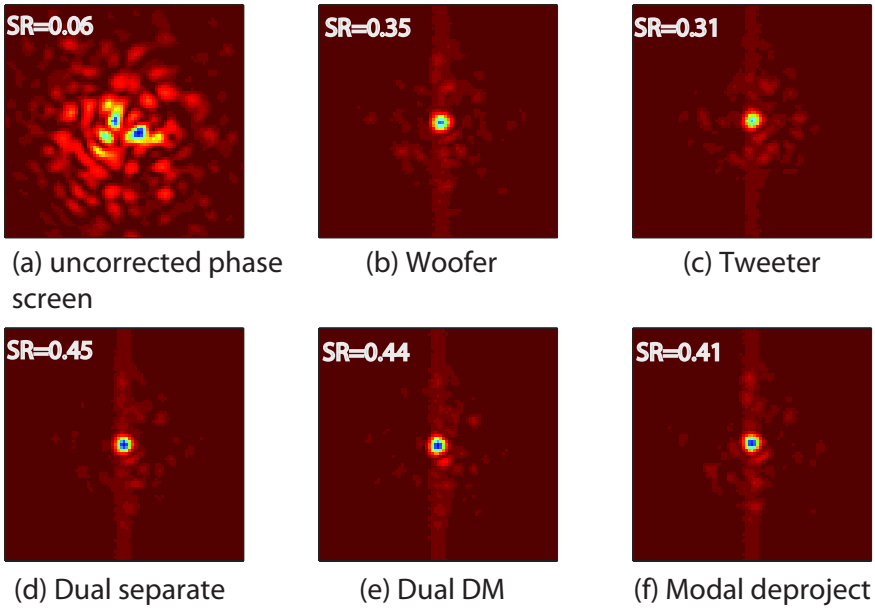

FIGURE 5.20: Recorded PSFs after closed loop AO

The results for correcting a static section of turbulent phase screen are seen in figure 5.20. The phase screen is added after pre-correction of static aberrations and the resulting PSF is characteristic of Kolmogorov turbulence. Individual woofer and tweeter correction is successful in recovering a lot of resolution with SR above 0.3. Using the three WT control schemes results in less speckle around the halo of the Airy disc and more energy concentrated in the peak. Calculating the SR for each control scheme over

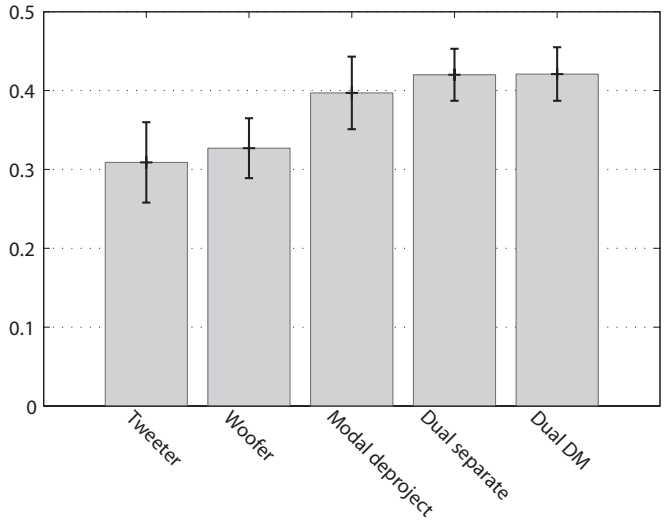

FIGURE 5.21: Average Strehl ratio for each control scheme. The three WTAO control methods performed quite similarly

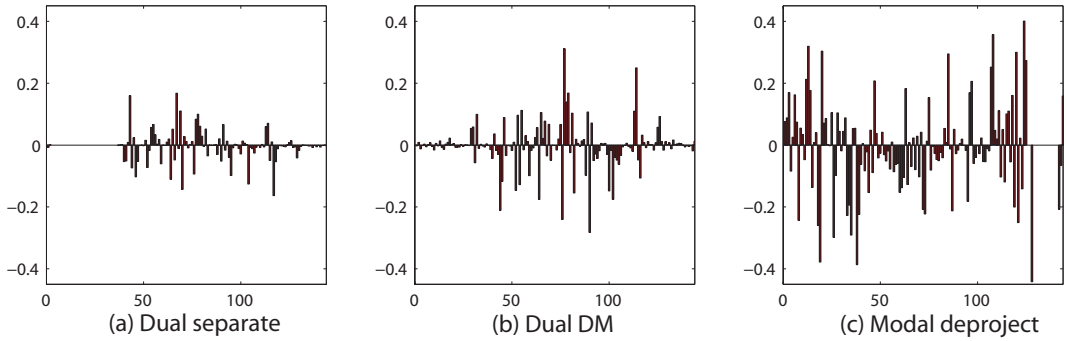

FIGURE 5.22: Typical control signals for tweeter DM for each control scheme. As in simulations the deprojected tweeter has much more variance in control signals

an average of 15 sections of turbulence shows a similar trend (5.21), with SR around 0.4 for all methods. The modal deproject method fails to outperform the zonal WTAO method as predicted in simulations.

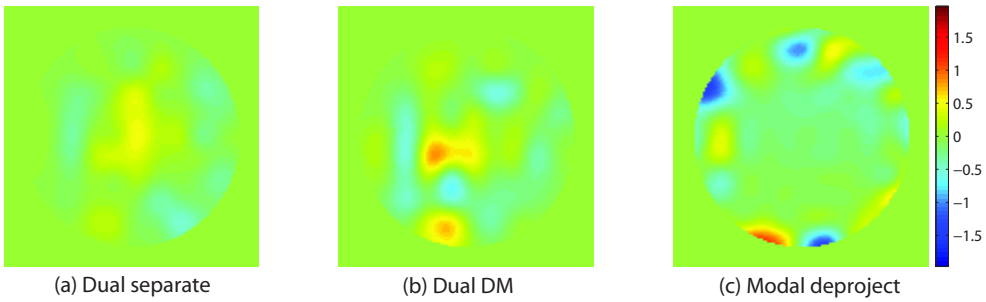

FIGURE 5.23: Wavefront shapes reconstructed from the measured interactions matrices and control signals in figure 5.22. The modal deproject method has the highest PV wavefront with most variance occurring at the edges of the aperture.

The shapes adopted by the tweeter for each scheme are illustrative of how that particular scheme shares correction between mirrors. Figure 5.22 shows the control signals for each tweeter at the point of stable correction. In phase space the corresponding tweeter shapes are given in figure 5.23. As expected tasking the tweeter to correct after woofer correction results in the smallest wavefront deformation, with the tweeter only performing a cleanup of residual wavefront error. In the Dual DM mode there is greater PV deformation and control signal variation but the tweeter still remains well within its dynamic range. Operating the tweeter in modal deproject mode results in much more control signal variation. The tweeter adopts a more severe shape with strong local gradients around the edge and flat elsewhere. This would indicate possible saturation of certain high order modes.

5.5 Conclusions

In this chapter I have described the design, operation and performance of the WTAO experiment. The experiment successfully operated closed loop AO with SR above 0.4 achieved in all WTAO modes. This approximately matches the performance of simulated WTAO wavefront fitting with WT increasing correction performance by about 30% over single mirror operation. Using their 'confinement correction algorithm' Hu *et al*[77] predicted a 32% increased in SR using their own configuration of DMs. There are currently no other experimental results available in the public domain to compare with those presented here.

The experimental anomalies of the modal de-project method are in need of explanation. Having orthogonal woofer and tweeter mirror modes should lead to the most efficient and stable correction. In operation this method was prone to oscillations and instabilities in correction. This could be due to the outer actuators saturating for certain modes. The SH mask used might have been too generous with outer edge pixels, leading to poor wavefront sensing at the edges where the tweeter would have required much greater sensitivity. Reducing the de-projected tweeter modes to solve this results in a lower spatial correction and a larger fitting error. Overall the experiment did not make full use of tweeter actuators and should have used a slightly larger aperture. Due to the optical design this could not be readily changed. To overcome these outstanding issues a redesign of the experiment would be necessary.

Chapter 6

Summary and Conclusions

The conclusions from this research into a new dual mirror adaptive optics technique for astronomy are presented here along with some discussion on possible further work that may interest other researchers.

The necessity for dual mirror AO is shown in chapters 2 and 4 with deformable mirror stroke requirements providing a technological barrier to extremely large telescope operation. The properties of various types of DM design are discussed in chapter 3 with a comparative analysis of wavefront fitting shown. When tasked with correcting for strong turbulence the best mirrors are those which have the required actuator stroke and ability to fit the shapes demanded by Kolmogorov turbulence. In this regard the diameter and shape of a mirrors influence function is very important as well as the geometry of actuator grid. Whilst MEMS mirrors can provide the best possible fitting through brute force of actuator count a DM with optimised (for turbulence) actuators and layout is a more efficient solution and should be considered for implementation on ELTs.

A dual mirror, dual conjugate approach to ELT design has been acknowledged within the community for a number of years with only a small amount of research endeavored. The algorithms to operate such a design, some previously suggested and also of my own suggestion, are included in this research with the intention of comparing and contrasting correction performance. In simulations the modal-de-project method outperforms all others and seems an obvious choice due to its fully orthogonal nature. As seen in chapter 5, simulation and experimental experiences often show differences in performance for

a number of subtle and unforeseen operational reasons. For the experiment a 30% improvement in Strehl ratio is recorded as expected through both methods with PV deformations of mirrors showing quite different results between the control schemes. If much stronger turbulence with D/r_0 ratios above 40 are to be encountered then economy of stroke is very important. In this regard the modal de-project method could be expected to saturate and show far worse correction over the zonal WTAO method. A major mitigating factor which may have distorted this result from simulated performance includes the lack of sensitivity of the system to the very high frequency de-projected modes.

This research, as a proof of concept work, shows that WTAO works in a laboratory environment at mid level turbulence strengths typically encountered during good seeing on an eight metre telescopes. The best controlling algorithm is inconclusive at this strength of turbulence and more research is needed to provide a more definitive answer for the forthcoming ELTs.

6.1 Further Work

First light for ELTs is scheduled within the next decade with time for refining of theory and operation of WTAO. The major disadvantage of this research is its application to very large telescopes (8-10 metre class) and not to larger aperture extremely large telescopes (>30 metres diameter). Simulations and experiment were both limited by computing power and available DMs. It would be necessary to compute correction performance for a selection of WTAO mirror combinations with actuator counts greater than $3000-4000$ reflecting the requirements of ELTs. A more comprehensive simulation should also take account of the outer scale, particularly values of outer scale expected at the mountain top sites for each of the main ELTs.

The control algorithms used in this thesis are relatively basic in their nature in need of optimisation based on the DMs used as woofer and tweeter. Some form of live balancing or tuning of control between mirrors could also allow better sharing of correction depending on atmospheric conditions.

The temporal aspects of WTAO operation have largely been ignored within this project. This is a luxury only afforded within a laboratory or simulated environment

and will certainly have to be addressed for star light operation. Some research has already been done within this area[94] with fully dynamic experiments required.

A number of improvements could be made with the laboratory demonstrator to give more conclusive results. Having definable strength of phase disturbance would allow a better comparison between the control schemes to be performed. A wavefront sensor with double to triple the number of subapertures across would also allow greater study of the sensitive modal de-project method. Ultimately a laboratory demonstrator would need to have a tweeter MEMS DM with over 1000 actuators to properly compute expected performance on ELTs.

Appendix A

Computer control

An adaptive optics system requires quite an amount of computer control and calibration of the various deformable mirrors and wavefront sensors. The successful interfacing between mirrors, cameras and computer can be easily as challenging as optical alignment of the system. For the WTAO demonstrator all control and interfacing was implemented within a single, modestly powered pc. National Instruments Labview was the key component that made this possible, allowing hardware drivers and software code to coexist in a single application. The code used in this experiment was a mix of labview User Interfaces, Matlab code and some C++. An example of typical Labview and Matlab code can be seen in figure A.1. Generated GUIs screen grabs are seen in figures A.2 and A.3. The benefits of using Labview for small AO experiments are

- A library of routines and drivers available related to adaptive optics and associated hardware.
- Allows importing of Matlab and C++ routines. In the case of this experiment many of the Matlab routines had been tested and used for simulation work.
- Graphical User Interface based operation is more intuitive to allow other researchers with less experience operate the system.

There are some drawbacks to using this application for AO experiments which potential users should be aware of. If full dynamic operation is required at a few hundred Hz then Labview will probably prove too slow. Optimisation and embedded loops of faster

code are possible but high speed operation might still prove difficult. Labview can have quite a steep learning curve and it can be difficult to debug something as complex as an AO system. It helps to have a few Labview users or experts within your research group.

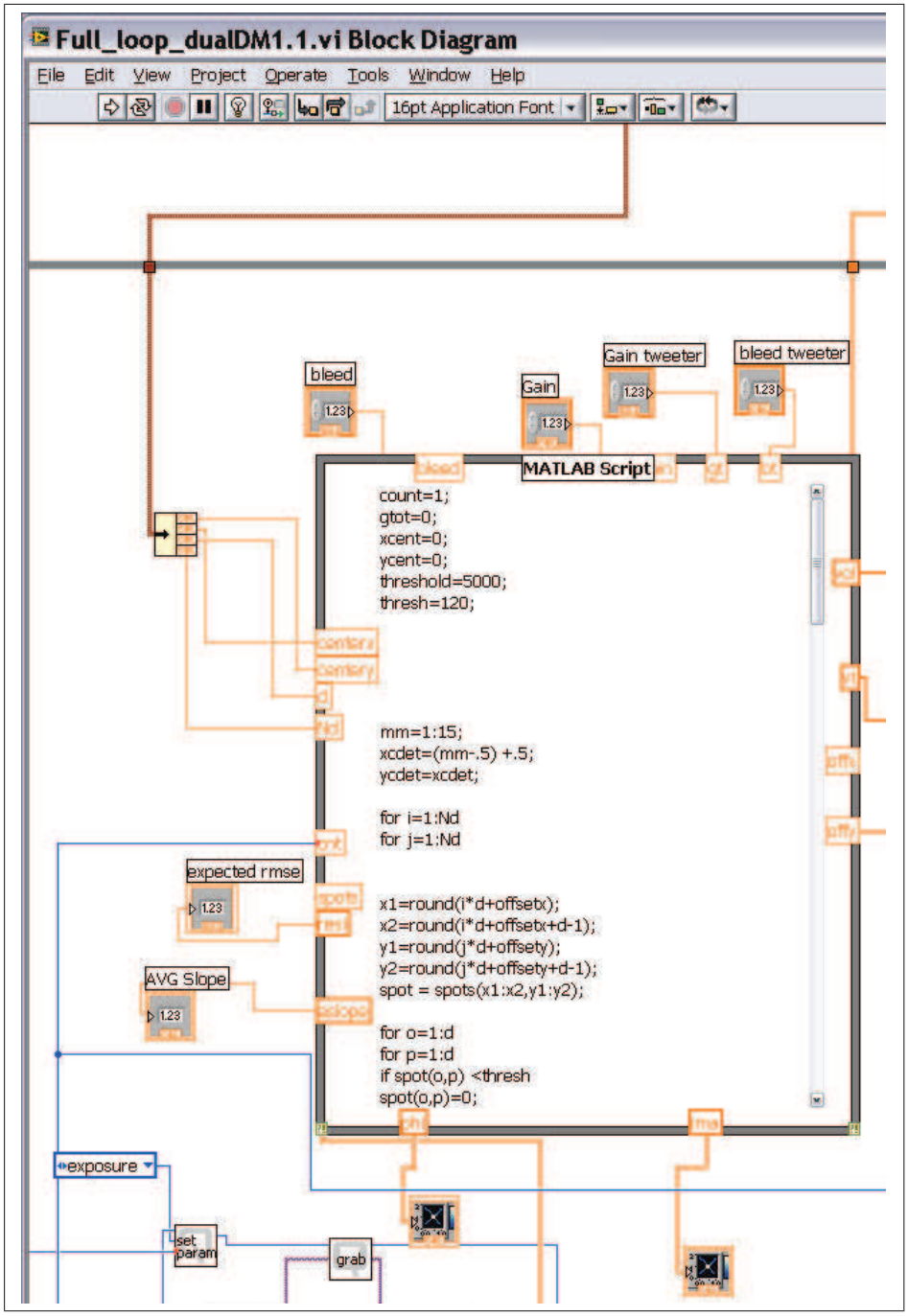

FIGURE A.1: Labview internal code interface with integrated Matlab code

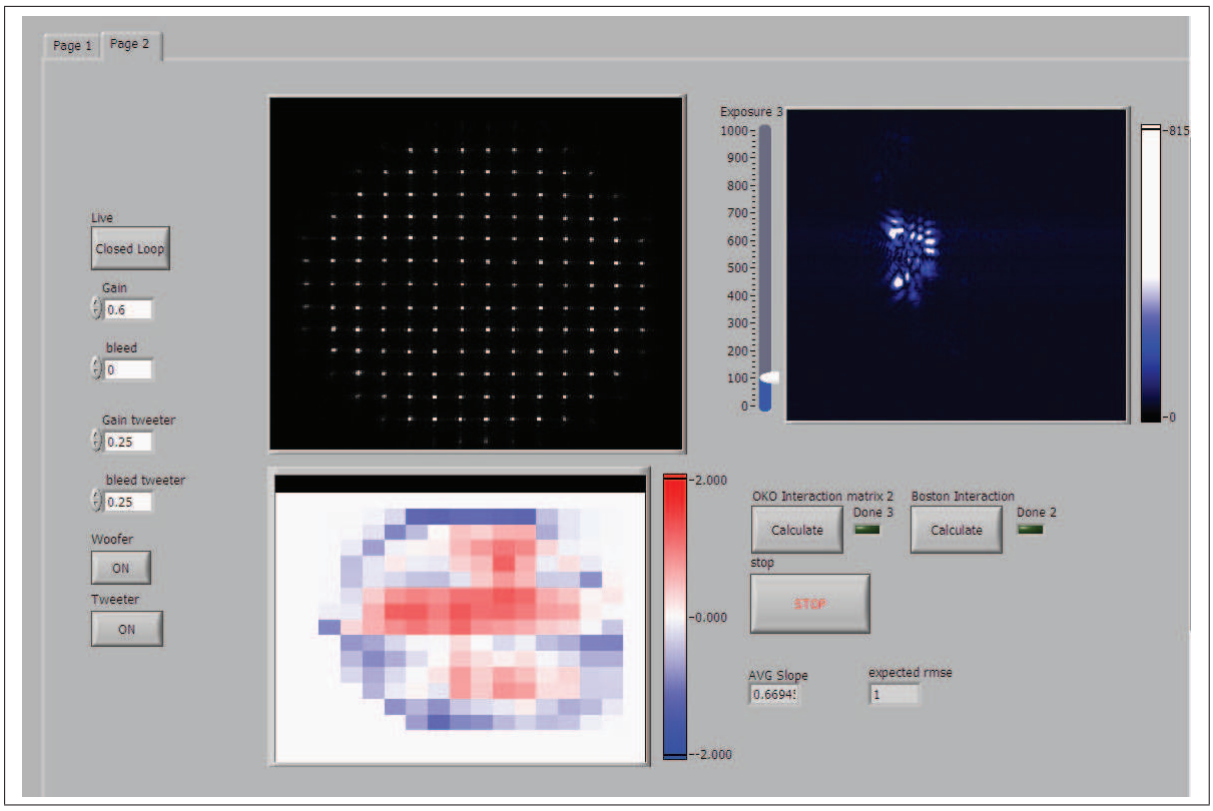

FIGURE A.2: Closed loop WTAO demonstrator GUI showing SH spot patter, reconstructed aberration and image before internal aberration correction.

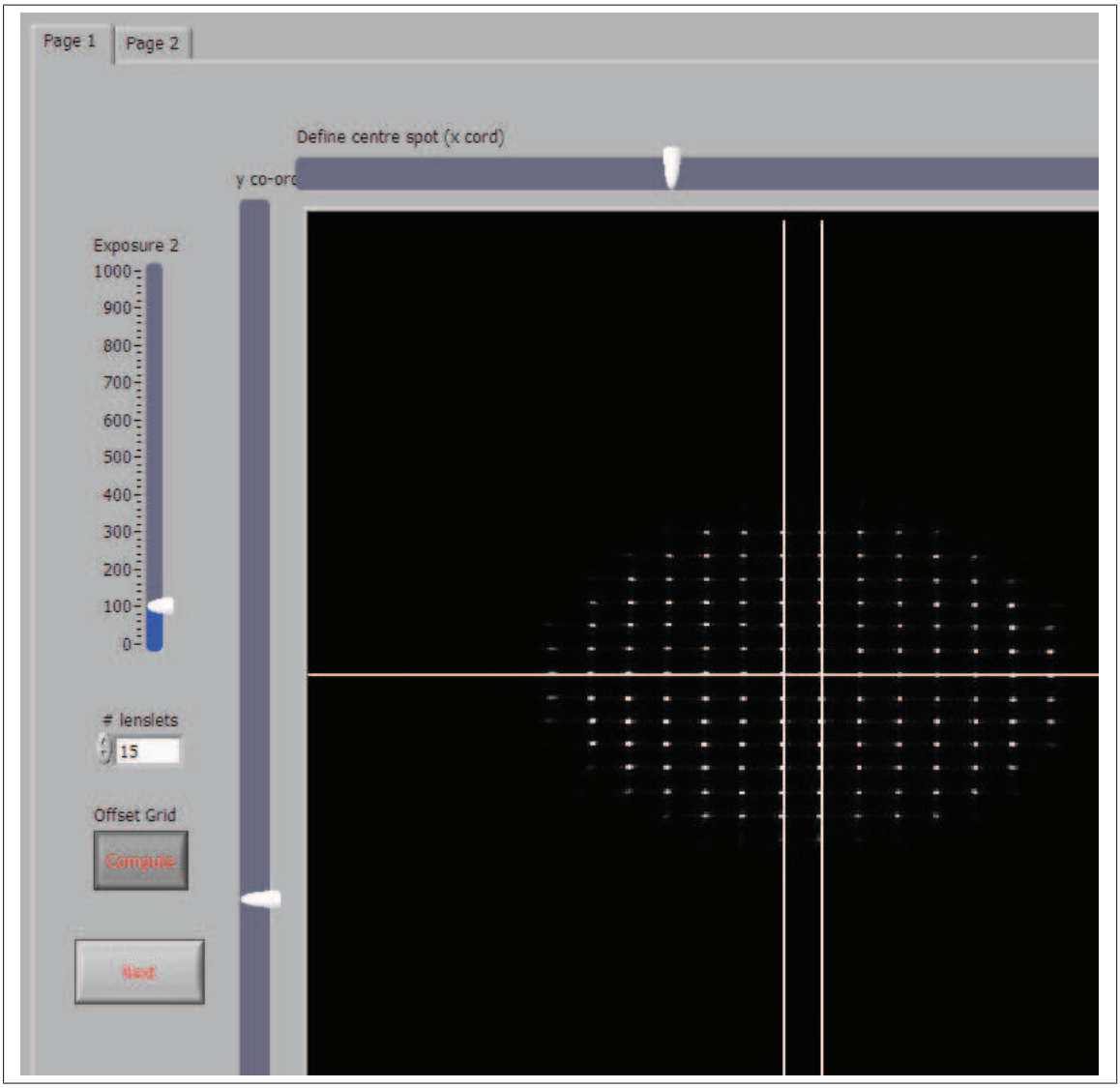

FIGURE A.3: Wavefront sensor calibration screen for the WTAO demonstrator

Appendix B

Strehl Ratio

The Strehl ratio is common image quality metric used mostly in astronomy. A detector at the focal plane will image a point source of light from a telescope as an Airy disc assuming zero aberrations. When aberrations are present this Airy disc is distorted and peak intensity is reduced. The ratio of aberrated peak intensity to un-aberrated peak intensity is the Strehl ratio. When turbulence is too strong and the Airy disc structure reduces the value of Strehl ratio as a quality metric reduces. Diffraction limited performance is obtained at 0.8 Strehl ratio. A common approximation to the Strehl ratio is

$$S = \exp(-\phi^2) \tag{B.1}$$

which is valid for wavefront errors ϕ^2 below 2 radians.

When dealing with a measured PSF, the SR is not easily obtained as finding peak intensity. The peak intensity for a perfect Airy pattern has to calculated as defined for that particular lens, camera and pupil size. For the WTAO experiment the these were focal length $f = 120mm$, pixel size $d_{ccd} = 6.45\mu m$ and beam diameter $d = 3mm$. The angular distance between two minima or maxima on an Airy pattern is $2.44\frac{\lambda}{d}$ with $\lambda = 633nm$. Due to the small angles involved this can be stated in terms of distance at the image plane,

$$h = 2.44\frac{\lambda f}{d} \tag{B.2}$$

Across the CCD this $61.8\mu m$ was recorded by 9.58 pixels. The quantisation of PSF by the camera leads to errors in Strehl ratio calculation.

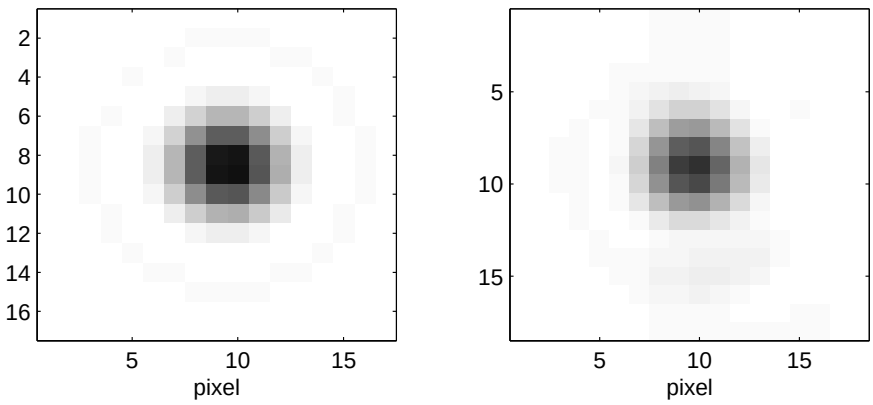

FIGURE B.1: PSF for simulated perfect airy disc and adaptive flattened PSF as measured by CCD camera

An Airy disc was simulated in Matlab and interpolated onto a grid to match the size of the CCD pixels. In figure B.1 this quantised Airy disc can be compared to the fully flattened experimental PSF. To get a final measure of peak intensity the total light over a small area of the image is normalised for both images. In terms of digital counts the peak intensity for the simulated PSF is 3688. For the experimental spot this value is 3215. The Strehl ratio for the system with adaptive flattening is therefore 0.87, above diffraction limited. The error on this value is undetermined.

Appendix C

Least Squares Fitting

A regular problem that occurs in adaptive optics is the fitting of one set of signals to some other space. Examples of this are fitting phase space signals to slope signals or finding the actuator control signals that minimise wavefront sensor signals. In the latter scheme a WFS records slope signals s for each actuator command c with the interaction matrix D defining the relationship between the two.

$$s = Dc \tag{C.1}$$

To find the control signals that produce a certain effect in phase space, the inverse of D is required, $c = D^{-1}s = Ms$. Closed loop AO requires the phase to be minimised at each iteration point. The mean square error of the system is

$$e = |s - Dc|^2 \tag{C.2}$$

Minimising this error with respect to c, $\frac{\partial e}{\partial c} = 0$. Using the Froebius norm this can be derived as[95],

$$\begin{aligned} \frac{\partial e}{\partial c} &= \frac{\partial}{\partial c}\text{trace}(ss^T - sc^T) - Dcs^T + Dcc^T D^T) \\ &= -2D^T s + 2D^T Dc = 0 \end{aligned}$$

This results in the least squares estimator

$$c = (d^T D)^{-1} D^T s = Ms \tag{C.3}$$

Inverting $D^T D$ usually results in a poorly conditioned matrix and Singular Value Decompositions is preferred.

$$D = UWV^T$$
$$M = VW^{-1}U^T$$

Bibliography

[1] H.W. Babcock. The possibility of compensating astronomical seeing. *Public. of the Astron. Soc. Pac.*, 65:229–236, 1953.

[2] N. Devaney, E. Dalimier, T. Farrell, D. Coburn, R. Mackey, D. Mackey, F. Laurent, E. Daly, and J.C. Dainty. Correction of ocular and atmospheric wavefronts: a comparison of the performance of various deformable mirrors. *Appl. Opt.*, 47:6550–6562, 2008.

[3] J.W. Hardy. *Adaptive Optics for Astronomical Telescopes*. Oxford University Press, 1998.

[4] G. Rousset, J.C. Fontanella, P. Kern, P. Gigan, and F. Rigaut. First diffraction-limited astronomical images with adaptive optics. *Astron. Astrophys.*, 230:L29–L32, 1990.

[5] R. Foy and A. Labeyrie. Feasibility of adaptive telescope with laser probe. *Astron. Astro.*, 152:L29–L31, 1985.

[6] David Le Mignant, Randall D. Campbell, Antonin H. Bouchez, Jason C. Y. Chin, Elizabeth Chock, Al Conrad, Marcos A. van Dam, Steve Doyle, Robert E. Goodrich, Erik M. Johansson, Robert E. Lafon, James E. Lyke, Christine Melcher, Ronald P. Mouser, Douglas M. Summers, Cynthia Wilburn D.V.M., and Peter L. Wizinowich. LGS AO operations at the w.m. keck observatory. *Proc. SPIE*, 6270, 2006.

[7] D. T. Gavel, S. S. Olivier, C. E. Max, H. W. Friedman, J. M. Brase, J. R. Morris, K. Avicola, J. T. Salmon, D. A. Rapp, H. D. Bissinger, and K. E. Waltjen. Laser Guide Star Adaptive Optics Systems for the Lick Observatory Telescopes. volume 25 of *Bulletin of the American Astronomical Society*, pages 888–+, 1993.

[8] R. V. Shack and B. C. Platt. Production and use of a lenticular Hartmann screen. *J. Opt. Soc. Am.*, 61(656), 1971.

[9] F. Roddier. Curvature sensing and compensation: a new concept in adaptive optics. *Appl. Opt.*, 27:1223–1225, 1988.

[10] F. Roddier, M. Northcott, and J. E. Graves. A simple low-order adaptive optics system for near-infrared applications. *Pub. Astron. Soc. Pac.*, 103:131–149, 1991.

[11] F. Rigaut, D. Salmon, R. Arsenault, J. Thomas, O. Lai, D. Rouan, J. P. V'eran, David Crampton, J. M. Fletcher, and J. Stilburn. Performance of the Canada-France-Hawaii telescope adaptive optics bonnette. *Public. of the Astron. Soc. Pac*, 110:15–2, 1998.

[12] J. W. Hardy, J. E. Lefebvre, and C. L. Koliopoulos. Real-time atmospheric compensation. *J. Opt. Soc. Am.*, 67:360–369, 1977.

[13] R. Ragazzoni. Pupil plane wavefront sensing with an oscillating prism. *J. Mod. Opt.*, 43:289–293, 1996.

[14] A. Burvall, E.Daly, S. R. Chamot, and J.C. Dainty. Linearity of the pyramid wavefront sensor. *Opt. Express*, 14:11925–11934, 2006.

[15] G. Rousset. *Adaptive optics in astronomy.* Cambridge University Press, 1999.

[16] H. H. Barrett, J.C. Dainty, and D. Lara. Maximum-likelihood methods in wavefront sensing: Stochastic models and likelihood functions. *J. Opt. Soc. Am. A.*, 24:391–414, 2007.

[17] A. N. Kolmogorov. The local structure of turbulence in incompressible viscous fluid for very large Reynolds numbers (translation). *Proceedings of the Royal Society of London A*, 434:9–13, 1991.

[18] V.I. Tatarski. *Wave Propagation in a Turbulent Medium.* McGraw-Hill, 1961.

[19] S. Voitsekhovich, V. V. Cuevas. Adaptive optics and the outer scale of turbulence. *J. Opt. Soc. Am. A*, 12:2253–2531, 1995.

[20] A. Ziad, M. Schock, G. A. Chanan, M. Troy, R. Dekany, B.F. Lane, J. Borgnino, and F. Martin. Comparison of measurements of the outer scale of turbulence by three different techniques. *Appl. Opt.*, 43:2316–2324, 2004.

[21] M. Le Louarn, N. Hubin, M. Sarazin, and A. Tokovinin. New challenges for adaptive optics: extremely large telescopes. *Mon. Not. R. Astron. Soc.*, 317:535–544, 2000.

[22] M. Azouit and J. Vernin. Optical turbulence profiling with balloons relevant to astronomy and atmospheric physics. *Public. of the Astron. Soc. Pac.*, 117:536–543, 2005.

[23] A. Rocca, F. Roddier, and J. Vernin. Detection of atmospheric turbulent layers by spatiotemporal and spatioangular correlation measurements of stellar-light scintillation. *J. Opt. Soc. Am.*, 64:1000–1004, 1974.

[24] D. Garnier. *Profiling Atmospheric Turbulence with Single Star SCIDAR).* PhD thesis, National University of Ireland Galway, 2007.

[25] R.W. Wilson. Slodar : measuring optical turbulence altitude with a shack-hartmann wavefront sensor. *Mon. Not. R. Astron. Soc.*, 337:103–108, 2002.

[26] F. Roddier. *Adaptive Optics in Astronomy.* Cambridge University Press, 1999.

[27] D. L. Fried. Statistics for a geometric representation of wavefront distortion,. *J. Opt. Soc. Am.*, 55:1427–1435, 1965.

[28] D. L. Fried. Optical resolution through a randomly inhomogeneous medium for very long and very short exposures. *J. Opt. Soc. Am.*, 56:1372–1379, 1966.

[29] Web. http://www.eso.org/sci/facilities/eelt/science/index.html.

[30] P. Kalas, J. R. Graham, E. Chiang, M. P. Fitzgerald, M. Clampin, E. S. Kite, K. Stapelfeldt, C. Marois, and J. Krist. Optical Images of an Exosolar Planet 25 Light-Years from Earth. *Science*, 322:1345–, 2008.

[31] D. L. Fried. Anisoplanatism in adaptive optics. *J. Opt. Soc. Am.*, 72:52–61, 1982.

[32] R.K. Tyson. *Principles of Adaptive Optics.* Academic Press, 1998.

[33] F. Rigaut and E. Gendron. Laser guide star in adaptive optics : the tilt determination problem'. *Astron. and Astro.*, 261:677, 1992.

[34] R. Flicker. *Methods of Multi-ConjugateAdaptive Optics for Astronomy.* PhD thesis, Lund Observatory.

[35] B. L. Ellerbroek and D. W. Tyler. Adaptive optics sky coverage calculations for the Gemini-North telescope. *Pub. Astron. Soc. Pac.*, 110:165–185, 1998.

[36] L. A. Thompson and C. S. Gardner. Experiments on laser guide stars at Mauna Kea Observatory for adaptive imaging in astronomy. *Nature*, 328:229–231, 1987.

[37] J. M. Beckers. Increasing the size of the isoplanatic patch with multiconjugate adaptive optics. In *ESO Conference on Very Large Telescopes and their Instrumentation, Vol. 2, p. 693 - 703*, volume 2, pages 693–703, 1988.

[38] M. L. Louarn and M. Tallon. Analysis of modes and behavior of a multiconjugate adaptive optics system. *J. Opt. Soc. Am. A*, pages 912–925, 2002.

[39] M. Tallon and R. Foy. Adaptive telescope with laser probe - isoplanatism and cone effect. *Astron, Astrophys.*, 235:549–557, 1990.

[40] B. Ellerbroek. First-order performance evaluation of adaptive-optics systems for atmospheric-turbulence compensation in extended-field-of-view astronomical applications. *J. Opt. Soc. Am. A*, 11:783–805, 1994.

[41] R. Ragazzoni, E. Marchetti, and G. Valente. Adaptive-optics corrections available for the whole sky. *Nature*, 403:54–56, 2000.

[42] F. Rigaut. Ground-conjugate wide field adaptive optics for the ELTs. In *Beyond Conventional Adaptive Optics*, Proc. ESO, 2001.

[43] A. Tokovinin. Seeing improvement with ground-layer adaptive optics. *Pub. Astron. Soc. Pac.*, 116:941–951, 2004.

[44] C. J. Baranec, M. Lloyd-Hart, M. Milton, T. Stalcup, M. Snyder, N. Putnam, and R. Angel. Ground layer wavefront reconstruction using dynamically refocused rayleigh laser beacons. In *Adaptive Optics: Analysis and Methods*, page AThA3, 2005.

[45] R. Angel. Ground-based imaging of extrasolar planets using adaptive optics. *Nature*, 368:203–207, 1994.

[46] J. Feinleib, S. G. Lipson, and P. F. Cone. Monolithic piezoelectric mirror for wavefront correction. *Appl. Phys. Lett.*, 25:311–313, 1974.

[47] B. R. Oppenheimer, D. Palmer, R. Dekany, A. Sivaramakrishnan, M. Ealey, and T. Price. Investigating a Xinetics Inc. deformable mirror. *Proc. SPIE*, 3126:569–579, 1997.

[48] R.H. Freeman and J.E. Pearson. Deformable mirrors for all seasons and reasons. *Appl. Opt.*, 21:580–589, 1982.

[49] E. Steinhaus and S.G. Lipson. Bimorph piezoelectic flexible mirrors. *J. Opt. Soc. Am.*, 69:478–481, 1979.

[50] R.P. Grosso and M. Yellin. The membrane mirror as an adaptive optical element. *J. Opt. Soc. Am.*, 67:399–406, 1977.

[51] J.A. Perreault, T.G. Bifano, B.M. Levine., and M.N. Horenstein. Adaptive optic correction using microelectromechanical deformable mirrors. *Opt. Eng.*, 41:561–566, 2002.

[52] G. Vdovin, M. Loktev, and A. Simonov. Low-cost deformable mirrors: technologies and goals. volume 5894 of *SPIE*, pages 0B–1 – OB10, 2005.

[53] M. A. Ealey. Low-voltage SELECT deformable mirrors. *Proc. SPIE*, 1920, 1993.

[54] E. Dalimier and C. Dainty. Comparative analysis of deformable mirrors for ocular adaptive optics. *Optc. Expr.*, 13:4275–4285, 2005.

[55] W.M. Press, S.A. Teukolsky, W.T. Vetterling, and B.P. Flannery. *Numerical Recipes in C*. Cambridge University Press, 1992.

[56] G. Vdovin and P.M. Sarro. Flexible mirror micromachined in silicon. *Appl. Opt.*, 34:2968–2972, 1995.

[57] T.G. Bifano, R.K. Mali, J.K. Dorton, J. Perreault, N. Vandelli, M.N. Horenstein, and D.A. Castanon. Continuous-membrane surface-micromachined silicon deformable mirror. *Opt. Eng.*, 36:1354–1360, 1997.

[58] J. A. Perreault, T. G. Bifano, B. M. Levine, and M. N. Horenstein. Adaptive optic correction using micro-electro-mechanical deformable mirrors. *Optical Engineering*, 41:561–566, 2002.

[59] J.W. Evans, B. Macintosh, L. Poyneer, K. Morzinski, S. Severson, D. Dillon, D. Gavel, and L. Reza. Demonsrating sub-nm closed loop MEMS flattening. *Opt. Expr.*, 14:5558–5570, 2006.

[60] M. Bruce, G. James, B. Oppenheimer, L. Poyneer, A. Sivaramakrishnan, and J.-P. Veran. MEMS-based extreme adaptive optics for planet detection. *Proc. SPIE*, 6467:48–57, 2007.

[61] R. Conan, C. Bradley, P. Hampton, O. Keskin, A. Hilton, and C. Blain. Distributed modal command for a two-deformable-mirror adaptive optics system. *Appl. Opt.*, 46:4329–4340, 2007.

[62] R.J. Noll. Zernike polynomials and atmoshperic turbulence. *J. Opt. Soc. Am.*, 66: 207–211, 1976.

[63] D. P. Greenwood. Mutual coherence function of a wave front corrected by zonal adaptive optics. *J. Opt. Soc. Am*, 69:549, 1979.

[64] R.K. Tyson. *Adaptive Optics Engineering Handbook*. Marcel Dekker.

[65] B. P. Wallace, P. J. Hampton, C. H. Bradley, and R. Conan. Evaluation of a MEMS deformable mirror for an adaptive optics test bench. *Opt. Expr.*, 14:10132–10138, 2006.

[66] R. Conan. Mean-square residual error of a wavefront after propagation through atmospheric turbulence and after correction with Zernike polynomials. *J. Opt. Soc. Am. A*, 25:526–536, 2008.

[67] G. Vdovin, O. Soloviev, A. Samokhin, and M. Loktev. Correction of low order aberrations using continuos deformable mirrors. *Opt. Expr.*, 16:2859–2866, 2008.

[68] C. M. Harding, R.A. Johnston, and R.G. Lane. Fast simulation of Komolgorov phase screen. *Appl. Opt.*, 38:2161–2170, 1999.

[69] T. Farrell, E. Daly, E. Dalimier, and C. Dainty. Task-based assessment of deformable mirrors. *Proc SPIE*, 6467, 2007.

[70] Devaney N, D. Coburn, C. Coleman, J. C. Dainty, E. Dalimier, T. Farrell, D. Lara, D. Mackey, and R. Mackey. Characterisation of MEMS mirrors for use in atmospheric and ocular wavefront correction. *Proc. SPIE*, 6888:688802, 2008.

[71] M. Roggemann and D. Lee. Two-deformable mirror concept for correcting scintillation effects in laser beam propagation in turbulent atmosphere. *Appl. Opt.*, 37: 4577–4585, 1998.

[72] R. Flicker. Sequence of phase correction in multiconjugate adaptive optics. *Opt. Lett.*, 26:1743–1745, 2001.

[73] H. Baumhacker, G. Pretzler, K.J. Witte, M. Hegelich, M. Kaluza, S. Karsch, A. Kudryashov, V. Samarkin, and A. Roukossouev. Correction of strong phase and amplitude modulations by two deformable mirrors in a multistaged ti:sapphire laser. *Opt. Lett.*, 27:1570–1572, 2002.

[74] R. Gilmozzi and J. Spyromilio. The european extremely large telescope (E-ELT). *The Messenger*, 127:11–19, 2007.

[75] R. G. Dekany, M. C. Britton, D. T. Gavel, B. L. Ellerbroek, G. Herriot, C. E. Max, and J.-P. Veran. Adaptive optics requirements definition for TMT. volume 5490 of *SPIE*, pages 879–890, 2004.

[76] B. Ellerbroek and F. Rigaut. Adaptive optics requirements, concepts, and performance predictions for extremely large telescopes. Conference talk. www.gsmt.noao.edu/presentations/AO_OptoSW.ppt.

[77] S. Hu, B. Xu, X. Zhang, J. Hou, J. Wu, and W. Jiang. Double-deformable-mirror adaptive optics system for phase compensation. *Appl. Opt.*, 45:2638–2642, 2006.

[78] S.M. Jones, S. Olivier, D. Chen, S. Joeres, S. Sadda, R.J. Zawadzki, J.S. Werner, and D.T. Miller. Adaptive optics ophthalmologic systems using dual deformable mirrors. *SPIE*, 6467:64670H1 – 64670H14, 2007.

[79] D.C. Chen, S.M. Jones, D.A. Silva, and S.S. Olivier. High-resolution adaptive optics scanning laser ophthalmoscope with dual deformable mirrors. *J. Opt. Soc. Am. A*, 24:1305–1312, 2007.

[80] W. Zou, X. Qi, and S. A. Burns. Wavefront-aberration sorting and correction for a dual-deformable-mirror adaptive-optics system. *Opt. Lett.*, 33:2602–2604, 2008.

[81] A. Goncharov, J.C. Dainty, S. Esposito, and A. Puglisi. Laboratory MCAO test-bed for developing wavefront sensing concepts. *Opt. Express*, 13:5580–5590, 2005.

[82] J. Schmidt, J. Knobbe, A. Gehner, and H. Lakner. CMOS integrable micro mirrors with highly improved drift-stability. *SPIE*, 6467, 2007.

[83] Y. Liu, H.-m. Bao, J. Li, J. Ruan, and Z. Hao. Measuring the system gain of the TDI CCD remote sensing camera. *Proc SPIE*, 5633:520–526, 2005.

[84] Axiom Research Inc. Axiom tech note. Web. http://www.personal.psu.edu/sdb210/stash/.

[85] A. Goncharov, J.C. Dainty, and S. Esposito. Compact multireference wavefront sensor design. *Opt. Lett.*, 30:2721–2723, 2005.

[86] R.H. Hudgin. Wave-front reconstruction for compensated imaging. *J. Opt. Soc. Am.*, 67:375–378, 1977.

[87] O. Keskin, L. Jolissaint, and C. Bradley. Hot-air optical turbulence generator for the testing of adaptive optics systems: principles and characterization. *Appl. Opt.*, 45:4888–4897, 2006.

[88] D.J. Butler, S. Hippler, S. Egner, W. Xu, and J. Bahr. Broadband, static wavefront generation: Na-ag ion-exchange phase screens and telescope emulation. *Appl. Opt.*, 43:2813–2823, 2004.

[89] S. Hippler, F. Hormuth, D.J. Butler, W. Brandner, and T. Henning. Atmospher-like turbulence generation with surfac-etched phase-screens. *Opt. Express*, 14:10139–10149, 2006.

[90] E. Marchetti, N. N. Hubin, E. Fedrigo, J. Brynnel, B. Delabre, R. Donaldson, F. Franza, Rodolphe Conan, Miska Le Louarn, Cyril Cavadore, Andrea Balestra, Dietrich Baade, Jean-Luis Lizon, Roberto Gilmozzi, Guy J. Monnet, Roberto Ragazzoni, Carmelo Arcidiacono, Andrea Baruffolo, Emiliano Diolaiti, Jacopo Farinato, Elise Vernet-Viard, David J. Butler, Stefan Hippler, and Antonio Amorin. MAD the ESO multi-conjugate adaptive optics demonstrator. *Proc SPIE*, 4839:317–328, 2003.

[91] P. Hampton, C. Bradley, P. Agathoklis, and R. Conan. Control system performance of a woofer-tweeter adaptive optics system. In *The Advanced Maui Optical and Space Surveillance Technologies Conference*, 2006.

[92] C. Paterson, I. Munro, and J.C. Dainty. A low cost adaptive optics system using a membrane mirror. *Opt. Expr.*, 6:175–185, 2000.

[93] J.-F. Sauvage, T. Fusco, G. Rousset, and C. Petit. Calibration and precompensation of noncommon path aberrations for extreme adaptive optics. *J. Opt. Soc. Am. A*, 24:2334–2346, 2007.

[94] Peter J. Hampton, Rodolphe Conan, Colin Bradley, and Pan Agathoklis. Control of a woofer tweeter system of deformable mirrors. *Proc. SPIE*, 6274:62741Z, 2006.

[95] W.J. Vetter. Derivative operations on matrices. *IEEE Trans. Auto. Control*, 15: 241–244, 1970.